GEORG-AUGUST-UNIVERSITÄT
GÖTTINGEN

Fakultät für
Physik

Master's Thesis

Search for Top Flavour Violating Resonances in $t\bar{t}$ + jet Events with the ATLAS Experiment

Suche nach Top-Jet Resonanzen in $t\bar{t}$ + jet Ereignissen mit dem ATLAS Detektor

prepared by

Chris Malena Delitzsch

from Hamburg

at the II. Institute of Physics

Thesis period:	April 1, 2012 until September 30, 2012
Supervisor:	Dr. Kevin Kröninger
First Referee:	Prof. Dr. Arnulf Quadt
Second Referee:	Prof. Dr. Ariane Frey
Thesis number:	II.Physik-UniGö-MSc-2012/07

Contents

1. Introduction

The question about the fundamental building blocks of matter and their interactions has concerned mankind for many centuries. Our current knowledge about the constituents of matter is described by the *Standard Model of particle physics* (SM) which has been formulated in the 1970s. According to the SM, matter is made up of elementary particles – *quarks* and *leptons* – which interact via three fundamental forces mediated by *gauge bosons*. The predictions of the SM have been tested with high precision within the last decades and were in agreement with the observations. Although being such a successful theory, the SM cannot explain for example the origin of dark matter and the asymmetry between matter and antimatter. In order to solve these unanswered questions, high-energy particle accelerators are built to enable measurements at new energy scales.
The Large Hadron Collider (LHC) at CERN is the world's largest particle accelerator with a centre-of-mass energy of $\sqrt{s} = 8$ TeV. Protons are accelerated to close to the speed of light and are brought to collision in four different interaction points. In the years 2011 and 2012, the LHC has delivered data corresponding to an integrated luminosity of approximately $\mathcal{L} = 19$ fb^{-1} at $\sqrt{s} = 7$ and 8 TeV. With this amount of data, the ATLAS and CMS collaboration were able to present the first observation of a new boson in the context of the Standard Model Higgs boson search. The Higgs boson is the last missing particle in the SM, predicted by the so-called *Higgs mechanism* which gives mass to the gauge bosons of the weak interaction.

The heaviest particle of the SM is the top quark with a mass of $m_\mathrm{t} = 173.2 \pm 0.9$ GeV which is close to the scale of electroweak symmetry breaking. Therefore the top quark plays an important role in searches for physics beyond the Standard Model. Due to its large mass, the top quark decays before it can hadronise and does not form bound states. Thus it is the only quark which can be studied as a *bare* quark. At the Tevatron, a 3.4 σ deviation of the top forward-backward asymmetry A_FB above the next-to-leading order QCD prediction has been measured by the CDF collaboration. The DØ collaboration has also measured A_FB with a discrepancy of three standard deviations. Measurements of the corresponding asymmetry A_FB by the ATLAS and CMS collaboration with the 2011 data showed no deviations from the SM predictions. A wide class of models like axigluons, extra-dimensions, new heavy gauge bosons or diquarks have been presented to explain the anomalous forward backward asymmetry.

In this thesis, a search for a new top-flavour violating particle M is presented. The particle M could either be a new heavy gauge boson or a diquark as part of a colour triplet state which is produced in association with a top quark. The analysis is based on data corresponding to an integrated luminosity of $\mathcal{L} = 4.71$ fb^{-1} recorded with the ATLAS detector in 2011.

The thesis is organised as follows: Chapter 2 gives a summary of the Standard Model followed by an introduction to top quark physics including the production and decay mechanism. Afterwards the measurement of the top forward-backward asymmetry measured at the Tevatron is discussed and a new model including top-flavour violating resonances is introduced to explain the measured asymmetry. A short introduction in the Large Hadron Collider and the ATLAS detector is given in chapter 3 followed by the object definitions in chapter 4. Chapter 5 describes the signal and background Monte Carlo (MC) samples, the data driven background estimates as well as the data set used for the analysis. The event selection which is optimized for the search of a new top-flavour violating resonance in $t\bar{t}$ + jet events is introduced in chapter 6. The reconstruction of $t\bar{t}$ events is done with a Kinematic Likelihood Fitter (KLFitter) which is described in chapter 7 as well as studies for the performance of the KLFitter. Chapter 8 summarises the analysis strategy and introduces the two-dimensional binning method used to enhance the signal over background ratio, followed by the sources of systematic uncertainties which are presented in chapter 9. The $\mathrm{CL_s}$ method, motivated by frequentist statistics, is used to set limits on the production cross section and is introduced in chapter 10. The results are then presented in chapter 11.

2. The Top Quark in Context of the Standard Model

In this chapter a short introduction to the Standard Model of particle physics and an overview of the top quark is given. Afterwards the measurement of the top forward-backward asymmetry is discussed and new models which could explain the anomalous asymmetry are presented.

2.1. The Standard Model of Particle Physics

The *Standard Model of particle physics* (SM) [1, 2] is the most successful theoretical model to describe the elementary particles and their fundamental interactions. The predictions of the SM have been tested with very high precision in many experiments and no significant deviations have been observed so far [3]. The SM distinguishes between fermions with half-integer spin and vector bosons with integer spin. The fundamental interactions between fermions are mediated by these bosons. The SM incorporates three of the four fundamental forces, the electromagnetic, the weak and the strong force which are described by relativistic quantum field theories. Gravity is not included in the SM as it can be neglected at energy scales which are accessible with the current collider experiments.

2.1.1. Quarks and Leptons

The SM contains twelve fermions which are grouped into leptons and quarks. The fermions are arranged into three generations with increasing masses. Each generation consists of two doublets of left-handed particles and right-handed singlets.

$$
\begin{array}{cccc}
\text{Generation:} & \text{I} & \text{II} & \text{III} \\
 & \begin{pmatrix} \nu_e \\ e \end{pmatrix} & \begin{pmatrix} \nu_\mu \\ \mu \end{pmatrix} & \begin{pmatrix} \nu_\tau \\ \tau \end{pmatrix} \\
 & \begin{pmatrix} u \\ d \end{pmatrix} & \begin{pmatrix} c \\ s \end{pmatrix} & \begin{pmatrix} t \\ b \end{pmatrix}
\end{array}
$$

A charged lepton (e, μ, τ) with electric charge $Q = -e$ [1] forms together with its corresponding

---

[1] e is the charge of a proton and $|e|$ the charge of an electron

electrically neutral neutrino (ν_e, ν_μ, ν_τ) the lepton doublet. The quark doublet comprises an up-type quark (u, c, t) with electric charge $Q = \frac{2}{3}e$ and a down-type quark (d, s, b) with $Q = -\frac{1}{3}e$. The masses of the fermions are listed in Tab.2.1.

Lepton	Mass [MeV]	Quark	Mass [MeV]
e	0.511	u	1.7-3.1
ν_e	$< 2 \cdot 10^{-6}$	d	4.1-5.7
μ	105.658	c	$(1.29^{+0.05}_{-0.11}) \cdot 10^3$
ν_μ	< 0.19 (90% CL)	s	100^{+30}_{-20}
τ	1776.82 ± 0.16	t	$(173.2 \pm 0.9) \cdot 10^3$
ν_τ	< 18.2 (95% CL)	b	$4.19^{+0.18}_{-0.06}$

Table 2.1.: Masses of the fermions [4]. The electron and muon mass are measured with a very high precision. The uncertainties on their masses are therefore neglected.

The first generation contains the fermions, which are the building blocks of the visible matter. The up and down quark are the constituents of the proton and form, together with the electrons, the atoms. For each fermion a corresponding antifermion exists with the same mass and spin but opposite charge and weak isospin.

The doublets are classified by the characterizing quantum numbers of the weak interaction, the third component of the weak isospin I_3 and the weak hypercharge Y which are related to the electric charge Q:

$$Q = I_3 + \frac{Y}{2} \; .$$

Up-type quarks as well as charged leptons have a weak isospin of $+\frac{1}{2}$ while down-type quarks and neutrinos have a weak isospin of -$\frac{1}{2}$. Right-handed particles form singlets with $I_3 = 0$ and do not interact weakly.

Furthermore, quarks carry an additional quantum number called *colour* charge which can be either red, blue or green.

2.1.2. Interactions

The Standard Model describes three fundamental forces: the strong, the electromagnetic and the weak force. These interactions can be expressed by local gauge symmetries, i.e. the Lagrangian is locally invariant under the action of a special unitary gauge group $SU(N)$. Each interaction is described by $N^2 - 1$ gauge bosons which corresponds to the number of generators of the gauge group and its dimension [5].

The symmetry group of the Standard Model is

$$\mathrm{SU}(3)_C \otimes \mathrm{SU}(2)_L \otimes \mathrm{U}(1)_Y$$

which is the combination of the strong and electroweak interaction which will be explained in the following.

Quantum Chromodynamics

The strong force is described by the $\mathrm{SU}(3)_C$ gauge group, also known as Quantum Chromodynamics (QCD) which is generated by the eight three-dimensional Gell-Mann matrices, λ_i. The mediators of this group are eight colour-charged massless gluons. Gluons do not carry electromagnetic charge but colour and anti-colour and couple therefore only to quarks or to themselves.

In contrast to leptons, quarks do not exist as free particles but form mesons ($q\bar{q}$) or baryons (qqq or $\bar{q}\bar{q}\bar{q}$), also called *hadrons* because of the *confinement*. This phenomenon can be described by the energy dependence of the strong coupling constant. When two quarks are separated, the potential energy between these quarks increases until it becomes energetically favourable to create a new quark-antiquark pair. These two quarks form, together with the two initial quarks, a bound state. The strong coupling constant, g_s, is related to α_s, and its energy dependence is

$$\alpha_s(Q^2) = \frac{12\pi}{(33 - 2n_f)\log(\frac{Q^2}{\Lambda^2})} \; .$$

Λ is a commonly chosen scale and is determined from measurements to be $\Lambda \approx 200$ MeV. The parameter n_f is the number of quark flavours at a certain energy scale Q. For energy scales larger than the heaviest quark mass, i.e. the top quark mass ($Q > m_t$), the number of quark flavours in the SM is six. For large energy scales ($Q^2 > \Lambda^2$), or short distances, the strength of the strong coupling decreases. Therefore, quarks can be treated as free particles at short distances which allows the usage of perturbation theory in QCD. The antiscreening of the colour charge is called *asymptotic freedom*. While the strong coupling constant decreases at larger energy scales, the coupling constant of the electromagnetic interaction increases. This opposite behaviour is due to the self-coupling of the gluons in comparison to the photons which cannot couple to themselves.

Electroweak Interactions

In 1967, Glashow, Weinberg and Salam proposed to unify the description of the electromagnetic and weak interaction to the *electroweak* interaction by the group $\mathrm{SU}(2)_L \otimes \mathrm{U}(1)_Y$. The index L implies that the weak interaction couples exclusively to left-handed fermions. The group $\mathrm{SU}(2)_L$ is generated by the three Pauli matrices σ_i, with $i = 1, 2, 3$ and consists of an isotriplet of vector gauge fields $W_\mu^{1,2,3}$. The hypercharge Y is the generator of the $\mathrm{U}(1)$ group which contains only an isosinglet gauge field B_μ. The gauge bosons of the electroweak force, i.e. the massless photon and the massive bosons $W^{\pm}, Z^0$ are linear combinations of the gauge fields $W_\mu^{1,2,3}$ and B_μ. The mass eigenstates of the neutral gauge bosons can be written as

$$\begin{aligned} A_\mu &= W_\mu^3 \sin\theta_W + B_\mu \cos\theta_W \quad \text{(photon)} \\ Z_\mu &= W_\mu^3 \cos\theta_W - B_\mu \sin\theta_W \quad (Z^0)\ . \end{aligned}$$

θ_W is the *Weinberg-angle* which describes the mixing between $\mathrm{SU}(2)_L$ and $\mathrm{U}(1)_Y$ and is connected to their coupling constants g and g':

$$\sin\theta_W = \frac{g'}{\sqrt{g^2 + g'^2}}\ .$$

Its measured value is:

$$\sin^2\theta_W = 0.21316 \pm 0.00016\ [4]\ .$$

The charged gauge bosons are defined as:

$$W_\mu^{\pm} = \frac{1}{\sqrt{2}}(W_\mu^1 \mp i W_\mu^2)\ .$$

The photon is the mediator of the electromagnetic interaction and couples only to charged particles. Since it is massless, the electromagnetic interaction has an infinite range.

The massive gauge bosons $W^{\pm}$ and Z^0 are the mediators of the weak interaction. While the Z^0 can couple to all fermions, the $W^{\pm}$ bosons couple only to left-handed particles. Due to the large mass of the gauge bosons, the weak force has only a limited range and dominates only at high energies. The relative strength of the interactions are listed in Tab.2.2. Although the coupling of the weak interaction is larger than the coupling of the U(1) gauge, it is suppressed due to the large mass of the weak gauge bosons.

Interaction	Mediator	Mass	Relative strength
Strong	Gluon	0	1
Electromagnetic	Photon	$< 1 \cdot 10^{-18}$ eV	10^{-2}
Weak	$W^{\pm}$	80.399 ± 0.023 GeV	10^{-13}
	Z^0	91.1876 ± 0.0021 GeV	

Table 2.2.: Fundamental forces of the SM with their associated mediators and interactions strengths. In addition, the masses of the gauge bosons are listed.

In the weak interaction, the eigenstates of the quarks q' are linear combinations of the mass eigenstates q of the physical quarks, represented by the unitary 3×3 *Cabibbo-Kobayashi-Maskawa* (CKM) matrix:

$$\begin{pmatrix} d' \\ s' \\ b' \end{pmatrix} = \begin{pmatrix} V_{ud} & V_{us} & V_{ub} \\ V_{cd} & V_{cs} & V_{cb} \\ V_{td} & V_{ts} & V_{tb} \end{pmatrix} \cdot \begin{pmatrix} d \\ s \\ b \end{pmatrix} \ .$$

Since the CKM matrix differs from the unit matrix, flavour changing charged currents, i.e. transitions between the three quark generations are possible in the weak interaction. No flavour changing neutral currents have been observed so far. For leptons, the *Pontecorvo-Maki-Nakagawa-Sakata* (PMNS) matrix describes the mixing between the neutrino flavour eigenstates ν_α ($\alpha = e, \mu, \tau$) and the mass eigenstates i.

2.1.3. Electroweak Symmetry Breaking

Since the massive gauge bosons $W^\pm$ and Z^0 would break the local gauge invariance of the SM Lagrangian, the so-called *Higgs mechanism* [6, 7] was introduced. The Higgs mechanism is based on spontaneous symmetry breaking which results in an additional term in the SM Lagrangian:

$$\mathcal{L}_{\text{Higgs}} = (D^\mu \Phi)^\dagger (D_\mu \Phi) - V(\Phi) \ ,$$

where Φ is a complex scalar field in the spinor representation of $\text{SU}(2)_L$:

$$\Phi = \begin{pmatrix} \Phi^+ \\ \Phi^0 \end{pmatrix} \ .$$

The covariant derivative D_μ for left-handed particles is defined as

$$D_\mu = \partial_\mu + ig\frac{\sigma_i}{2} \cdot W^i_\mu + i\frac{g'}{2} Y B_\mu \ ,$$

whereas the second term vanishes for right-handed particles since they do not carry isospin. The Higgs potential has to be of the form

$$V(\Phi) = \mu^2 \Phi^\dagger \Phi + \lambda (\Phi^\dagger \Phi)^2 \quad \text{with } \lambda > 0$$

in order to be renormalisable and to be invariant under $\text{SU}(2)_L \otimes \text{U}(1)_Y$.

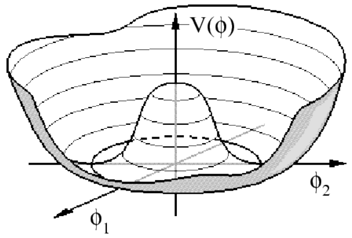

Figure 2.1.: The Higgs potential for the case $\mu^2 < 0$.

If $\mu^2 < 0$, the potential has a non-zero vacuum expectation value v as shown in Fig. 2.1. For $\Phi_0 = \pm\sqrt{-\frac{\mu^2}{2\lambda}} = \frac{v}{\sqrt{2}}$, the potential has its global minimum, with $v \approx 246$ GeV. The non-zero vacuum expectation value causes the symmetry breaking of $\mathrm{SU}(2)_L \otimes \mathrm{U}(1)_Y$. Due to the symmetry of the potential, the states satisfying $\Phi^\dagger\Phi = \frac{v}{2}$ are infinitely degenerated. Usually the ground state is arbitrarily chosen to be:

$$\Phi_0 = \frac{1}{\sqrt{2}}\begin{pmatrix} 0 \\ v \end{pmatrix}$$

such that the scalar Higgs doublet Φ can be obtained by perturbative expansion:

$$\Phi_0 = \frac{1}{\sqrt{2}}\begin{pmatrix} 0 \\ v + H(x) \end{pmatrix}$$

with the real scalar field H. Expanding the Lagrangian around the ground state yields:

$$\mathcal{L} = \underbrace{\frac{1}{2}\partial_\mu H \partial^\mu H}_{\text{kinetic term}} + \underbrace{\frac{1}{4}g^2 v^2 W_\mu^+ W^{-\mu} + \frac{1}{8}(g^2 + g'^2)v^2 Z_\mu Z^\mu - \lambda v^2 H^2}_{\text{mass terms}} - \underbrace{\lambda v H^3 - \frac{1}{4}H^4}_{\text{self-coupling of H field}} \tag{2.1}$$

The first term in equation 2.1 is the kinetic term for the Higgs field. A mass term of a field F in the Lagrangian is of the form $\frac{1}{2}m^2F^2$. Therefore the masses of the gauge bosons and the Higgs boson can be directly extracted from the Lagrangian:

$$\begin{aligned} m_{W^\pm} &= \frac{1}{2}gv \ , \\ m_Z &= \frac{1}{2}v\sqrt{g^2 + g'^2} \ , \\ m_H &= \sqrt{2\lambda}v \ . \end{aligned}$$

In the Higgs mechanism, the photon remains massless since no term proportional to $A_\mu A^\mu$ exists in the Lagrangian. The mass of the Higgs boson cannot be determined due to the unknown parameter λ. So far, the mass of the Higgs boson could only be predicted from precision measurements of the top quark and W boson mass. On the 4th of July, the ATLAS and CMS collaboration presented the latest results for the Higgs boson search with the full 2011 and part of the 2012 data in a dedicated seminar at CERN. Both collaborations reported the discovery of a new boson with a mass of approximately 126 GeV.

Furthermore, the Lagrangian describes the self-coupling of the Higgs field. Terms of the order $\mathcal{O}(\mathrm{HW^+W^-}, \mathrm{HZZ}, \mathrm{HHW^+W^-}, \mathrm{HHZZ})$ which represent the coupling of the Higgs field to the massive gauge bosons have been neglected in equation 2.1.

The Higgs mechanism was introduced in order to explain the masses of the gauge bosons while the masses of the fermions cannot be extracted directly from the Lagrangian 2.1. The fermion masses are implemented in the Standard Model by a Yukawa coupling of the Higgs field to the fermions. The strength of the coupling g_f is proportional to the mass of the fermion m_f:

$$m_f = \frac{g_f \cdot v}{\sqrt{2}} \ .$$

Observation of a New Particle in the Search for the Higgs Boson

The ATLAS and CMS collaboration performed a search for the Standard Model Higgs boson in proton-proton collisions at the Large Hadron Collider using the data taken in 2011 and 2012 at centre-of-mass energies of $\sqrt{s}$ = 7 TeV and 8 TeV, respectively. The search of the ATLAS collaboration is based on the full 2011 data sample, corresponding to an integrated luminosity of $\mathcal{L} = 4.8$ fb^{-1} and 5.8 fb^{-1} of data taken in 2012. The decay channels analysed in the 2011 data, $H \to \gamma\gamma$, ZZ^*, WW^*, $b\bar{b}$, $\tau^+\tau^-$ were combined with the high-mass resolution searches $H \to \gamma\gamma$, $H \to ZZ^* \to 4\ell$ and $H \to WW^* \to e\nu\mu\nu$ in the 8 TeV data. An excess above the expected background is observed with a local significance of 5.9 σ at a mass of 126 ± 0.4(stat) ± 0.4(syst) [8]. This corresponds to a probability of $1.7 \cdot 10^{-9}$ that the observation is the result of a statistical background fluctuation, which in turn implies the Higgs boson production and decay. The CMS collaboration analysed $\mathcal{L} = 5.1$ fb^{-1} and 5.3 fb^{-1} of 7 TeV and 8 TeV data, respectively using five different decay modes: $H \to \gamma\gamma$, ZZ^*, WW^*, $b\bar{b}$, $\tau^+\tau^-$. With a local significance of 5.0 σ, a new particle with a mass of 125.3 ± 0.4(stat) $\pm$ 0.5(syst) has been discovered [9]. Taking the look-elsewhere effect into account, the global significance in the mass range 115-130 GeV corresponds to 4.6 σ. The new particle is expected to be a boson with a spin different from one due to the decay into two photons. Fig.2.2 shows the observed local p-value as a function of the Higgs mass for the ATLAS (a) and CMS (b) collaborations. The dashed line corresponds to the expected local p-value under the hypothesis of a SM Higgs boson.

2.1.4. Open Questions in the SM

Although the SM is a very successful theory, it is not complete because several aspects cannot be explained by the SM.

Only about 4.6% of the energy of the Universe is the baryonic matter comprising the particles of the SM. The remaining 95% of the Universe energy density is *dark matter* and *energy* which are not described by the SM. A possible dark matter candidate in supersymmetric models could be the lightest supersymmetric particle (LSP).

Furthermore, the source of the matter-antimatter asymmetry is an unanswered question in the SM. During the Big Bang, the same amount of matter and antimatter were produced. Without an asymmetry, particles and antiparticles would have annihilated. The CP violation in the weak interaction is too small to explain the observed asymmetry.

After the electroweak unification, it is assumed that the strong force and electroweak force are described by a *Grand Unified Theory (GUT)*. This would result in the convergence of the

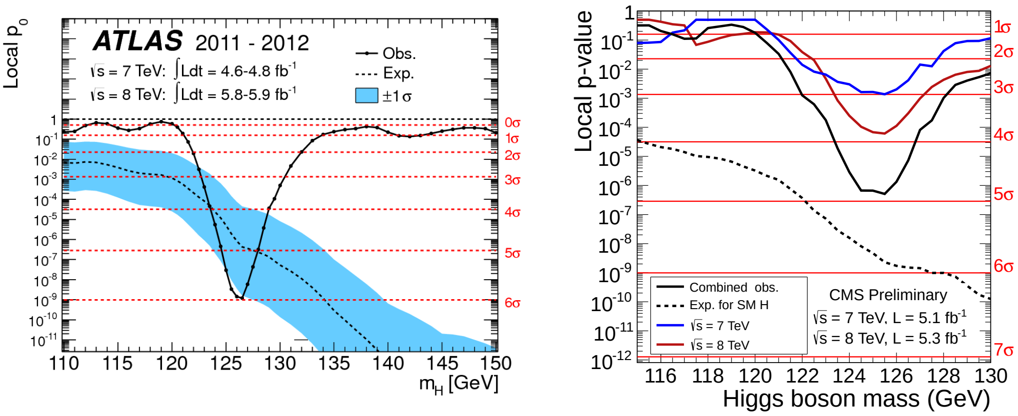

(a) ATLAS collaboration (b) CMS collaboration

Figure 2.2.: Observed local p-value (solid black line) as a function of the Higgs mass m_{H} measured by the ATLAS (a) and CMS (b) collaboration for the 2011 and 2012 data. The expected local p-value under the assumption of a SM Higgs boson is shown as the dashed line.

coupling constants of the three forces at the grand unification scale of approx. 10^{16} GeV. In the SM the coupling constants do not unify.

2.2. Top Quark Physics

The top quark was discovered in 1995 at the Tevatron collider at Fermilab [10, 11] although it has been predicted already in 1977 as the weak isospin partner of the b-quark [12]. The top quark is the heaviest known elementary particle with a mass of $m_t = 173.2 \pm 0.9$ GeV [13]. Its mass is the most precisely measured quark mass with a relative precision of 0.54%. Due to its large mass, the top quark plays an important role for searches of physics beyond the SM.

2.2.1. Hadron Collider Physics

So far, top quarks have only been produced at hadron colliders. In order to describe the proton-proton interactions at the LHC, the short distance structure of the proton has to be well understood. Experiments like the ep-accelerator HERA at DESY [14] investigated the proton structure through deep inelastic scattering (DIS). A Feynman diagram for the deep inelastic scattering in an ep-collision is shown in Fig. 2.3. The energy transfer by the virtual photon is denoted as q. At low energies, the proton consists of three valence quarks: two up quarks and one down quark. At large energies and therefore small distances, the proton comprises in addition sea quarks and gluons. Hence, the structure of the proton is determined by the energy scale μ_F^2 $(-q^2 = \mu_F^2)$, the so-called factorization scale at which the proton is probed.

The constituents of the proton carry only a fraction x, the so-called Bjorken x of the proton mo-

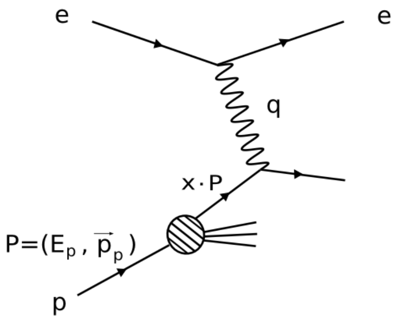

Figure 2.3.: Feynman diagram for the deep inelastic scattering in a *ep* collision.

mentum. The probability for a parton i with a certain momentum fraction x_i to be in the proton when probed at a scale μ_F^2 is described by the parton distribution function (PDF) $f_i(x_i, \mu_F^2)$. Since the momentum fraction cannot be calculated a priori by pertubative QCD, the PDFs are measured in DIS experiments and parametrized as a function of x_i and and at a starting scale μ_0^2 and taken to higher mu^2 values via the Altarelli-Parisi evolution equations [15]. The PDFs for two different scales using the CT10 parametrization are shown in Fig. 2.4.

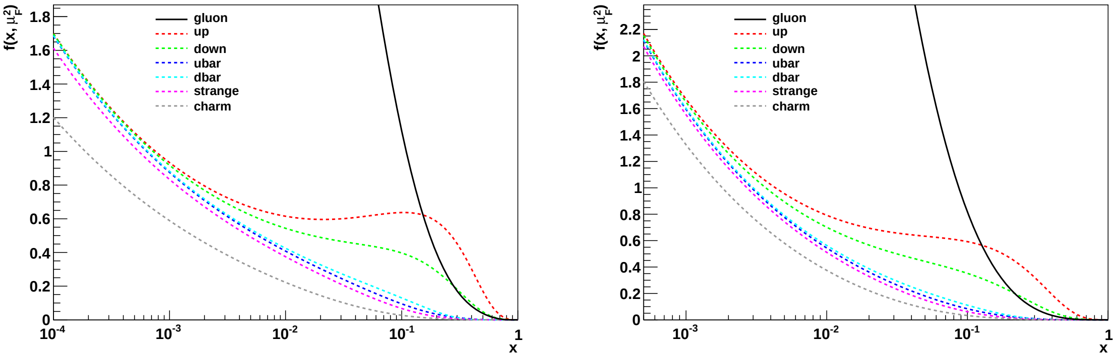

(a) $\mu_F^2 = 100$ GeV (b) $\mu_F^2 = m_t^2$

Figure 2.4.: CT10 parton distribution functions for two different μ_F scales [16].

According to the factorization theorem, the leading order cross section σ for the process $pp \to AB$ can be separated into the short distance partonic hard scattering process $\hat{\sigma}_{ij\to AB}$ convoluted with the parton distribution functions:

$$\sigma_{pp\to X} = \sum_{i,j} \int \int \mathrm{d}x_1 \mathrm{d}x_2 f_i(x_1, \mu^2) f_j(x_2, \mu^2) \hat{\sigma}_{ij\to AB}(x_1, x_2, \alpha_s, \hat{s}) \ .$$

The squared partonic centre-of-mass energy $\hat{s}$ is defined as $\hat{s} = x_i x_j s$ and the indices i and j sum over all quarks, antiquarks and gluons.

2.2.2. Top Quark Production

Top Pair Production

Top quark pairs are produced via the strong interaction in two different processes: at leading order these are quark-antiquark ($q\bar{q}$) annihilation and gluon-gluon (gg) fusion. The corresponding Feynman diagrams are shown in Fig. 2.5. The next-to-next-to leading order $t\bar{t}$ production cross section at the LHC is

$$\sigma_{t\bar{t}} = 166.8^{+16.5}_{-17.8}\,\text{pb}$$

for a centre-of-mass energy of $\sqrt{s} = 7$ TeV and a top quark mass of $m_t = 172.5$ GeV [17] and includes also the process $qg \rightarrow t\bar{t}$.

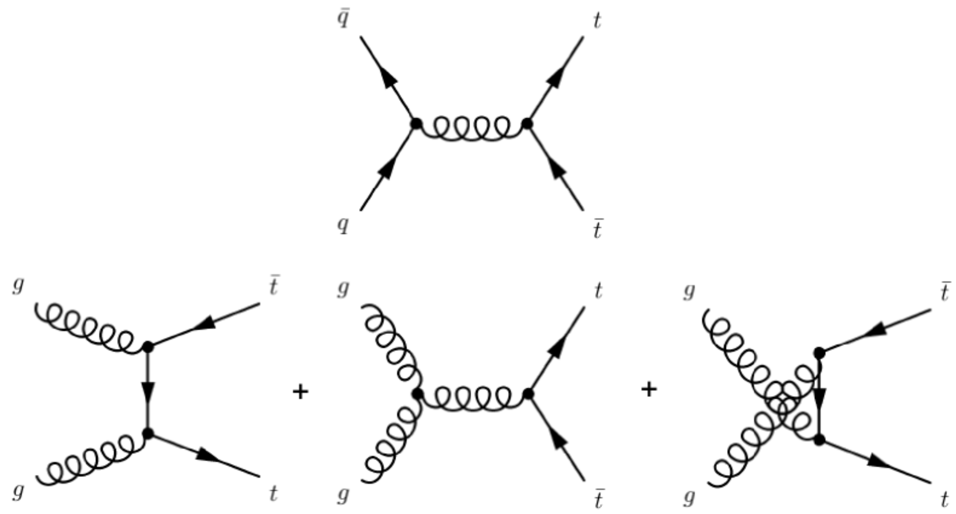

Figure 2.5.: Leading order Feynman diagrams for the production of $t\bar{t}$ pairs. The upper plot shows the production via quark-antiquark annihilation and the lower plots that for gluon-gluon fusion.

At the LHC which is a pp collider, the top quark pair production is dominated by gluon-gluon fusion while the $q\bar{q}$ annihilation dominates at the $p\bar{p}$ collider Tevatron. This effect can be explained by the different type of collider as well as the higher centre-of-mass energy at the LHC. At the LHC with a centre-of-mass energy of $\sqrt{s} = 7$ TeV, a smaller momentum fraction of the partons is needed to produce top quark pairs compared to the Tevatron with $\sqrt{s} = 1.96$ TeV. For small momentum fractions, the gluon parton distribution function dominates over the quark/antiquark PDFs, see Fig.2.4.

Single Top Production

Besides the top quark pair production, single tops are produced via the weak interactions in three different channels: the s-channel, t-channel and the associated Wt-production. The leading-order Feynman diagrams are depicted in Fig. 2.6.

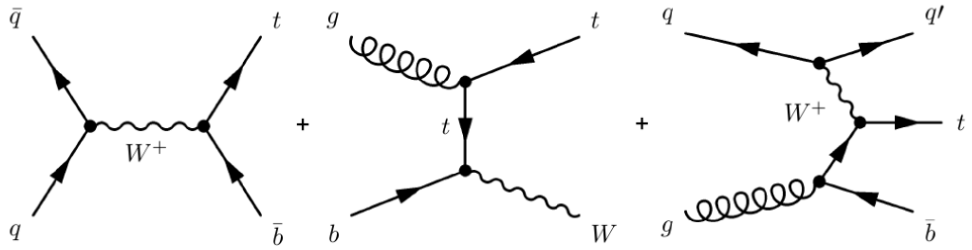

Figure 2.6.: Feynman diagrams for the production of single top quarks in the s-channel (left), the associated Wt-production (middle) and t-channel (right).

Single top quark production has been observed in 2009 at the Tevatron [18, 19]. After the discovery of top quarks pairs, it took approximately 14 years to discover the production of single top quarks because of the much smaller cross section and the smaller signal to background ratio. The measurement of the single top cross section enabled the first direct measurement of the CKM matrix element $|V_{tb}|$.

2.2.3. Top Quark Decay

Due to its large mass, the top quark has a short lifetime of $\tau_t \approx 5 \cdot 10^{-25}$ s and decays before it can hadronise. Therefore no bound states with top quarks exist. According to the CKM matrix, the top quark decays via the weak interaction almost exclusively into a W-boson and a b-quark with $|V_{tb}| = 0.999152^{+0.000030}_{-0.000045}$ [4]. The final state of $t\bar{t}$ pairs can be classified by the decay products of the two W-bosons. The W-boson can decay either leptonically into a charged lepton and its corresponding neutrino, or hadronically into two quarks. Neutrinos cannot be directly measured in the detector but are identified by missing transverse energy. One distinguishes the following channels:

- **dileptonic:** In the dilepton channel, both W-bosons decay leptonically. The signal consists of two leptons, missing transverse energy and two b-jets. The dilepton channel cannot be fully reconstructed due to the two neutrinos. The branching ration BR for the dilepton channel is BR$\approx$ 4.94% assuming only decays into muons and electrons. Furthermore, the background contribution to the dilepton channel is very small.

- **lepton + jets** The signal in the lepton + jets channel consists of four jets, one high-p_T lepton and missing transverse energy. The branching ratio for the lepton + jets channel is relatively large BR $\approx$ 34.9%, taking also the decay of taus into electrons and muons into account. The lepton + jets channel is also called the *golden channel* due to its good signal over background ratio.

- **hadronic:** In the hadronic channel, both W-bosons decay hadronically leading to six jets in the final state. The channel has a high BR $\approx$ 44.44% but also a large background due to QCD multijet production.

2.2.4. Charge Asymmetry in Top Quark Pair Production

At leading order, the production of $t\bar{t}$ pairs is symmetric under charge conjugation. At next-to-leading order an asymmetry arises in the quark-antiquark production of $t\bar{t}$ pairs. The interference between the Born and box diagram leads to a positive asymmetry contribution while the interference between initial and final state radiation leads to a small negative asymmetry contribution. The interfering Feynman diagrams are shown in Fig. 2.7. It is predicted that the top quark is preferentially emitted in the direction of the incoming quark and the antitop quark in the direction of the incoming antiquark. The production of $t\bar{t}$ pairs via gluon-gluon fusion remains symmetric.

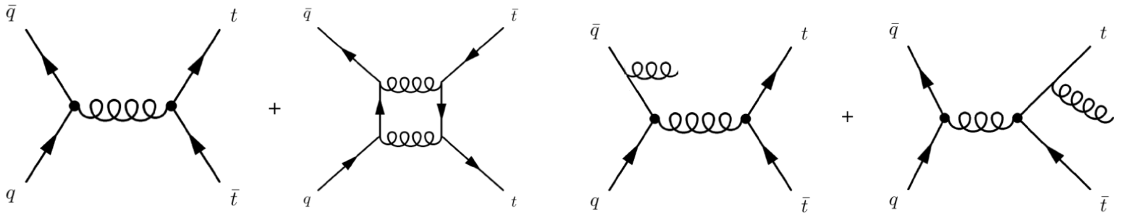

(a) $q\bar{q} \rightarrow t\bar{t}$ (b) $q\bar{q} \rightarrow t\bar{t}g$

Figure 2.7.: Interfering Born and box level diagrams (a) and initial and final state radiation diagrams (b).

Charge Asymmetry at the Tevatron

At the $p\bar{p}$ collider Tevatron the charge asymmetry can be measured as a forward-backward asymmetry A_{FB} which is defined as:

$$A_{\mathrm{FB}}^{t\bar{t}} = \frac{N(\Delta Y > 0) - N(\Delta Y < 0)}{N(\Delta Y > 0) + N(\Delta Y < 0)}, \qquad \text{with} \quad \Delta Y = y_t - y_{\bar{t}} \; .$$

The theoretical QCD prediction has been calculated with the Monte Carlo generator MC@NLO assuming a top quark mass of $m_t = 172.5$ GeV: $A_{\mathrm{FB}}^{t\bar{t}} = 0.058 \pm 0.009$. CDF has measured the forward-backward asymmetry as a function of the invariant $t\bar{t}$ mass $M_{t\bar{t}}$ with an integrated luminosity of $\mathcal{L} = 5.3$ fb^{-1} at a centre-of-mass energy of $\sqrt{s} = 1.96$ TeV [20]. The distribution is depicted in Fig. 2.8.

For low masses $M_{t\bar{t}} < 450$ GeV, the theoretical prediction and the measured data agree very well within the uncertainties, whereas for masses $M_{t\bar{t}} > 450$ GeV, an excess of data over the theoretical prediction is measured. Furthermore, the rapidity distributions ΔY at reconstruction level are shown in Fig. 2.9 for (a) $M_{t\bar{t}} < 450$ GeV and (b) $M_{t\bar{t}} > 450$ GeV. Good data/Monte Carlo agreement is achieved for low $M_{t\bar{t}}$ while the data distribution for $M_{t\bar{t}} > 450$ deviates from the Standard Model prediction.

To compare the measured forward-backward asymmetry with the theoretical prediction, the

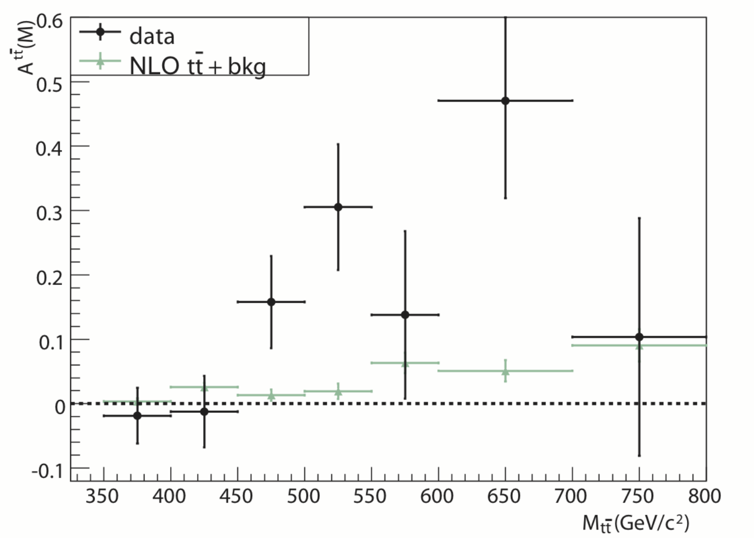

Figure 2.8.: Top forward-backward asymmetry as a function of the invariant $t\bar{t}$ mass [20].

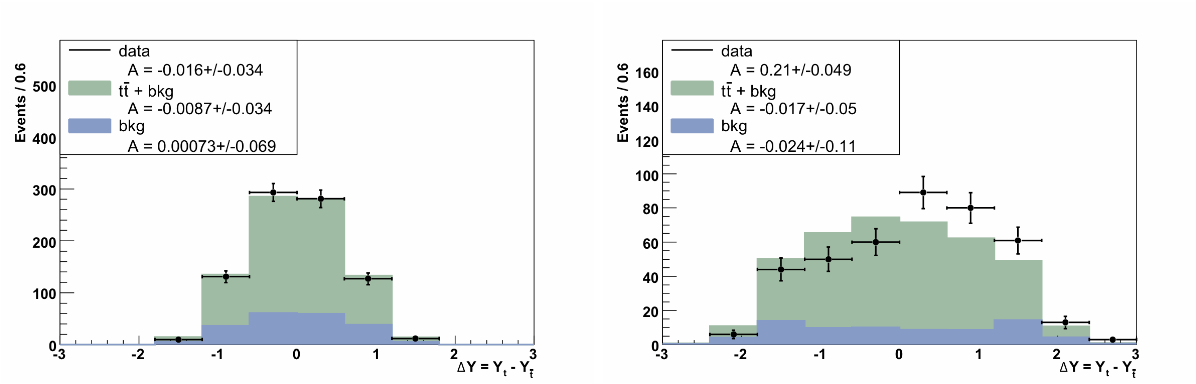

(a) $M_{t\bar{t}} < 450$ GeV

(b) $M_{t\bar{t}} > 450$ GeV

Figure 2.9.: ΔY distributions for a $t\bar{t}$ mass $M_{t\bar{t}}$ smaller (a) and larger (b) than 450 GeV [20].

background is subtracted and an unfolding procedure was applied to correct for detector acceptance and resolution effects. The obtained forward-backward asymmetry for the low and high mass region, $M_{t\bar{t}} < 450$ GeV and $M_{t\bar{t}} > 450$ GeV are shown in Fig. 2.10 together with the theoretical prediction.

For $M_{t\bar{t}} > 450$ GeV, the measured partonic forward-backward asymmetry is:

$$A_{t\bar{t}}^{\text{meas}} = 0.475 \pm 0.114 \ ,$$

which is 3.4 σ deviations larger than the next-to-leading order QCD prediction of 0.088 ± 0.013. The DØ collaboration published results with data corresponding to an integrated luminosity of $\mathcal{L} = 5.4 \text{ fb}^{-1}$ which also show deviations from the SM with a significance of three sigma [21]. The

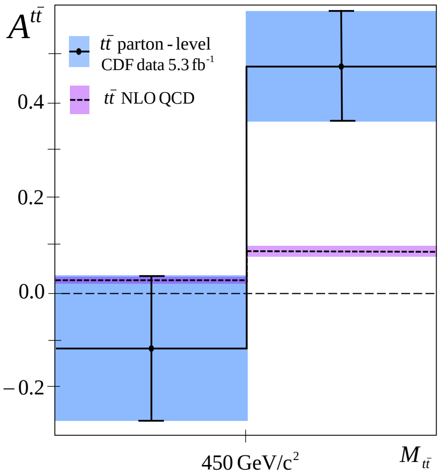

Figure 2.10.: Measured partonic top forward-backward asymmetry for $M_{t\bar{t}}$ smaller and larger than 450 GeV and the NLO prediction [20].

CDF collaboration published a new measurement of the forward-backward asymmetry with the full Run II dataset, corresponding to an integrated luminosity of $\mathcal{L} = 8.7\ \text{fb}^{-1}$. The latest results still show a large asymmetry in the high invariant $t\bar{t}$ mass region but with lower significance:

$$A_{t\bar{t}}^{\text{meas}} = 0.296 \pm 0.067\ .$$

Charge Asymmetry at the LHC

Recently, the top charge asymmetry has been measured with the ATLAS detector at the LHC. As the LHC is a proton-proton collider and therefore has a symmetric initial state, no forward-backward asymmetry can be measured. It is predicted at the LHC that antitops are centrally produced while top quarks are produced on average at higher rapidities. The charge asymmetry observable is defined as:

$$A_C = \frac{N(\Delta|Y| > 0) - N(\Delta|Y| < 0)}{N(\Delta|Y| > 0) + N(\Delta|Y| < 0)}, \qquad \text{with } \Delta|Y| = |Y_t| - |Y_{\bar{t}}|\ .$$

Compared to the Tevatron only a small charge asymmetry is expected because the main production mechanism for $t\bar{t}$ pairs is gluon-gluon fusion which is symmetric under the exchange of t and $\bar{t}$. The theoretical prediction for the charge asymmetry is $A_C = 0.006 \pm 0.002$ (MC@NLO). Using data of $\sqrt{s} = 7$ TeV pp collisions with a corresponding integrated luminosity of $\mathcal{L} = 1.04\ \text{fb}^{-1}$, the charge asymmetry was measured to be:

$$A_C = -0.018 \pm 0.028(\text{stat.}) \pm 0.023(\text{syst.})\ \text{(ATLAS) [22]}$$

which is consistent with the Standard Model prediction. The CMS collaboration recently published an analysis using a dataset of $\mathcal{L} = 5.0\ \text{fb}^{-1}$ in the lepton + jets channel. The measured value

$$A_C = 0.004 \pm 0.010(\text{stat.}) \pm 0.011(\text{syst.})\ (\text{CMS})\ [23]\ ,$$

is in agreement with the SM prediction $A_C^{\text{theory}} = 0.0115 \pm 0.0006$ [24].

Charge Asymmetry Beyond the SM

A wide range of models like axigluons, extra-dimensions, new heavy gauge bosons and diquarks have been presented to explain the anomalous forward-backward asymmetry measured at the Tevatron. In Fig. 2.11 the predicted inclusive partonic charge asymmetries at the Tevatron and LHC for several models beyond the SM are shown. Detailed descriptions of the models can be found in [25, 26, 27, 28]. The predictions are overlaid with the measured forward-backward asymmetry at the Tevatron (CDF and DØ) and the measured charge asymmetry at the LHC (ATLAS and CMS). The solid lines represent the measured central value for each experiment and the dashed areas are the 1 σ-uncertainty regions. Furthermore the SM prediction is indicated.

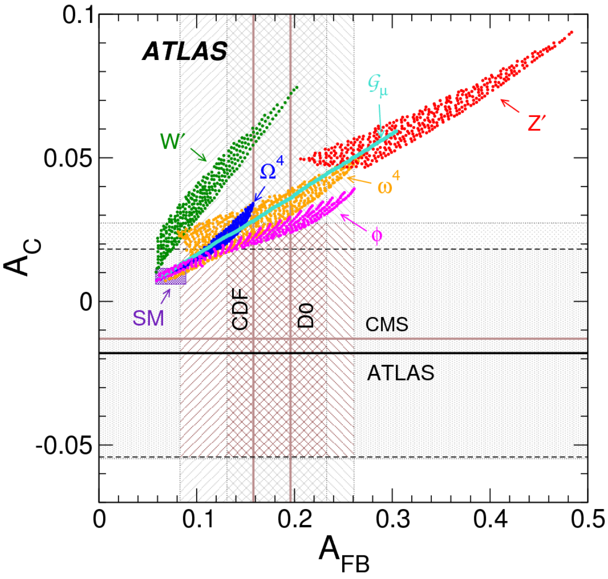

Figure 2.11.: Measured charge asymmetry at the LHC vs. the forward-backward asymmetry at the Tevatron. Furthermore, the predicted charge asymmetries for different theoretical beyond-the-SM-models are shown.

Promising models for the explanation of the large forward-backward asymmetry are those including a new gauge boson W', diquarks or axigluons G_μ.

2.2.5. Top Flavour Violating Resonances

The challenge for new models aiming to explain the large forward-backward asymmetry measurement at the Tevatron is to preserve the total $t\bar{t}$ cross-section and the invariant $t\bar{t}$ mass distribution which is in agreement with SM predictions. One distinguishes two different models: s-channel exchange of a vector mediator and t-channel exchange of flavour violating mediators. This flavour violating mediators can be either Z' or W' gauge bosons or coloured particles. The t-channel exchange model has only a small contribution to the $t\bar{t}$ cross-section and is therefore chosen.

In the following, the production of a new top flavour violating particle M [29, 30, 31], either a new gauge boson W' or a diquark (Φ) as part of a colour triplet model, in association with a top quark will be considered [29]. The production of the gauge boson Z' will not be considered here since the measured charge asymmetry disfavours a Z' at 2-3 σ (see Fig. 2.11). The t-channel Feynman diagram for the $t\bar{t}$ production is shown in Fig. 2.12 (a). Furthermore, the Feynman diagrams for the single M production are depicted in Fig 2.12 (b)-(d). Only the triplet resonance can be produced via the u-channel. Depending on the type of model, the new particle is either produced in association with a top quark or an antitop quark. The W' is produced in association with a top quark ($qg \to W't$), while the triplet resonance is produced with an antitop quark ($qg \to \Phi\bar{t}$).

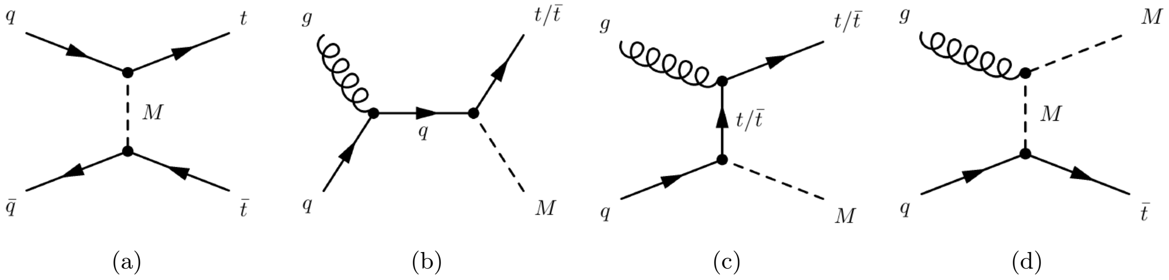

Figure 2.12.: Feynman diagrams for the production of a $t\bar{t}$-pair via t-channel exchange of the new particle M (a) and for the production of M via s-, t- and u-channel (b)-(d).

The new particle M couples only to the top quark and light quarks, i.e up and down quark. The Lagrangians for the singlet and triplet resonance are:

$$\mathcal{L}_{W'} = \frac{1}{\sqrt{2}}\bar{d}\gamma^{\mu}g_R P_R t W'_{\mu} + \text{h.c.} \tag{2.2}$$

$$\mathcal{L}_{\Phi} = \bar{t}^c T^a_r (g_L P_L + g_R P_R) u \Phi^a + \text{h.c.} \tag{2.3}$$

The production cross section of the colour singlet or triplet depends on the coupling to the $t/\bar{t}$ and to the u and d quark. Assuming a unit coupling in the Lagrangian 2.2, 2.3, the leading order cross-sections for the singlet and triplet resonance can be found in Tab. 5.1 for different masses.

If the mass of the new particle is larger than the top quark mass, it can decay into a top or antitop quark and a light quark, $M \to t/\bar{t}q$. It is further assumed that the new particle is not self-conjugated in order to avoid constraints from same sign top production. This results in a $\bar{t}j$ or tj resonance in $t\bar{t}$ + jet events. In contrast to the Tevatron, the resonance at the LHC is dominantly in either tj or $\bar{t}j$ assuming baryon number conservation. For the colour singlet W', the resonance dominates in the $\bar{t}j$ system while a tj resonance is expected for the colour triplet model. The Feynman diagrams for the decay of the colour singlet and triplet are shown in Fig. 2.13.

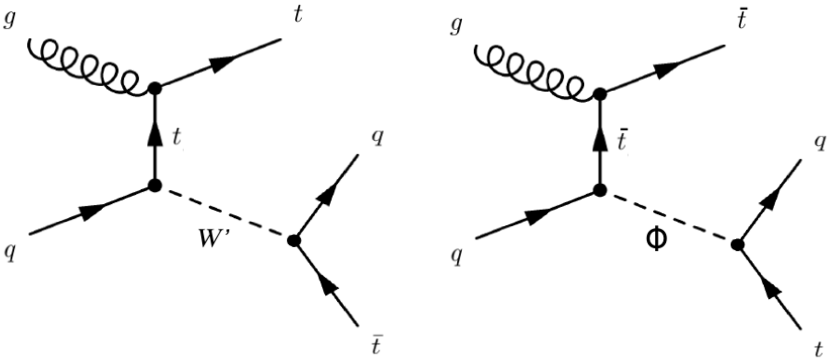

(a) singlet (b) triplet

Figure 2.13.: Feynman diagrams for the decay of the new singlet (a) and triplet (b) resonance.

In the following, the lepton + jets decay channel of $t\bar{t}$ pairs will be assumed for all studies. Therefore signal events contain five jets, one high-p_T lepton and missing transverse energy.

CDF has published results of the search for a top + jet resonance in $t\bar{t}$ + jet(s) events. The analysis has been performed in the lepton + jets channel using data of an integrated luminosity of $\mathcal{L} = 8.7\ \mathrm{fb}^{-1}$ [32]. No deviations from the SM prediction have been found and upper limits on the cross-section for different resonance masses have been set. The upper limits on the cross-section can be found in Fig. 2.14. Specific models can be excluded by setting limits on the mass-coupling space. The excluded regions in mass-coupling space for the singlet and triplet resonance are depicted in Fig 2.15. Assuming $g_R = 1$, a singlet with $m_{W'} < 270$ GeV and a coloured triplet with $m_\Phi < 200$ GeV can be excluded.

The CMS collaboration recently presented a search for the production of a W' boson with $\mathcal{L} = 5.0\ \mathrm{fb}^{-1}$ of pp-collisions at $\sqrt{s} = 7$ TeV [33]. No excess above the SM prediction have been observed and limits on the mass of the W' have been set. W' models with a coupling constant of $g_R = 2$ are excluded at 95% CL for W' masses below 840 GeV.

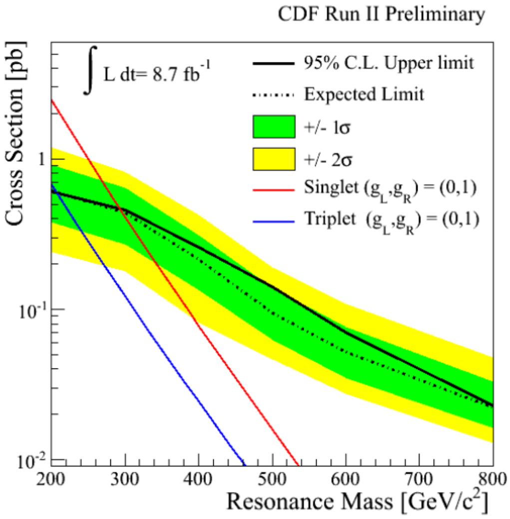

Figure 2.14.: Upper cross-section limits at 95% CL for the production of a new mediator M as a function of its mass.

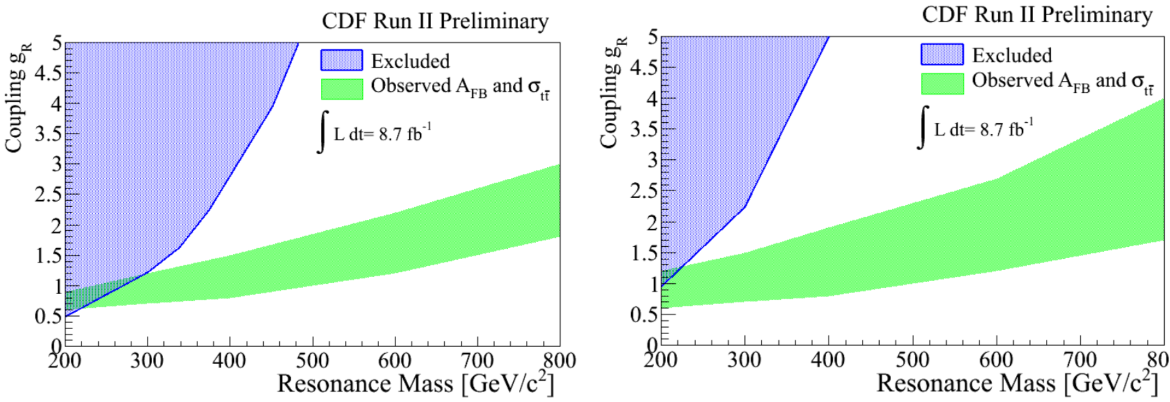

(a) singlet (b) triplet

Figure 2.15.: Excluded regions in mass-coupling space for a singlet (a) and triplet (b) resonance as a function of its mass. In addition, the region which is consistent with the $t\bar{t}$ cross section measurement and the anomalous A_{FB} is shown.

3. Experimental Setup

The *Large Hadron Collider* (LHC) is the world's largest and most powerful particle accelerator. It has been built to allow high precision measurements of the SM, to verify or exclude the Higgs mechanism, and to explore physics beyond the SM. In this chapter, the LHC is described and one of the four main experiments, the ATLAS detector and its components are introduced.

3.1. The Large Hadron Collider

The LHC is a proton-proton (pp) collider which is located at CERN (*Conseil Européen pour la Recherche Nucléaire*) in Geneva [34, 35]. Furthermore, lead ions can be brought to collision in the LHC. The two beam pipes of the LHC are situated in the previous tunnel of the *Large Electron Positron* collider in which electrons and positrons were brought to collisions with a maximum centre-of-mass energy of 209 GeV from 1989 to 2000. The tunnel has a circumference of approximately 27 km. The design centre-of-mass energy of the LHC is $\sqrt{s} = 14$ TeV. Until the end of 2011, the LHC ran at centre-of-mass energy of 7 TeV. For the 2012 run, the LHC has been upgraded to $\sqrt{s} = 8$ TeV. The expected event rate $\frac{\mathrm{d}N}{\mathrm{d}t}$ for a process with cross section σ is:

$$\frac{\mathrm{d}N}{\mathrm{d}t} = \sigma \cdot L \ ,$$

where the instantaneous luminosity L is defined as

$$L = \frac{n_b N_1 N_2 f}{4\pi \sigma_x \sigma_y} \ .$$

n_b is the number of bunches, N_1 and N_2 the number of particles per bunch in beam 1 and 2, f the revolution frequency and σ_x and σ_y are the horizontal and vertical beam sizes assuming Gaussian beam shapes. The LHC has a design luminosity of 10^{34} $\mathrm{cm}^{-2}\mathrm{s}^{-1}$.

Before being injected in the LHC, the protons are first preaccelerated in the linear collider LINAC2 to 50 MeV and in the BOOSTER to 1.4 GeV. Afterwards the protons are transferred to the Proton Synchroton (PS) which accelerates the protons to an energy of 25 GeV before they enter the Super Proton Synchrotron (SPS). In the SPS, the protons reach an energy of 450 GeV, the LHC injection energy. The proton bunches are then injected in the two beam pipes of the LHC and are accelerated to their final energy. The accelerator chain of the LHC is depicted in Fig. 3.1. Each proton beam consists of 2808 bunches with approximately $1.15 \cdot 10^{11}$ protons per bunch. The separation between the bunches is 25 ns.

The proton bunches are accelerated in the LHC with radio-frequency cavities and deflected by 1232 superconducting dipole magnets to keep them on their circular path. The dipole magnets have a maximum magnetic field of 8.33 T. Furthermore, 392 superconducting quadrupole magnets are installed to focus the beam. Liquid helium is used to cool down the dipole and quadrupole magnets to a temperature of 1.9 K.

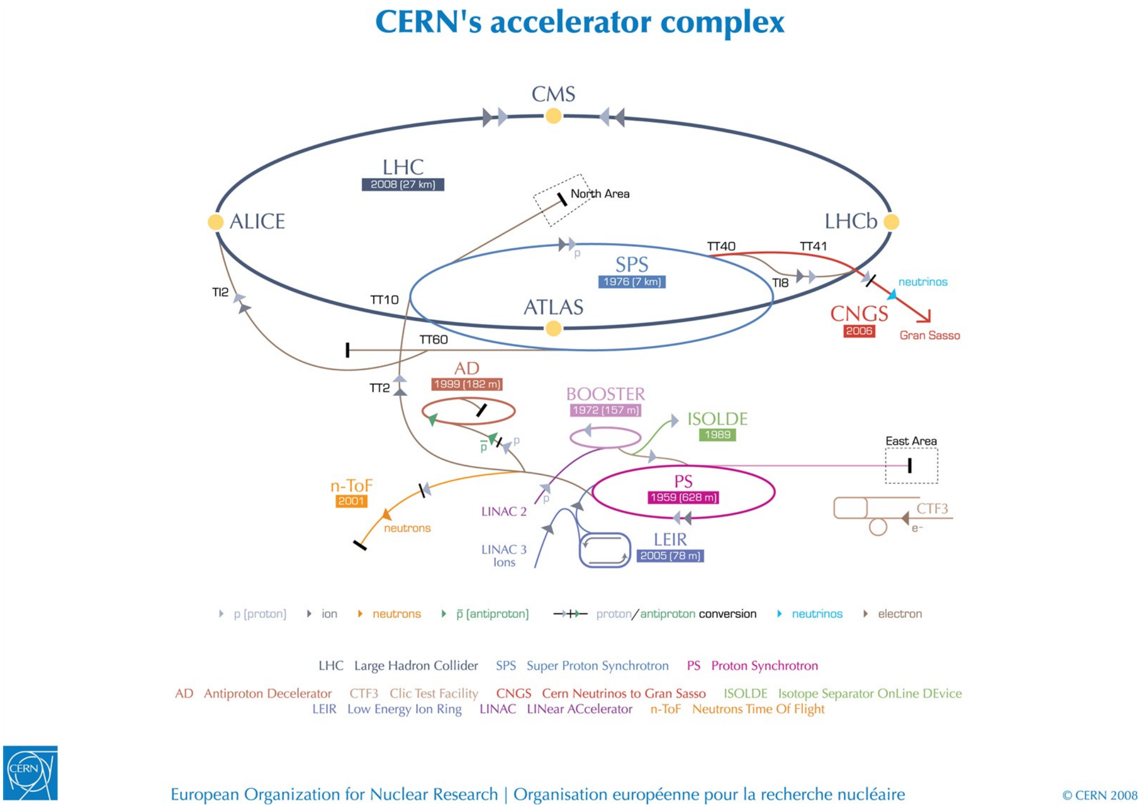

Figure 3.1.: The LHC accelerator chain with the four main experiments [36].

The proton bunches are brought to collision at four different interaction points where the main experiments ALICE, ATLAS, CMS and LHCb are situated. The two general-purpose detectors ATLAS (*A Toroidal LHC Apparatus*) [37] and CMS (*Compact Muon Solenoid*) [38] investigate a wide range of physics topics. ALICE (*A Large Ion Collider Experiment*) [39] was built to investigate the quark-gluon plasma created by lead ion collisions and LHCb [40] studies the matter-antimatter asymmetry in the b-physics sector.

Performance of the LHC

The first protons circulated in the LHC ring in September 2008. Due to a failure of an electrical connection between two magnets which resulted in a helium leakage, several magnets of the LHC were damaged only a few days later. It took more than one year to replace and repair the damaged magnets until the first pp collision at $\sqrt{s} = 900$ GeV could be recorded on November 23rd 2009. The first pp collisions at $\sqrt{s} = 7$ TeV succeeded on March 30th 2010. Hence, the LHC became the world's most powerful particle accelerator. Within 2010, the ATLAS detector recorded 45 pb^{-1} of pp collisions. After the winter shutdown, the LHC started data taking in March 2011 and recorded more than 5 fb^{-1} of data, see Fig. 3.2. Till the end of September 2012, 8 TeV pp collisions have been recorded which correspond to an integrated luminosity of 15 fb^{-1}. The delivered integrated luminosity by the LHC per day and the recorded integrated luminosity by the ATLAS experiment in 2011 and 2012 are shown in Fig. 3.2.

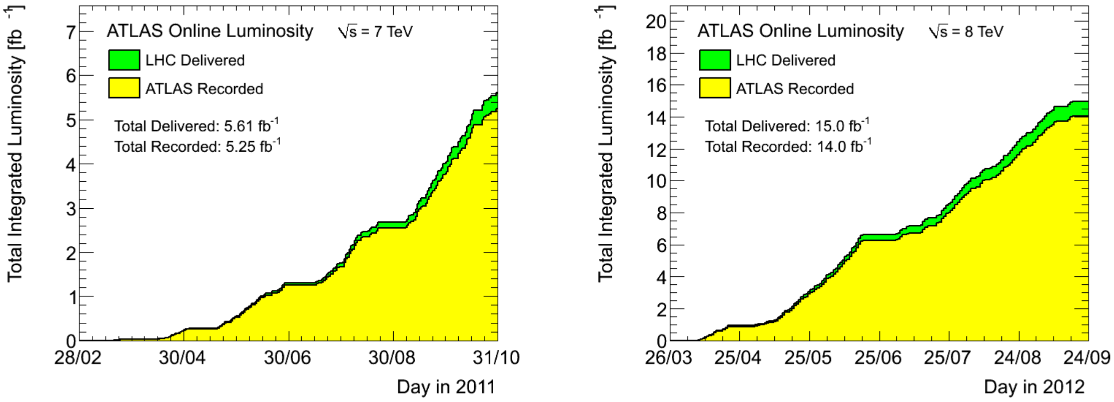

(a) 2011 (b) 2012

Figure 3.2.: Delivered integrated luminosity by the LHC (green) and the recorded integrated luminosity (yellow) by the ATLAS experiment in 2011 (left) and 2012 (right) per day [41].

3.2. The ATLAS Detector

The ATLAS detector is one of the two multi-purpose detectors at the LHC and covers a broad range of physics. It is 44 m long and has a diameter of 25 m with a total weight of 7000 tons. The ATLAS detector has an onion-shell-like structure and consists of four major components: the *Inner Detector*, the *electromagnetic* and *hadronic calorimeters*, the *muon spectrometer* and the *magnet system* which will be described in more detail in the next sections. An overview of the ATLAS detector with its components is shown in Fig. 3.3.

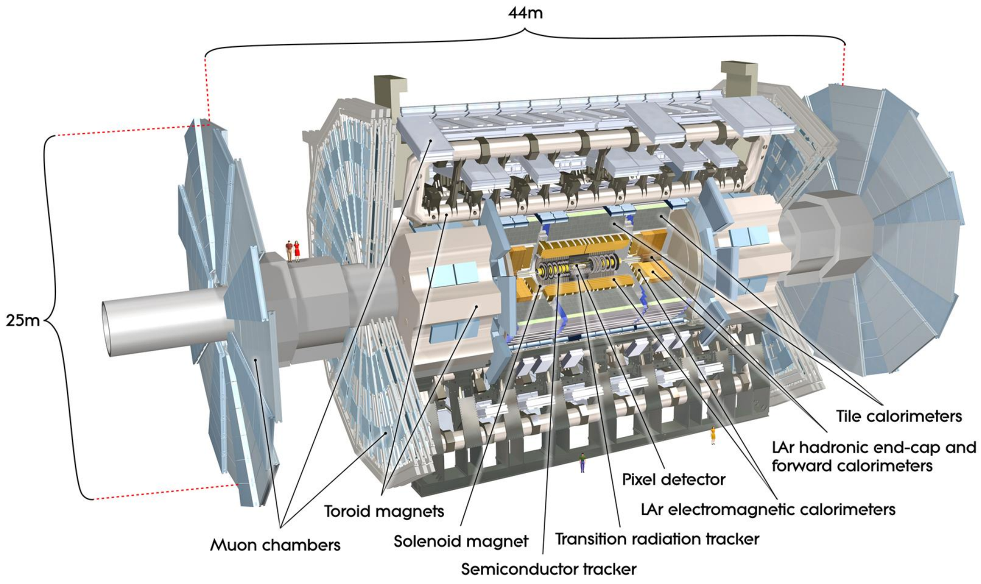

Figure 3.3.: The ATLAS detector with its subcomponents [42].

3.2.1. Detector Coordinates

The ATLAS detector uses a right-handed coordinate system whose origin is placed in the interaction point. The x-axis points towards the centre of the LHC, the y-axis upwards and the z-axis along the beam pipe. Positions within the detector are well-defined by the coordinates (ϕ, η, z), where ϕ is the azimuthal angle in the xy-plane:

$$\phi = \arctan\left(\frac{y}{x}\right) .$$

The pseudorapidity η is defined as

$$\eta = -\ln\left(\tan\left(\frac{\theta}{2}\right)\right) ,$$

where the polar angle θ is measured between the momentum of the particle and the beam-axis. The pseudorapidity is an approximation of the rapidity y for particles with small masses and differences $\Delta\eta$ are invariant under Lorentz transformations. The momentum of particles in the xy plane, the so-called transverse momentum p_T is given by

$$p_\mathrm{T} = \sqrt{p_\mathrm{x}^2 + p_\mathrm{y}^2} ,$$

where p_x and p_y are the momenta in the x and y direction, respectively. Distances between particles are defined in the η-ϕ-plane according to

$$\Delta R = \sqrt{(\Delta\eta)^2 + (\Delta\phi)^2} .$$

3.2.2. The Inner Detector

The track of charged particles and its momentum as well as the primary and secondary vertices are measured in the innermost part of the detector. The inner detector contains the *pixel detector*, the *semiconductor tracker* (SCT) and the *transition radiation tracker* (TRT), see Fig. 3.4. The inner detector is surrounded by a thin superconducting solenoidal magnet with a field strength of 2 T which bends the trajectory of charged particles.

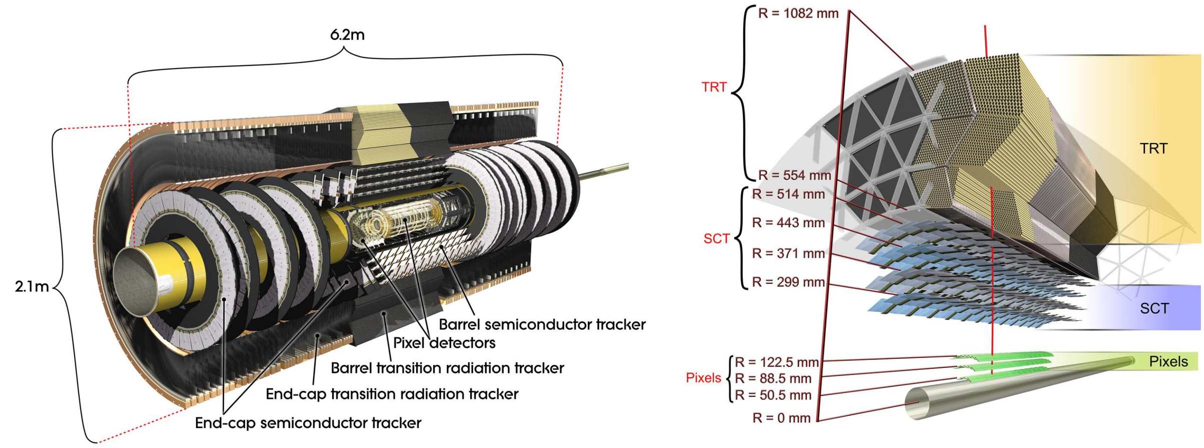

Figure 3.4.: Schematic view of the ATLAS inner detector consisting of the pixel detector, semiconductor tracker and transition radiation tracker [42].

The innermost part of the ATLAS detector is the pixel detector which consists of three barrel layers and three disc layers in the forward and backward direction. The pixel detector enables three measurements of the track of a traversing charged particle in the pseudorapidity range $|\eta| < 2.5$. The approximately 80.4 million pixels, each having a size of $50 \times 400\ \mu\text{m}^2$ are individually read-out by front-end chips via bump-bond connections. The so-called b-layer is the innermost layer of the pixel detector and installed with a distance of approximately 5 cm to the beam. The b-layer is exposed to a very high radiation dose resulting in a decrease of its performance. Therefore, an additional layer, the so-called *insertable b-layer* (IBL) will be installed in the pixel detector during the shutdown in 2013 [43].

The semiconductor tracker affords eight measurements of (R,Φ) for each track and is composed of four barrel layers covering the pseudorapidity range $|\eta| < 1.4$ and nine end-cap layer disks on each side covering $1.4 < |\eta| < 2.5$. Each layer consists of single-sided silicon microstrip detectors which are installed back-to-back at an angle of 40 mrad to provide a three-dimensional measurement.

The transition radiation tracker is the outermost part of the inner detector and consists of straw tubes which are filled with a gas mixture of 70 % Xe, 27 % CO_2 and 3% O_2. The TRT has two end-caps and a central barrel section which results in approximately 36 hits per track. Besides the track measurement, the TRT is also used to distinguish between electrons and pions. If a relativistic charged particle traverses a region with different dielectric constants, it emits photons. The emitted radiation depends on the characteristics of the traversing particle and can therefore be used to distinguish between hadrons (e.g. pions) and electrons.

3.2.3. The Calorimeters

The energy of particles is measured in the *electromagnetic* and *hadronic* calorimeters. Both calorimeters are sampling calorimeters consisting of alternating passive absorber material and active material which measures the deposited energy in the calorimeter. The energy of electrons and photons is measured in the electromagnetic calorimeter. If a high-energetic electron or photon enters the electromagnetic calorimeter, it interacts with the material and produces a particle shower via bremsstrahlung and e^+e^- pair-production. The electromagnetic calorimeter is surrounded by the hadronic calorimeter and measures the energy of hadrons which are originating from the hadronisation of quarks and gluons. Hadrons passing the hadronic calorimeter interact via the strong interaction with the nuclei of the absorber material and produce secondary particles leading to a shower. Besides the measurement of the energy of electrons, photons, τ-leptons and jets, the calorimeters are an essential ingredient for the determination of the missing transverse energy originating from neutrinos.

The number of particles, N, produced in the shower is proportional to the energy E of the incoming particle and follows Poisson statistics. Therefore, the energy resolution of the calorimeters is parametrized as

$$\frac{\sigma_E}{E} = \frac{a}{\sqrt{E}} \oplus \frac{b}{E} \oplus c \, .$$

The constant term c accounts for systematic uncertainties due to miscalibration of the detector as well as dead detector material, and the noise is described by the term b.

An overview of the calorimeter system in ATLAS is shown in Fig. 3.5. The electromagnetic calorimeter covers the pseudorapidity range $|\eta| < 3.2$ and is divided into a barrel region and two end-caps. Due to its high density, lead is chosen as absorber and liquid Argon (LAr) is used as active material. The electromagnetic calorimeter has a total thickness of 24 and 26 radiation lengths in the barrel and end-caps respectively to ensure that the traversing particles deposit all of their energy.

The hadronic calorimeter can be divided into three parts: the tile calorimeter, the liquid Argon end-caps and forward calorimeter which cover a pseudorapidity range of $|\eta| < 4.9$. To minimize punch-through into the muon system, the hadronic calorimeter has a total thickness of more than eleven radiation lengths. The tile calorimeter ($|\eta| < 1.7$) uses iron plates as absorber and scintillating tiles as active material. In the hadronic end-caps (HEC) as well as for the forward calorimeter (FCAL) LAr is used as passive absorber. The HEC consists of two copper wheels on

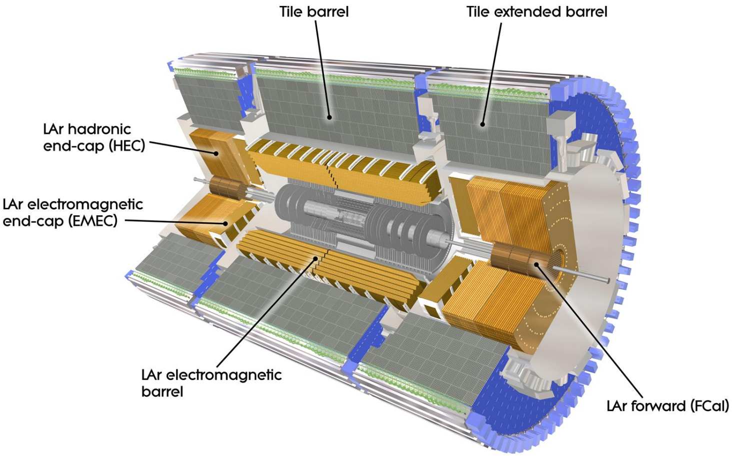

Figure 3.5.: Overview of the electromagnetic and hadronic calorimeters in the ATLAS detector [42].

each side, separated by a thin gap of 8.5 mm in which the liquid argon as well as the read-out wires are contained. The FCAL is contained in the HEC and consists of three sections using copper as absorber for the innermost layer and tungsten for the two outermost layers.

3.2.4. The Muon Spectrometer

Heavy charged particles penetrating through matter, loose energy due to ionization and excitations of the atoms. The average energy loss per distance is described by the Bethe-Bloch formula [4]

$$-<\frac{\mathrm{d}E}{\mathrm{d}x}>=4\pi N_A r_e^2 m_e c^2 z^2 \frac{Z}{A}\frac{1}{\beta^2}\left[\ln\left(\frac{2m_e c^2\gamma^2\beta^2 T_{\max}}{I^2}\right)-\beta^2-\frac{\delta}{2}\right] ,$$

where N_A is the Avogadro constant, r_e and m_e the classical radius and the mass of the electron, z the charge of the interacting particle, Z and A atomic and mass number of the absorbing material, I the mean excitation energy, $T_{\max}$ the maximum energy transfer per collision and δ the density correction. The energy loss has a minimum at $\beta\gamma \approx 3.5$ which is approximately independent of the absorber material. High-energetic muons with a momentum of 1 - 100 GeV are called minimum ionizing particles because their energy loss per distance is close to its minimal value. Therefore, muons deposit only a small amount of their energy in the detector and their momentum is measured in the outermost part of the ATLAS detector: the muon spectrometer. The muon spectrometer comprises four different types of detectors which are embedded in a superconducting toroid magnet with a peak field strength of 4 T to deflect the muons. The momentum of muons is measured with high precision in the monitored drift tubes (MDTs) and cathode strip chambers (CSCs). Resistive plate chambers (RPCs) and thin gap chambers (TGCs) are used for fast triggering of muon events. The MDTs are arranged in three layers in the barrel region and cover a pseudorapidity range of $|\eta| < 2.0$. Due to the higher particle flux with larger $|\eta|$, the innermost layer of the endcaps ($2.0 < |\eta| < 2.7$) uses the CSCs which are multiwire proportional chambers using cathode strips as readout. The trigger chambers provide well-defined p_{T} thresholds as well as a measurement of the muon track orthogonal to the measurement in the MDTs and CSCs. The RPCs are used for triggering events in the barrel region and the TGCs in the endcaps.

3.2.5. The Trigger System

The high luminosity of the LHC leads to a bunch crossing rate of 40 MHz with approximately 25 interactions per crossing. In order to store only the data which are of interest, a three level trigger system is used within ATLAS and reduces the data to 200 Hz.

The level-1 trigger (LV1) is hardware based and uses only a subset of the detector information from the calorimeters and the muon chambers. The LV1 is sensitive to high p_{T} muons, electrons, photons and jets as well as large missing transverse energy. Within a latency of 25 μs the LV1 decides if an event is rejected or further analysed, reducing the rate to 75 kHz. Before being passed to the high-level trigger, regions of interest (RoI) in the η-ϕ plane are defined.

The high-level trigger consists of the level-2 trigger (LV2) and the Event Filter (EF) and is software based. The LV2 investigates the RoI using the full granularity information of all subdetectors. Within 40 ms a decision is made, reducing the rate to 3 kHz. The full event information is provided by the EF which reconstructs and analyses the event signature based on offline algorithms resulting in a processing time of 4 s per event. Events passing all trigger levels are written to streams which are stored permanently.

4. Object Definitions

Particles traversing the ATLAS detector produce characteristic signatures which are used to identify the particles. Electrons, muons and jets are identified and reconstructed using information from the inner detector, calorimeters and the muon spectrometer. In the following, the object definitions optimized for the 2011 collision data are presented.

4.1. Jets

Jets are reconstructed with the anti-k_T [45] algorithm with a radius parameter of $\Delta R = 0.4$. Topological clusters at the electromagnetic scale, built from calorimeter cells, are used as input for the jet algorithm. Based on the transverse momentum and the pseudorapidity, the reconstructed jets are then calibrated to the hadronic scale.
Jets are required to have a minimum transverse momentum of $p_\mathrm{T} > 25$ GeV and a pseudorapidity of $|\eta| < 2.5$. To reduce the number of pile-up jets, a cut on the jet vertex fraction (JVF) is applied: $|\mathrm{JVF}| > 0.75$. The JVF is defined as the ratio of the p_T of the matched tracks from the primary to the total number of matched track p_T in the jet. In the jet-overlap removal, jets are removed from an event if they overlap within $\Delta R > 0.2$ with an electron (see below for object definitions).

b-Tagging

The identification of jets originating from a b-quark is crucial for top quark ($t \rightarrow Wb$) and Higgs ($H \rightarrow bb$) analyses to separate the signal from background contamination. b-tagging algorithms discriminate between light and b-flavored jets exploiting the long lifetime of B-mesons of about 10^{-12} s. Therefore, B-mesons decay after a flight length of approx. 1 mm, leading to a displaced secondary vertex and a large impact parameter. In this analysis, the neural network-based algorithm MV1 was used which combines the weights of three different b-taggers: SV0, IP3D and JetFitterCombNN. Further information on the different b-tagging algorithms can be found in [46]. The performance of the algorithm is characterized by its efficiency to correctly identify b-jets and the rejection efficiency defined as the inverse of the rate with which light jets are misidentified as b-jets. For this analysis, the 70% working point of the MV1 tagger is chosen.

4.2. Electrons

Electrons are reconstructed from energy deposits in the electromagnetic calorimeter via the cluster-based sliding window algorithm [47]. Clusters are only taken into account if they can be matched to a track in the inner detector. Electrons are required to be detected in the central region of the detector $|\eta_{\text{cluster}}| < 2.47$, excluding the transition region between the barrel and endcaps ($1.37 < |\eta_{\text{cluster}}| < 1.52$). In addition, the transverse energy of the electron $E_{\text{T}} = E_{\text{cluster}} / \cosh(\eta_{\text{track}})$ has to be larger than 25 GeV and a cut on the z_0 position with respect to the primary vertex is applied $|z_0| < 2$ mm. To suppress QCD multijet background, electrons are required to be isolated. Therefore, cuts on the deposited transverse energy in a cone of $\Delta R = 0.2$ (Etcone20) around the electron and the transverse momentum in a cone of $\Delta R = 0.3$ (ptcone30) are imposed. Further separation between electrons and jets is achieved if electrons satisfy the `tight++` quality criteria. If the distance ΔR between an electron and a jet is smaller than 0.4 after the jet-overlap removal, the electron is discarded.

4.3. Muons

Muons in the ATLAS detector can be reconstructed with four different algorithms depending on the available information of the different detector subsystems. In top quark analyses, muons are reconstructed with the `MUIDcombined` algorithm which combines the track in the muon spectrometer with its associated track in the inner detector via a global fit. The quality requirements on the inner detector track can be found in the recommendations of the muon combined performance group [48]. In addition, only muons with $p_{\text{T}} > 20$ GeV and $|\eta| < 2.5$ are considered. Events with large JVF scale factors are rejected if muons fulfill $|z_0| < 2$ mm with respect to the primary vertex. To reduce the amount of non-prompt muons, i.e. muons which are produced in the decay of hadrons inside a jet, tight isolation criteria are defined. Tight muons have to fulfill the following requirements: ptcone30 < 2.5 GeV and etcone20 < 4 GeV. Furthermore the distance between a jet ($p_{\text{T}} > 25$ GeV) and a muon in the $\eta - \phi$ plane has to be at least $\Delta R > 0.4$.

4.4. Missing Transverse Energy

The production of top pairs in the lepton + jets channel results in a large amount of missing transverse energy $E_{\text{T}}^{\text{miss}}$ due to the neutrino which escapes the dectector. The imbalance of the transverse energy in the detector is used to measure $E_{\text{T}}^{\text{miss}}$ based on the deposited energy in the calorimeters and the muon momentum. For the calculation of $E_{\text{T}}^{\text{miss}}$, electrons with a transverse momentum of $p_{\text{T}} > 10$ GeV are considered. Jets fulfilling the object definitions described above as well as soft jets with $7 \text{ GeV} < p_{\text{T}} < 20$ GeV at the electromagnetic scale are included in the definition of $E_{\text{T}}^{\text{miss}}$. The contribution of the muons to the $E_{\text{T}}^{\text{miss}}$ is determined by the p_{T} measured in the muon spectrometer, including all muons in the pseudorapidity range $|\eta| < 2.7$. In addition, calorimeter cells with deposited energy not associated to a high p_{T} object, are included in the so-called cell-out term. Hence, the missing energy in x and y direction is composed as follows:

$$-E_{\mathrm{x,y}}^{\mathrm{miss}} = E_{\mathrm{x,y}}^{\mathrm{RefElectron}} + E_{\mathrm{x,y}}^{\mathrm{RefMuon}} + E_{\mathrm{x,y}}^{\mathrm{RefJet}} + E_{\mathrm{x,y}}^{\mathrm{RefSoftJet}} + E_{\mathrm{x,y}}^{\mathrm{CellOut}} \, ,$$

resulting in the definition of the missing transverse energy

$$E_{\mathrm{T}}^{\mathrm{miss}} = \sqrt{\left(E_{\mathrm{x}}^{\mathrm{miss}}\right)^2 + \left(E_{\mathrm{y}}^{\mathrm{miss}}\right)^2} \, .$$

5. Process Modelling and Data Sample

Monte Carlo (MC) generators play an important role in high energy physics. MC simulations are used to estimate the background, predict experimental observables which discriminate between signal and background processes as well as to determine signal selection efficiencies. Furthermore, the detector and the trigger system is optimized with MC simulations. The MC event generators simulate the hard scattering process between two incoming partons, the parton showers in the initial and final state, the hadronisation and decay of the final state particles as well as the underlying event. The underlying event describes the beam remnants and multiple parton interactions. A simulated event is shown schematically in Fig. 5.1.

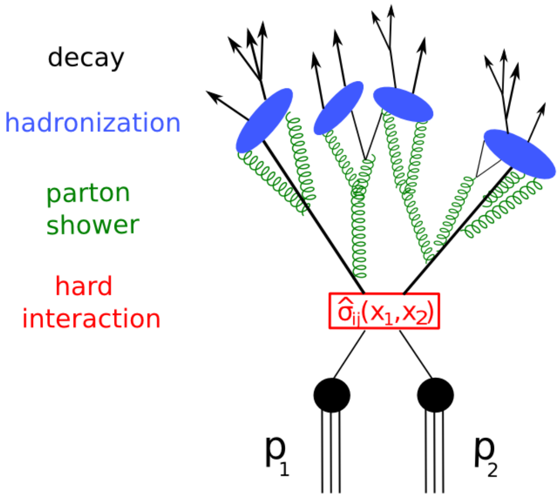

Figure 5.1.: Schematic view of a Monte Carlo simulated event including the hard scattering process, parton shower and hadronisation.

Tree level matrix element generators like Alpgen [49], AcerMC [50], MadGraph [51] and MC@NLO [52] are specialised on the simulation of hard scattering processes via perturbative QCD and interfaced to full event simulation generators, e.g. Pythia [53], Herwig [54] and Sherpa [55]. The full event generators simulate the non-perturbative parton showering, hadronisation and underlying event. Two different approaches for the hadronisation exist: the Lund string fragmentation model which is implemented in Pythia while Herwig and Sherpa use the cluster fragmentation model.

The MC signal and background samples used for the analysis are described in this chapter. Athena software framework [56] version 17 is used to perform the event generation, detector simulation (through GEANT 4 [57]), digitization and reconstruction. All MC samples have been created during the central ATLAS MC11c production with an assumed centre-of-mass energy of $\sqrt{s} = 7$ TeV. The signal samples as well as the $t\bar{t}$ and single top samples are produced with a default top quark mass of $m_t = 172.5$ GeV. Furthermore, the analysed data sample is described in 5.3.

5.1. Signal Modelling

Two types of MC signal samples have been generated using MadGraph and passed through Pythia. The new particle M can either be a colour singlet (W') or a colour triplet diquark. For both particles, seven samples have been generated with masses ranging from 200-800 GeV in 100 GeV intervals. In addition five samples with masses in the range 1000-2000 GeV in 250 GeV step have been generated. For the production of the signal samples, no pair production of the new particle is assumed. Furthermore, the all-hadronic decay channel is not contained in the signal samples. The production cross sections can be found in Tab. 5.1.

Mass [GeV]	Leading order cross section [pb]	
	Color singlet	Color triplet
200	40.20	45.00
300	14.00	17.50
400	5.77	7.91
500	2.64	3.90
600	1.30	2.07
700	0.684	1.15
800	0.372	0.665
900	0.209	0.396
1000	0.121	0.243
1250	0.0338	0.0757
1500	0.0103	0.0254
1750	0.0033	0.0090
2000	0.0011	0.0032

Table 5.1.: Cross sections for the colour singlet and triplet samples.

5.2. Background Modelling

The same signature as that of the new top-flavour violating particle in association with a top quark can also be produced by several background processes. The following processes will be considered as background: $t\bar{t}$ + jets production, W + jets, Z + jets, single-top, diboson and multijet production.

The dominant background for this analysis is the production of $t\bar{t}$ pairs in association with additional jets. These additional jets are produced via initial or final state radiation as well as from underlying events. Furthermore, W + jets events are one of the main background processes. In W + jets events, a single W-boson is produced which decays into a lepton and its corresponding neutrino with additional jets. In Z + jets events, one lepton is not detected and can therefore be measured as missing transverse energy. In the multijet production a jet is misidentified as a lepton and the missing transverse energy can be observed due to jets which are outside the detector acceptance. The contribution of the fake lepton background (QCD multijet) is estimated with a data driven matrix method [22] which is explained in section 5.2.2

5.2.1. Background Monte Carlo Samples

Top Pair Production

The $t\bar{t}$ sample was generated with MC@NLO v4.01 with the CT10 [16] parton distribution functions. MC@NLO is interfaced to Herwig v6.520 and Jimmy v4.31 [58] to simulate the parton showering (fragmentation and hadronization) and the multiple parton interactions. The $t\bar{t}$ sample does not contain the all-hadronic decay mode. The $t\bar{t}$ cross section is normalized to the approximate next-to-next-to leading order (NNLO) prediction value $\sigma_{t\bar{t}} = 166.8^{+16.5}_{-17.8}$ pb, calculated with HATHOR [17] using the MSTW2008 NNLO PDF sets [59].

Single Top Production

Single top production in the t-channel and Wt-production was simulated with MC@NLO using Herwig/Jimmy for the parton shower and underlying event. The s-channel production of single top events was generated using AcerMC v3.8 interfaced with Pythia. For the leading-order (LO) generator AcerMC, the modified LO** PDFs were used, which are implemented in the *Les Houches Accord PDF Interface* [60].

Vector Boson Production With Additional Jets

Vector boson production with additional jets (W + jets, Z + jets) was simulated with the LO generator Alpgen v2.14 interfaced with Herwig and Jimmy. Alpgen includes the CTEQ6L1 [61] parton distribution functions. The partons which are produced in association with a W or Z boson can be either light quarks (W + jets, Z + jets) or heavy quarks ($W + c$ + jets, $W + c\bar{c}$ + jets, $W + b\bar{b}$ + jets and $Z + b\bar{b}$ +jets). In the inclusive W and Z + jets samples, the light quark as well as the heavy quark processes are included. Therefore, in order to avoid double counting, the heavy flavour overlap removal tool [62] is used. The Z + jets and $Z + b\bar{b}$ + jets samples also contain the Drell-Yan contribution from the process $\gamma^* \rightarrow ll$ and takes the Z/γ^* interference into account. The cross sections of the W + jets and Z + jets production are normalized to the NNLO predictions. For the Z + jets samples, the full DY cross sections are used. The shape of the W + jets background is estimated from MC whereas the normalisation of the W + jets background is determined using a data driven method from the W charge asymmetry measurement, see 5.2.2.

Diboson Production

Finally, the production of diboson events (WW, WZ, ZZ) is simulated with Herwig. In all vector boson samples, the NLO cross section predictions are used to obtain the k-factors.

5.2.2. Background Estimation With Data-Driven Methods

Normalisation of W + jets

The normalisation of the W + jets background is estimated from the W charge asymmetry measurement [22]. At the LHC the production of W bosons is charge asymmetric due to the parton distribution functions while the $t\bar{t}$, Z + jets and QCD multijet production is symmetric. Therefore the total number of W events in the pretag sample can be approximated by

$$\begin{aligned} N_{W^+} + N_{W^-} &= \frac{N_{W^+}^{\mathrm{MC}} + N_{W^-}^{\mathrm{MC}}}{N_{W^+}^{\mathrm{MC}} - N_{W^-}^{\mathrm{MC}}}(D^+ - D^-) \\ &= \frac{r_{\mathrm{MC}} + 1}{r_{\mathrm{MC}} - 1}(D^+ - D^-) \ , \end{aligned}$$

where D^+, D^- is the number of data events with a positively or negatively charged lepton. The variable r_{MC} is defined as the ratio of the W^+, W^- cross section $r_{\mathrm{MC}} = \frac{\sigma(pp \to W^+)}{\sigma(pp \to W^-)}$ and calculated from Monte Carlo simulations [63]. The number of W events in the tagged sample can be estimated by:

$$N_{\mathrm{W}}^{\mathrm{tagged}} = N_{\mathrm{W}}^{\mathrm{pretag}} \cdot f_{\mathrm{tagged}} \ ,$$

where f_{tagged} is the probability for a jet to be tagged. The normalisation is applied to the MC sample via scale factors.

QCD Multijet Background

Mis-identified leptons ("fake" leptons) are a non-negligible background for the production of $t\bar{t}$ pairs. Since this background is difficult to model with Monte Carlo simulations, a data driven matrix method was used to estimate the fake lepton background in the μ + jets and e + jets channel [22]. A loose and a tight sample are defined, where the tight sample is a subset of the loose sample by applying additional cuts. The number of events which contain a loose (N_{loose}) and tight lepton (N_{tight}) is given by

$$\begin{aligned} N_{\mathrm{loose}} &= N_{\mathrm{real}}^{\mathrm{loose}} + N_{\mathrm{fake}}^{\mathrm{loose}} \ , \\ N_{\mathrm{tight}} &= \epsilon_{\mathrm{real}} \cdot N_{\mathrm{real}}^{\mathrm{loose}} + \epsilon_{\mathrm{fake}} \cdot N_{\mathrm{fake}} \ . \end{aligned}$$

The factors ϵ_{real} and ϵ_{fake} are the efficiencies of a real and fake lepton to pass the tight selection, i.e.

$$\epsilon_{\mathrm{real}} = \frac{N_{\mathrm{real}}^{\mathrm{tight}}}{N_{\mathrm{real}}^{\mathrm{loose}}} \,, \qquad \epsilon_{\mathrm{fake}} = \frac{N_{\mathrm{fake}}^{\mathrm{tight}}}{N_{\mathrm{fake}}^{\mathrm{loose}}} \,.$$

In order to account for detector acceptance, the signal and background efficiencies are parametrised in $|\eta|$ and p_{T}. The determination of the efficiencies for the μ + jets and e + jets channel are described below. The number of background (fake lepton) events passing the tight lepton selection can then be estimated by:

$$N_{\mathrm{fake}}^{\mathrm{tight}} = \epsilon_{\mathrm{fake}} \cdot N_{\mathrm{fake}} = \frac{\epsilon_{\mathrm{fake}}}{\epsilon_{\mathrm{fake}} - \epsilon_{\mathrm{real}}} \cdot \left(N_{\mathrm{tight}} - \epsilon_{\mathrm{real}} \cdot N_{\mathrm{loose}}\right) \,. \tag{5.1}$$

A weight is applied to each event in the data sample depending on passed selection. According to equation 5.1, the event weight for the loose selection with $N_{\mathrm{loose}} = 1,\ N_{\mathrm{tight}} = 0$ is

$$w_{\mathrm{loose}} = \frac{\epsilon_{\mathrm{fake}}\epsilon_{\mathrm{real}}}{\epsilon_{\mathrm{real}} - \epsilon_{\mathrm{fake}}} \,,$$

and for the tight selection ($N_{\mathrm{loose}} = 1,\ N_{\mathrm{tight}} = 1$):

$$w_{\mathrm{tight}} = \frac{\epsilon_{\mathrm{fake}}(1 - \epsilon_{\mathrm{real}})}{\epsilon_{\mathrm{fake}} - \epsilon_{\mathrm{real}}} \,.$$

Matrix Method in the Muon + jets channel

In the muon channel, the loose sample for the matrix method is the default muon selection except for the isolation criteria described in 4.3. The tight sample contains muons which fulfil in addition the following cuts:

- ptcone30 < 2.5 GeV,
- Etcone20 < 4 GeV.

The signal efficiencies are determined in di-muon data events which are produced in the decay of a Z-boson ($Z/\gamma \to \mu\mu$) using a tag & probe method. The fake efficiencies are estimated in a control region which contains a large amount of QCD events. This control region might be a region with low missing transverse momentum or low transverse W mass. In the μ + jets channel, the control region is defined through the following triangular cut:

- $m_{\mathrm{T}}(W) < 20$ GeV,
- $E_{\mathrm{T}}^{\mathrm{miss}} + m_{\mathrm{T}}(W) < 60$ GeV.

Matrix Method in the Electron + jets channel

Tight electrons are the default electrons with the object definitions described in 4.2. The loose sample contains electrons passing the `Medium++` quality criteria with a veto on the conversion of a photon to electron-positron pairs. The tag & probe method is used to derive the signal efficiencies in the e + jets channel using a sample of $Z/\gamma \rightarrow ee$ data events. The fake efficiencies are measured in a control region with low missing transverse energy ($E_{\mathrm{T}}^{\mathrm{miss}} < 20$ GeV) using samples which contain at least one high-p_{T} jet ($p_{\mathrm{T}} > 25$ GeV) and exactly one loose electron. The jet and electron have to be separated by $\Delta R \geq 0.7$. Monte Carlo simulations are used to estimated the contamination of signal leptons from the decay of a W- or Z-boson in the low $E_{\mathrm{T}}^{\mathrm{miss}}$ region.

5.3. Data Sample

For this analysis, the complete data set recorded during the 2011 run is considered, corresponding to an integrated luminosity of $\mathcal{L} = 4.71$ fb^{-1}. The top good runs list (GRL) [64] was used in order to assure stable data-taking conditions. Depending on the data-taking period, different lepton triggers were used for the single electron and muon channels. Details of the trigger requirements can be found in Tab. 5.2.

period	single electron channel	single muon channel
period B-I	EF_e20_medium	EF_mu18
period J	EF_e20_medium	EF_mu18_medium
period K	EF_e22_medium	EF_mu18_medium
period L-M	EF_e22vh_medium1 OR EF_e45_medium1	EF_mu18_medium

Table 5.2.: Triggers used for the single electron and muon channel in different data taking periods.

6. Event Selection

In this chapter, the event selection optimized for top quark analyses is introduced. Three different control regions are defined to validate the selection and the background modelling. The event yields for the different control regions and distributions of different kinematic variables are presented in chapter 6.3. In addition, matching efficiencies for the event selection are calculated using the signal Monte Carlo samples.

6.1. Signal Region Selection Criteria

Signal events in the lepton + jets channel contain at least five jets, one isolated lepton and missing transverse energy. In order to enhance the signal over the background, the following pre-selection is applied:

- The trigger to the corresponding period has fired, see Tab. 5.2.
- To reject non-collision background, a good primary vertex with at least five tracks associated to it is required.
- In the single electron channel, exactly one electron with $E_{\mathrm{T}} > 25$ GeV and the absence of muons is required. Exactly one muon with $p_T > 20$ GeV and the absence of electrons is required in the muon + jets channel.
- The lepton must match the trigger object which fired the corresponding trigger. The distance between the trigger object and the reconstructed lepton must be smaller than $\Delta R = 0.15$.
- Muons can also be reconstructed as electrons in the detector. Therefore, events are removed if an electron and a muon share an inner detector track.
- Events containing a *bad* jet with $p_{\mathrm{T}} > 20$ GeV are rejected. These jets do not correspond to real energy deposits in the calorimeter. A jet is labelled bad if it fulfils the loose quality requirements on the electromagnetic coherent noise, hadronic end caps and LHC beam conditions, defined in [65]
- At least four jets fulfilling the object criteria described in section 4.1 are required.
- A minimum amount of missing transverse energy of $E_{\mathrm{T}}^{\mathrm{miss}} > 30$ GeV is required in the single electron and $E_{\mathrm{T}}^{\mathrm{miss}} > 20$ GeV in the single muon channel.

- In the single electron channel a transverse mass of the leptonic W-boson $m_{\mathrm{T}}(W)$ of at least 30 GeV is required. A triangular cut of $m_{\mathrm{T}}(W) + E_{\mathrm{T}}^{\mathrm{miss}} > 60$ GeV is applied in the single muon channel. The transverse mass of the W-boson is defined as:

$$m_{\mathrm{T}}(W) = \sqrt{2 p_{\mathrm{T}}^{\ell} p_{\mathrm{T}}^{\nu} (1 - \cos(\phi^{\ell} - \phi^{\nu}))} \ .$$

- Events with data integrity errors in the LAr calorimeter are removed.

In the signal region further criteria on the jets are imposed. The event has to contain at least five jets where at least one jet is required to be b-tagged with the MV1 algorithm using a working point of 70%.

6.2. Truth Matching

The assignment of the reconstructed objects to the decay products of the top-antitop pair and the resonance is done with the KLFitter, see chapter 7.1. In order to evaluate the reconstruction efficiency of the KLFitter, the reconstructed objects need to be identified with their corresponding truth partons. Therefore, a matching criteria in the $\eta - \phi$ space is applied. A reconstructed jet is associated with a truth quark if

$$\Delta R = \sqrt{(\phi_{\mathrm{reco}} - \phi_{\mathrm{truth}})^2 + (\eta_{\mathrm{reco}} - \eta_{\mathrm{truth}})^2} < 0.3$$

is fulfilled. For leptons, tighter criteria are applied. A reconstructed lepton is matched to a truth lepton if $\Delta R < 0.1$. This matching is not unique because a truth quark can be matched to more than one jet or more than two truth quarks can share the same reconstructed jet.

Matching Efficiency

The matching efficiency ϵ_{M} is defined as the probability to select the objects from the leading-order hard scattering process with the event selection described in section 6.1. Matching efficiencies for different signal samples will be presented in this section.

An event containing a top-antitop pair is called matched if a one-to-one assignment of the four truth partons to the selected jets is fulfilled. In addition, the truth lepton needs to be uniquely matched to the reconstructed lepton. A singlet or triplet signal event is labelled matched if in addition to the matching criteria in $t\bar{t}$ events, the light truth quark from the decay of the resonance is matched to exactly one of the reconstructed jets which is not associated with the truth quarks from the $t\bar{t}$ decay.

The matching efficiencies for three different singlet and triplet samples with masses of 200, 1000 and 2000 GeV are listed in Tab. 6.1 and 6.2 for different jet multiplicities. The matching efficiencies for the $t\bar{t}$ sample are shown in Tab. C.1. All jets in the events are considered for the matching.

# jets in event	Matching Efficiency $\epsilon_{\mathrm{M}}[\%]$		
	$m_{W'} = 200$ GeV	$m_{W'} = 1000$ GeV	$m_{W'} = 2000$ GeV
≥ 5	24.8 ± 1.0	24.7 ± 0.7	14.5 ± 0.6
5	19.7 ± 1.2	17.4 ± 0.9	6.5 ± 0.7
6	33.3 ± 2.4	27.1 ± 1.2	14.5 ± 1.1
7	35.9 ± 4.0	28.1 ± 1.6	17.9 ± 1.4

Table 6.1.: Matching efficiencies for the combined electron and muon channel in different W' samples with $m_{W'} = 200,\ 1000$ and 2000 GeV for different jet multiplicities.

# jets in event	Matching Efficiency $\epsilon_{\mathrm{M}}[\%]$		
	$m_{\Phi} = 200$ GeV	$m_{\Phi} = 1000$ GeV	$m_{\Phi} = 2000$ GeV
≥ 5	22.1 ± 1.7	33.0 ± 0.8	18.4 ± 0.7
5	19.5 ± 2.0	25.9 ± 1.0	11.1 ± 0.8
6	24.1 ± 3.7	36.8 ± 1.4	21.9 ± 1.4
7	38.9 ± 8.1	44.6 ± 2.1	29.6 ± 2.3

Table 6.2.: Matching efficiencies for the combined electron and muon channel in different triplet samples Φ with $m_{\Phi} = 200,\ 1000$ and 2000 GeV for different jet multiplicities.

6.3. Control Regions

Before the search for the new particle can be performed, all possible background processes have to be well understood. To validate the modelling of background processes, three different control regions are defined with low signal contamination and an enhancement of the important background processes.

1. Pretag Region: At least four jets are required in the pretag (no tag requirement) region which is used to validate W + jets and $t\bar{t}$ events.

2. A control region with more than four jets and no b-tagged is required to control the W + jets background.

3. The $t\bar{t}$ background is tested by selecting events with exactly four jets with at least one b-tagged jet.

Control plots for the event selection in the control region with exactly four jets and at least one b-tagged jet are shown in Fig. 6.1 for the muon channel and in Fig. 6.2 for the electron channel. The uncertainties on the Monte Carlo prediction include the systematic uncertainties on the background normalisation, the lepton efficiencies and the luminosity as well as the statistical uncertainty. A list of all systematic uncertainties and their determination can be found in chapter 9. A good agreement between the Monte Carlo prediction and the observation can be observed for the $t\bar{t}$ enhanced control region. The control regions for the pretag region and the enhanced W + jets background can be found in Appendix A. Although a good agreement within the uncertainties for the expected and observed number of events can be observed in the pretag region, the Monte Carlo prediction in the muon channel, see Fig. A.1 and A.2, underestimates the observation whereas a good modelling is achieved in the electron channel, see Fig. A.3 and A.4. This effect is currently studied within the ATLAS collaboration. The jet multiplicity in data does not agree very well with the predicted distribution in Monte Carlo in the muon channel especially for large jet multiplicities if the production of top quark pairs is modelled with MC@NLO. Currently the settings of different Monte Carlo generators for the production of top quarks with additional jets are compared and validated. This mismodelling of the jet multiplicity distribution leads also to the large discrepancies in the W + jets enhanced control region with at least five jets.

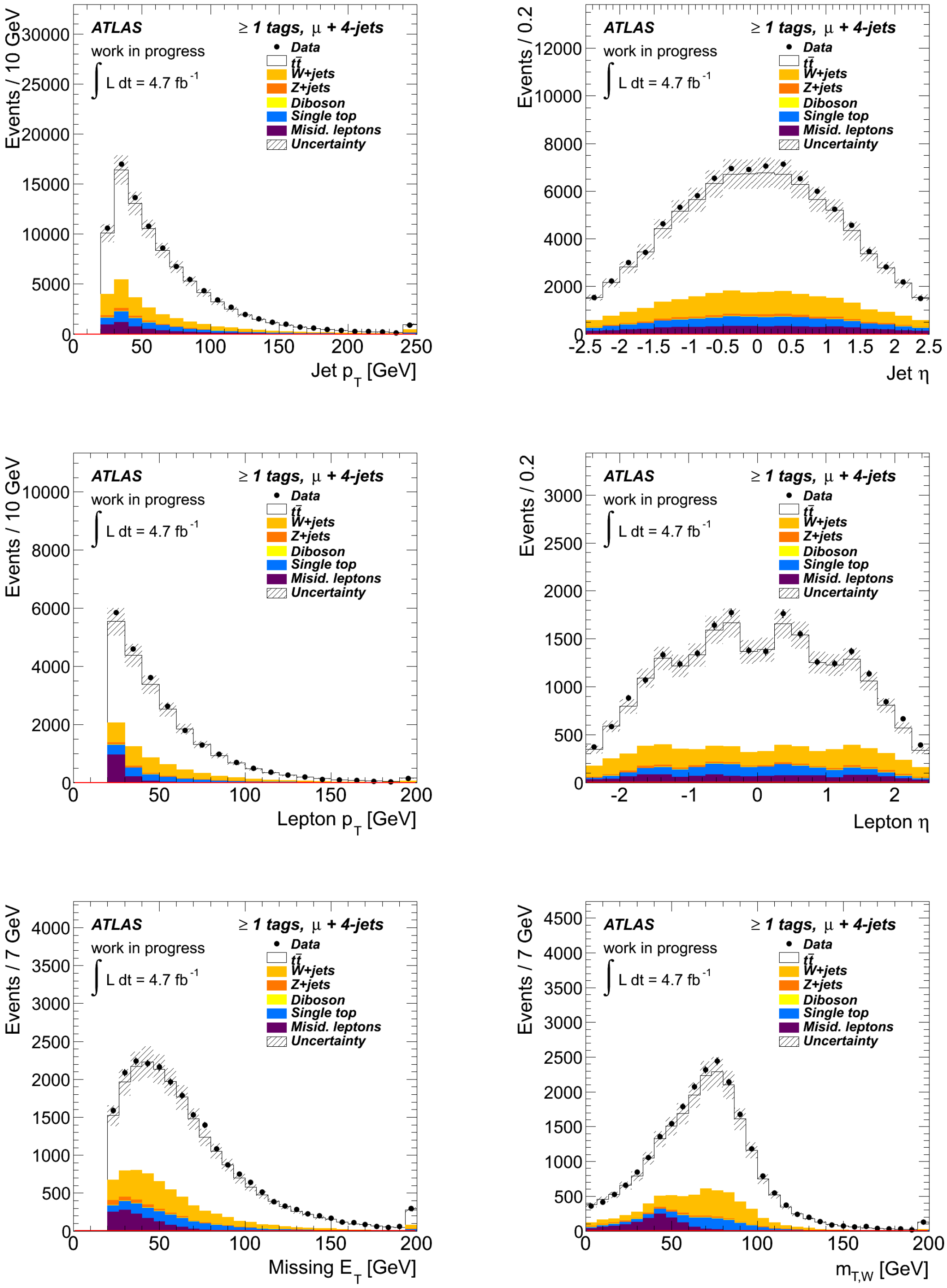

Figure 6.1.: Control plots for the μ + jets channel in the $t\bar{t}$ enhanced background region with exactly four jets and at least one b-tagged jet. The transverse momentum p_{T} and the pseudorapidity η of the jets and the muon are shown as well as the missing transverse energy distribution $E_{\mathrm{T}}^{\mathrm{miss}}$ and the transverse W-boson mass $m_{\mathrm{T}}(W)$. The uncertainties are statistical and systematic uncertainties on the normalisation of the background as well as uncertainties on the luminosity, b-tag scale factors and electron and muon efficiencies.

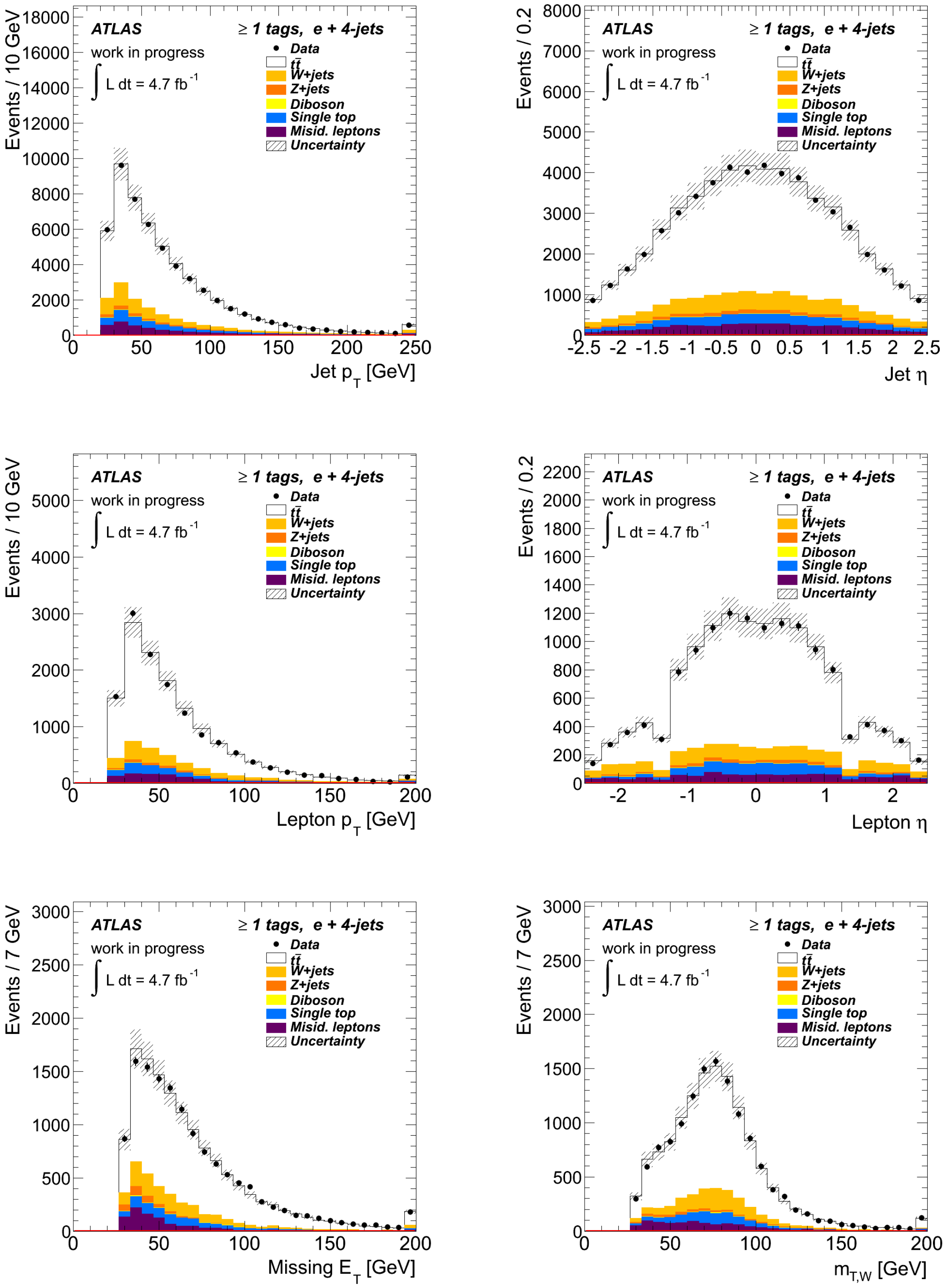

Figure 6.2.: Control plots for the e + jets channel in the $t\bar{t}$ enhanced background region with exactly four jets and at least one b-tagged jet. The transverse momentum p_{T} and the pseudorapidity η of the jets and the electron are shown as well as the missing transverse energy distribution $E_{\mathrm{T}}^{\mathrm{miss}}$ and the transverse W-boson mass $m_{\mathrm{T}}(W)$. The uncertainties on the prediction are statistical and systematic uncertainties on the normalisation of the background as well as uncertainties on the luminosity, b-tag scale factors and electron and muon efficiencies.

7. Event Reconstruction

The selected signal events in the lepton + jets channel comprise five jets at leading order. Four of those jets can be associated to the decay of the $t\bar{t}$ pair and the remaining jet to the decay of the new resonance M. The reconstruction of the top-antitop pair is done with the *Kinematic Likelihood Fitter* [66] which will be denoted in the following as KLFitter. The KLFitter is based on a likelihood approach and is explained in section 7.1. Two different techniques to choose the jet associated to the resonance decay among the remaining jets have been tested. Reconstruction efficiencies, which are defined as the probability that all jets are correctly assigned to the truth quarks, are presented in 7.2 for both techniques.

7.1. Kinematic Likelihood Fitter

The KLFitter is a general tool for kinematic fitting using a likelihood approach. The likelihood is defined as the probability to measure a certain set of quantities given a particular event topology with a certain set of parameters. In this analysis, the KLFitter is used to reconstruct the semileptonic decay of top-antitop pairs. For the kinematic fit, the energies and directions of the four jets (E_i, Ω_i), the lepton (E_l, Ω_l) and the missing transverse energy $E_{\mathrm{T}}^{\mathrm{miss}}$ are used from the measurement. The x and y-component of the missing transverse energy as well as the energies of the jets and the lepton cannot be measured precisely due to resolution effects. The directions of the jets and the lepton are assumed to be measured without uncertainty. The energy resolution of the detector is parametrized by a double gaussian transfer function $W(E_{\mathrm{true}}, E_{\mathrm{meas}})$ which is defined as the probability to measure an energy E_{meas} given the truth energy E_{true}:

$$W(E_{\mathrm{true}}, E_{\mathrm{meas}}) = \frac{1}{2\pi} \frac{1}{p_2 + p_3 \cdot p_5} \left(e^{\frac{(\Delta E - p_1)^2}{2p_2^2}} + p_3 \cdot e^{\frac{(\Delta E - p_4)^2}{2p_5^2}} \right) ,$$

with

$$\Delta E = \frac{E_{\mathrm{meas}} - E_{\mathrm{truth}}}{E_{\mathrm{truth}}} .$$

The parameters p_1, p_4 are the mean values of the first and second Gaussian, respectively and p_2, p_5 are the width of the two Gaussians. The parameter p_3 is the scale of the second Gaussian compared to the first one. The parameters p_i depend on the truth energy E_{truth} of the particle. The energy dependence of the parameters p_i depends on the type of particle and is listed in Tab. 7.1. One distinguishes between b-jets, light jets, electrons and muons. The transfer functions have been extracted from semileptonic $t\bar{t}$ samples which have been generated with MC@NLO and passed through the full ATLAS reconstruction.

parton type	p_1	p_2	p_3	p_4	p_5
b-jets	$\frac{a_1}{\sqrt{E_{\text{truth}}}} + b_1 \cdot E_{\text{truth}}$	$\frac{a_2}{\sqrt{E_{\text{truth}}}} + b_2$	$\frac{a_3}{\sqrt{E_{\text{truth}}}} + b_3 \cdot E_{\text{truth}}$	$a_4 + b_4 \cdot E_{\text{truth}}$	$a_5 + b_5 \cdot E_{\text{truth}}$
light jets	$a_1 + b_1 \cdot E_{\text{truth}}$	$\frac{a_2}{\sqrt{E_{\text{truth}}}} + b_2$	$a_3 + b_3 \cdot E_{\text{truth}}$	$a_4 + b_4 \cdot E_{\text{truth}}$	$a_5 + b_5 \cdot E_{\text{truth}}$
electrons	$a_1 + b_1 \cdot E_{\text{truth}}$	$\frac{a_2}{\sqrt{E_{\text{truth}}}} + b_2$	$a_3 + b_3 \cdot E_{\text{truth}}$	$a_4 + b_4 \cdot E_{\text{truth}}$	$a_5 + b_5 \cdot E_{\text{truth}}$
muons	$a_1 + b_1 \cdot E_{\text{truth}}$	$a_2 + b_2 \cdot E_{\text{truth}}$	$a_3 + b_3 \cdot E_{\text{truth}}$	$a_4 + b_4 \cdot E_{\text{truth}}$	$a_5 + b_5 \cdot E_{\text{truth}}$

Table 7.1.: Energy dependence of the parameters p_{i} of the transfer functions for different particle types.

For the calculation of the likelihood, the invariant dijet mass m_{jj} and the invariant mass of the lepton and neutrino $m_{l\nu}$ are assumed to be Breit-Wigner (BW) distributed around the pole W-mass $m_W = 80.4$ GeV within a width of $\Gamma = 2.1$ GeV. Moreover the invariant mass of one b-jet and the two light jets m_{jjj} has to be Breit-Wigner distributed around the top-pole mass of $m_t = 172.5$ GeV within a width of $\Gamma = 1.5$ GeV and analogue for the invariant mass of the b-jet, lepton and the corresponding neutrino $m_{l\nu j}$. The top quark mass can be either used as an additional free parameter in the kinematic fit or be fixed.

The likelihood for the lepton + jets channel in $t\bar{t}$ events is defined as:

$$\mathcal{L} = BW(m_{jjj}, m_t) \cdot BW(m_{l\nu j}, m_t) \cdot BW(m_{jj}, m_W) \cdot BW(m_{l\nu}, m_W) \cdot \\ \left(\prod_{i=1}^{4} W(\tilde{E}_i, E_i)\right) \cdot W(E_x^{miss}, p_x^{nu}) \cdot W(E_y^{miss}, p_y^{nu}) \cdot \begin{cases} W(\tilde{E}_l, E_l) \ , & \text{electron channel} \\ W(\tilde{p}_{\text{T},l}, p_{\text{T},l}) \ , & \text{muon channel} \end{cases}$$

As indicated in chapter 6.1, events with at least five jets are selected. In order to choose the four jets from the $t\bar{t}$ decay out of the n selected jets, $\frac{n!}{(n-4)!4!}$ combinations exist. For each combination, 24 possible permutations exist to assign the four jets to the two light quarks from the hadronically decaying W-boson and the two b-quarks. Since the likelihood is symmetric under the permutation of the two light quarks, only 12 permutations remain. Due to the large number of possible permutations, only events with less than 10 jets are used for the analysis. The likelihood is calculated for each permutation and the permutation with the largest likelihood value is chosen for the event reconstruction. Instead of maximizing the likelihood function, the minimum of $-\log \mathcal{L}$ is calculated with respect to the parameters. For the minimization, the KLFitter is interfaced to the Bayesian Analysis Toolkit (BAT) [67] which uses amongst other MINUIT as minimization technique.

The KLFitter returns the best fit parameters, the likelihood value as well as a relative weight for each permutation which contains also the b-tagging weight if the weighting method is chosen which will be explained in the following.

b-tagging in KLFitter

B-tagging can be used in the KLFitter to improve the reconstruction efficiency. Two different methods can be chosen:

1. a veto method (kVeto),

2. a weighting method.

In the first method, permutations with b-tagged jets on the position of the light quarks of the hadronically decaying W-boson are vetoed. These events have an event probability of zero. The weighting method is applied to a certain working point and takes the tagging efficiencies of b-quarks and the rejection of light quarks into account. The event probability for each event is multiplied by the following factor:

$$\left\{\begin{array}{cl} \epsilon & , b_{had} \text{ tagged} \\ (1-\epsilon), & b_{had} \text{ not tagged} \end{array}\right\} \cdot \left\{\begin{array}{cl} \epsilon & , b_{lep} \text{ tagged} \\ (1-\epsilon), & b_{lep} \text{ not tagged} \end{array}\right\} \cdot$$

$$\left\{\begin{array}{cl} \frac{1}{R} & , \text{ light quark 1 tagged} \\ (1-\frac{1}{R}), & \text{light quark 1 not tagged} \end{array}\right\} \cdot \left\{\begin{array}{cl} \frac{1}{R} & , \text{ light quark 2 tagged} \\ (1-\frac{1}{R}), & \text{light quark 2 not tagged} \end{array}\right\}$$

If b-tagging is used in the kinematic fit, for each jet, the information if the jet was tagged, needs to be provided for the veto and weighting method. Furthermore, the tagging efficiency for b-jets and rejection for light jets is needed in the weighting method.

7.2. Resonance Reconstruction

For the reconstruction of the new particle, the assignment of the reconstructed jets to the four truth partons of the $t\bar{t}$ decay is used. The light flavour jet associated to the decay of the new particle is chosen among the remaining jets which are not assigned to the $t\bar{t}$ decay. Two different approaches have been tested to identify the light flavour jet. In a first approach, the jet with the highest transverse momentum is selected as the jet from the resonance decay. This approach will be denoted as the p_T *method* in the following. In a second approach, each remaining jet is combined with the top and antitop quark, respectively and the invariant masses m_{tj}, $m_{\bar{\mathrm{t}}\mathrm{j}}$ are calculated. The jet which gives the largest invariant tj and $\bar{t}j$ mass is chosen. The masses m_{tj} and $m_{\bar{\mathrm{t}}\mathrm{j}}$ are maximized separately which might result in two different jets for the reconstruction of the resonance. In the following, this approach will be denoted as the $m_{\mathrm{tj}}/m_{\bar{\mathrm{t}}\mathrm{j}}$ *mass method.* Both techniques for the reconstruction of the new resonance are compared and reconstruction efficiencies are evaluated in chapter 7.2.1.

7.2.1. Reconstruction Efficiencies

The reconstruction efficiency ϵ_{R} is defined as the probability to find the correct jet-parton association. As the correct permutation can only be selected for matched events, the reconstruction efficiency can be defined as the ratio of the number of events in which all jets are correctly assigned to the total number of matched events.
For the analysis, the number of jets which is passed to the KLFitter for the reconstruction of the $t\bar{t}$ pair will be limited to reduce the number of permutations per event. The more jets are taken into account, the more permutations exist which results in an decrease of the reconstruction efficiency. If the number of jets in the event is n, then $\binom{n}{4}$ permutations exist to choose the four jets from the $t\bar{t}$ decay. For each permutation, 4! possibilities to assign the jets to the truth partons need to be taken into account. Therefore, the total number of permutations in an event with n jets is given by:

$$N_{\mathrm{perm}} = \frac{n!}{2 \cdot (n-4)!} \; .$$

If not all selected jets are taken into account for the reconstruction of the resonance, the matching efficiencies (see chapter 6.2) need to be re-evaluated. The matching efficiencies for the three different singlet and triplet samples with masses of 200, 1000 and 2000 GeV are listed in Tab. 7.2 and 7.3 for different jet multiplicities depending on the number of jets used for the matching. If the number of jets for the matching is limited to n_{j}, only n_{j} jets with the highest p_{T} are considered. The matching efficiencies for the five jet inclusive bin for the different samples are summarized in the first row. If the number of jets in the event is smaller than the number of jets which are considered for the matching, all available jets are used for the matching. In addition, the matching efficiencies for the $t\bar{t}$ samples are given in Tab. C.2. As expected, the more jets are taken into account for the matching, the higher the matching efficiency.

Number of jets in event	Number of jets considered for fit	Matching Efficiency [%]		
		$m_{W'} = 200$ GeV	$m_{W'} = 1000$ GeV	$m_{W'} = 2000$ GeV
≥ 5	5	14.2 ± 0.8	11.5 ± 0.5	4.2 ± 0.3
	6	22.2 ± 1.0	19.1 ± 0.6	8.7 ± 0.5
	7	24.3 ± 1.0	23.1 ± 0.6	11.9 ± 0.5
5	5	19.7 ± 1.2	17.4 ± 0.9	6.5 ± 0.7
6	5	4.5 ± 1.0	10.3 ± 0.8	4.9 ± 0.7
	6	33.3 ± 2.4	27.1 ± 1.2	14.5 ± 1.1
7	5	3.4 ± 1.5	6.2 ± 0.9	3.5 ± 0.7
	6	15.2 ± 3.0	14.8 ± 1.3	9.6 ± 1.0
	7	35.7 ± 4.0	28.1 ± 1.6	17.9 ± 1.4

Table 7.2.: Matching efficiency for three different W' samples with masses of 200, 1000 and 2000 GeV for a given number of jets in the event and in dependence on the number of jets which are considered for the matching.

Number of jets in event	Number of jets considered for fit	Matching Efficiency [%]		
		$m_\Phi = 200$ GeV	$m_\Phi = 1000$ GeV	$m_\Phi = 2000$ GeV
≥ 5	5	15.0 ± 1.5	18.4 ± 0.6	8.5 ± 0.5
	6	20.3 ± 1.7	28.3 ± 0.7	14.9 ± 0.7
	7	21.8 ± 1.7	31.8 ± 0.8	17.3 ± 0.7
5	5	19.5 ± 2.0	25.9 ± 1.1	11.1 ± 0.9
6	5	6.8 ± 2.2	15.3 ± 1.1	8.5 ± 1.0
	6	24.0 ± 3.4	36.8 ± 1.4	21.9 ± 1.4
7	5	0.0 ± 0.0	9.6 ± 1.2	4.7 ± 1.1
	6	19.4 ± 6.6	26.6 ± 1.9	16.9 ± 1.9
	7	38.9 ± 8.1	44.6 ± 2.1	29.6 ± 2.3

Table 7.3.: Matching efficiency for three different triplet samples with masses of 200, 1000 and 2000 GeV for a given number of jets in the event and in dependence on the number of jets which are considered for the matching.

Comparison of the Reconstruction Methods

The correct reconstruction of the selected objects to the decay topology of the new particle is very important for the analysis. Therefore, the reconstruction efficiency of the KLFitter is calculated for different signal samples and the $t\bar{t}$ sample. Furthermore, the two reconstruction techniques, described in chapter 7.2 are compared. The reconstruction efficiencies for the singlet and triplet samples with masses of 200 and 1000 GeV for both reconstruction methods can be found in Appendix B. The reconstruction efficiencies for the $t\bar{t}$ sample are summarized in Tab. C.3. In this chapter, the reconstruction methods are compared for the singlet and triplet sample with a mass of $m = 2000$ GeV in Tab. 7.4.

Number of jets in event	Number of jets considered for fit	Reconstruction Efficiency ϵ_R [%]			
		$m_{W'} = 2000$ GeV		$m_\Phi = 2000$ GeV	
		p_T method	$m_{\mathrm{tj}}/m_{\bar{\mathrm{t}}\mathrm{j}}$ mass	p_T method	$m_{\mathrm{tj}}/m_{\bar{\mathrm{t}}\mathrm{j}}$ mass
≥ 5	5	34.4 ± 3.8	34.4 ± 3.8	40.7 ± 3.2	40.7 ± 3.2
	6	30.4 ± 2.5	29.8 ± 2.5	33.4 ± 2.3	31.8 ± 2.3
	7	26.4 ± 2.1	24.9 ± 2.0	32.5 ± 2.1	31.0 ± 2.1
5	5	29.6 ± 5.4	29.6 ± 5.4	38.9 ± 4.0	38.9 ± 4.0
6	5	38.3 ± 7.1	38.3 ± 7.1	45.8 ± 5.9	45.8 ± 5.9
	6	30.7 ± 3.9	30.0 ± 3.9	33.8 ± 3.5	31.7 ± 3.4
7	5	42.9 ± 9.4	42.9 ± 9.4	31.6 ± 10.7	31.6 ± 10.7
	6	27.6 ± 5.1	26.3 ± 5.1	25.0 ± 5.3	22.1 ± 5.0
	7	22.5 ± 3.5	21.8 ± 3.5	22.7 ± 3.8	21.8 ± 3.8

Table 7.4.: Reconstruction efficiencies for the singlet and triplet samples with $m = 2000$ GeV for a given number of jets in the event and in dependence on the number of jets which are considered for the fit. The reconstruction efficiencies are evaluated for the two different reconstruction methods.

The reconstruction efficiency decreases if more jets are taken into account due to the larger number of permutations. An event which is reconstructed with the $m_{\mathrm{tj}}/m_{\bar{\mathrm{t}}\mathrm{j}}$ mass method can only be correctly reconstructed if the jets which gives the largest tj and $\bar{t}j$ invariant mass are the same. Therefore, the reconstruction efficiencies using the highest p_{T} jet for the resonance reconstruction is higher. For the signal samples with a high mass of 2000 GeV, the reconstruction efficiencies for both methods are very similar. The difference between ϵ_R for the two reconstruction methods is larger for the signal samples with a smaller mass, see Tab B.1 and B.2. This can be explained by the four different possibilities which exist if comparing the two reconstruction methods.

1. The same jet gives the largest tj and $\bar{t}j$ invariant mass and is also the highest remaining p_{T} jet.
2. The two jets which give the largest tj and $\bar{t}j$ invariant mass are the same but not the highest remaining p_{T} jet.
3. Different jets are used for the reconstruction of m_{tj} and $m_{\bar{\mathrm{t}}\mathrm{j}}$ and one jet is the highest remaining p_{T} jet.
4. All jets differ.

For the three different singlet and triplet samples, the percentage with which each of the cases described above occurs, is given in Tab. 7.5. Only events containing more than five jets have been taken into account and the highest seven jets in p_{T} have been considered for the fit.

Sample	Mass [GeV]	case 1 [%]	case 2 [%]	case 3 [%]	case 4 [%]
Singlet	200	55.71	14.11	27.77	2.32
	1000	73.32	6.30	19.66	0.69
	2000	70.93	7.55	20.90	0.62
Triplet	200	61.79	12.74	23.85	1.36
	1000	75.03	5.47	18.91	0.60
	2000	78.87	3.88	17.16	0.09

Table 7.5.: Comparison of the reconstruction methods for different singlet and triplet samples.

The smaller the mass of the resonance, the higher the probability that the jets for the reconstruction of the tj and $\bar{t}j$ mass differ (case 3 and 4). In addition, the probability for case 1 decreases for small resonance masses. Therefore, the difference between the two reconstruction methods becomes larger for smaller resonance masses.

KLFitter Performance

To evaluate the performance of the KLFitter, the reconstruction efficiencies are compared to the statistical probabilities. Fig. 7.1 shows the reconstruction efficiencies of the KLFitter for the three different singlet (a) and triplet (b) samples as well as the statistical probabilities for random assignments of the jets to the decay topology. In these plots, the p_{T} reconstruction method has been used and the highest six p_{T} jets have been taken into account for the reconstruction. The efficiency of the KLFitter to assign all jets correctly to the decay of the resonance for the singlet sample with a mass of $m_{W'} = 2000$ GeV is 30.6% compared to 0.28% if the jets are randomly assigned.

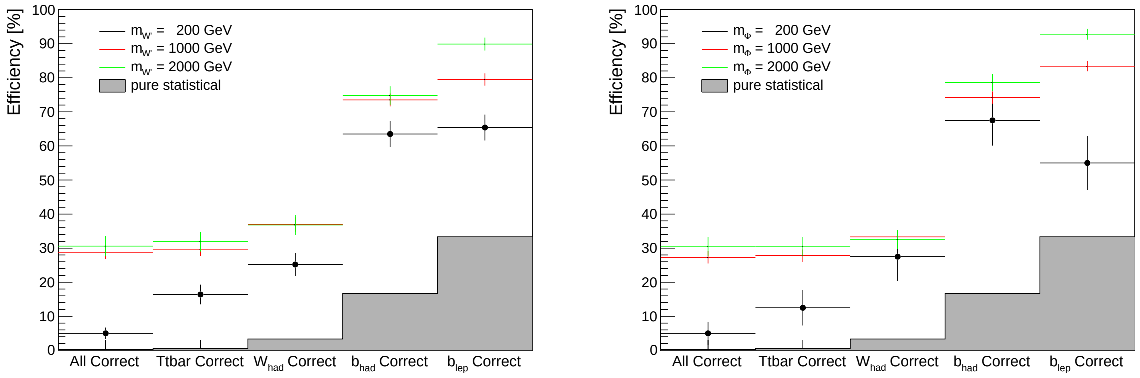

(a) singlet

(b) triplet

Figure 7.1.: Comparison of the KLFitter reconstruction efficiencies to the statistical probabilities for the singlet (a) and triplet (b) samples with a mass of 200, 1000 and 2000 GeV. The efficiencies for finding the correct resonance reconstruction, the correct assignment of the jets to the $t\bar{t}$ decay topology, the correct quarks of the hadronic W decay, the b-quark from the hadronic top quark decay as well as the b-quark from the leptonic top quark decay.

Total Efficiencies

Although the reconstruction efficiency is the quantity which should be maximized in the analysis, ϵ_{R} is not used to quantify the performance of the KLFitter. If more jets are considered in the fit, the matching efficiency increases. Due to the larger number of matched events, the number of correctly reconstructed events might also increase although the reconstruction efficiency decreases. Therefore, the performance of the KLFitter is quantified by the total efficiency ϵ_{tot}:

$$\epsilon_{\mathrm{tot}} = \epsilon_{\mathrm{M}} \cdot \epsilon_{\mathrm{R}} \ .$$

The total efficiencies for the different singlet and triplet samples can be found in Tab. 7.6 and 7.7 using the p_{T} method for the reconstruction. The total efficiencies for the $m_{\mathrm{tj}}/m_{\bar{\mathrm{t}}\mathrm{j}}$ method can be found in Tab. B.3 and B.4.

Number of jets in event	Number of jets considered for fit	Total Efficiency ϵ_{tot} [%]		
		$m_{W'} = 200$ GeV	$m_{W'} = 1000$ GeV	$m_{W'} = 2000$ GeV
≥ 5	5	3.4 ± 0.4	4.6 ± 0.3	1.4 ± 0.2
	6	3.5 ± 0.4	6.2 ± 0.4	2.7 ± 0.3
	7	3.5 ± 0.4	6.5 ± 0.4	3.2 ± 0.3
5	5	4.6 ± 0.6	6.8 ± 0.6	1.9 ± 0.4
6	5	1.3 ± 0.6	4.5 ± 0.6	1.9 ± 0.4
	6	1.5 ± 0.6	7.9 ± 0.8	4.5 ± 0.7
7	5	1.4 ± 1.0	2.3 ± 0.5	1.5 ± 0.4
	6	1.4 ± 1.0	4.2 ± 0.7	2.6 ± 0.6
	7	2.1 ± 1.2	5.0 ± 0.8	4.0 ± 0.7

Table 7.6.: Total efficiencies for different W' samples using the p_{T} mass method for the reconstruction of the resonance.

Number of jets in event	Number of jets considered for fit	Total Efficiency ϵ_{tot} [%]		
		$m_{\Phi} = 200$ GeV	$m_{\Phi} = 1000$ GeV	$m_{\Phi} = 2000$ GeV
≥ 5	5	3.4 ± 0.8	7.2 ± 0.4	3.5 ± 0.3
	6	3.7 ± 0.8	9.0 ± 0.5	5.0 ± 0.4
	7	3.7 ± 0.8	9.6 ± 0.5	5.6 ± 0.4
5	5	4.9 ± 1.1	9.8 ± 0.7	4.3 ± 0.6
6	5	0.0 ± 0.0	6.0 ± 0.7	3.9 ± 0.7
	6	1.5 ± 1.1	9.7 ± 0.9	7.4 ± 0.9
7	5	0.0 ± 0.0	4.3 ± 0.9	1.5 ± 0.6
	6	0.0 ± 0.0	7.9 ± 1.1	4.2 ± 1.0
	7	0.0 ± 0.0	11.4 ± 1.3	6.7 ± 1.2

Table 7.7.: Total efficiencies for different triplet samples using the p_{T} mass method for the reconstruction of the resonance.

In general, the total efficiency increases the more jets are taken into account for the fit. If seven jets are considered in the fit, the total efficiency does not gain significantly compared to the efficiencies if only six jets are used. On the other hand, the reconstruction efficiencies for the high mass singlet samples, see Tab. 7.4 and Tab. B.1 drops significantly if seven instead of six jets are used for the reconstruction. Furthermore, it has been checked if the signal over background ratio increases if more jets are considered. No significant improvement of $S/\sqrt{B}$ have been observed. Therefore, only the highest six p_{T} jets are used for the reconstruction in the following analysis. Besides, the p_{T} method is chosen for the reconstruction of the resonance as it has higher reconstruction efficiencies than the $m_{\mathrm{tj}}/m_{\bar{\mathrm{t}}\mathrm{j}}$ mass method.

Reconstruction with/without b-tagging

Besides the number of jets which are taken into account for the fit, the impact of the different b-tagging methods on the reconstruction efficiencies has been investigated. The reconstruction efficiencies for the 2000 GeV singlet and triplet sample if no b-tagging information is used as well as for the kVeto and the weighting method are listed in Tab. 7.8 and Tab. 7.9. For informations about the different methods, see chapter 7.1. As expected, the reconstruction efficiency increases if b-tagging information is used. Further improvement can be achieved if the weighting method is chosen which takes the tagging efficiencies into account.

Number of jets in event	Number of jets considered for fit	Reconstruction Efficiency [%]		
		weighting method	kVeto	no b-tagging
≥ 5	5	34.4 ± 3.8	32.5 ± 3.7	29.9 ± 3.7
	6	30.4 ± 2.5	26.1 ± 2.4	25.2 ± 2.4
	7	26.4 ± 2.1	23.1 ± 2.0	20.9 ± 1.9
5	5	29.6 ± 5.4	29.6 ± 5.4	22.5 ± 5.0
6	5	38.3 ± 7.1	38.3 ± 7.1	34.0 ± 6.9
	6	30.7 ± 3.9	25.0 ± 3.7	25.7 ± 3.7
7	5	42.9 ± 9.4	32.1 ± 8.8	42.9 ± 9.4
	6	27.6 ± 5.1	23.7 ± 4.9	21.1 ± 4.7
	7	22.5 ± 3.5	20.4 ± 3.4	16.9 ± 3.1

Table 7.8.: Reconstruction efficiencies for the singlet sample with $m_{W'} = 2000$ GeV using no b-tag information, the kVeto method and the weighting method.

Number of jets in event	Number of jets considered for fit	Reconstruction Efficiency [%]		
		weighting method	kVeto	no b-tagging
≥ 5	5	40.7 ± 3.2	36.6 ± 3.1	29.2 ± 2.9
	6	33.4 ± 2.3	28.7 ± 2.2	23.3 ± 2.0
	7	32.5 ± 2.1	27.8 ± 2.0	23.3 ± 1.9
5	5	38.9 ± 4.0	35.8 ± 3.9	27.5 ± 3.7
6	5	45.8 ± 5.9	40.3 ± 5.8	31.9 ± 5.5
	6	33.9 ± 3.5	26.9 ± 3.3	23.1 ± 3.1
7	5	31.6 ± 10.7	26.3 ± 10.1	26.3 ± 10.1
	6	25.0 ± 5.3	22.6 ± 5.0	19.1 ± 4.8
	7	22.7 ± 3.8	18.5 ± 3.6	16.8 ± 3.4

Table 7.9.: Reconstruction efficiencies for the triplet sample with $m_\Phi = 2000$ GeV using no b-tag information, the kVeto method and the weighting method.

7.3. Kinematic Distributions

Control plots for the reconstruction of the $t\bar{t}$ pair with the KLFitter as well as the resonance are shown in Fig. 7.2 for the muon and electron channel in the $t\bar{t}$ enhanced control region, respectively. Shown are the log Likelihood, the invariant mass of the $t\bar{t}$ pair $m_{t\bar{t}}$ and its transverse momentum $p_{\mathrm{T}}(t\bar{t})$. Further distributions for the pretag control region can be found in Fig. A.2 and Fig. A.4 and for the W + jets enhanced region in Fig. A.6 and Fig. A.8 in

Appendix A. For all control regions, the predictions agree within their uncertainties with the observations.

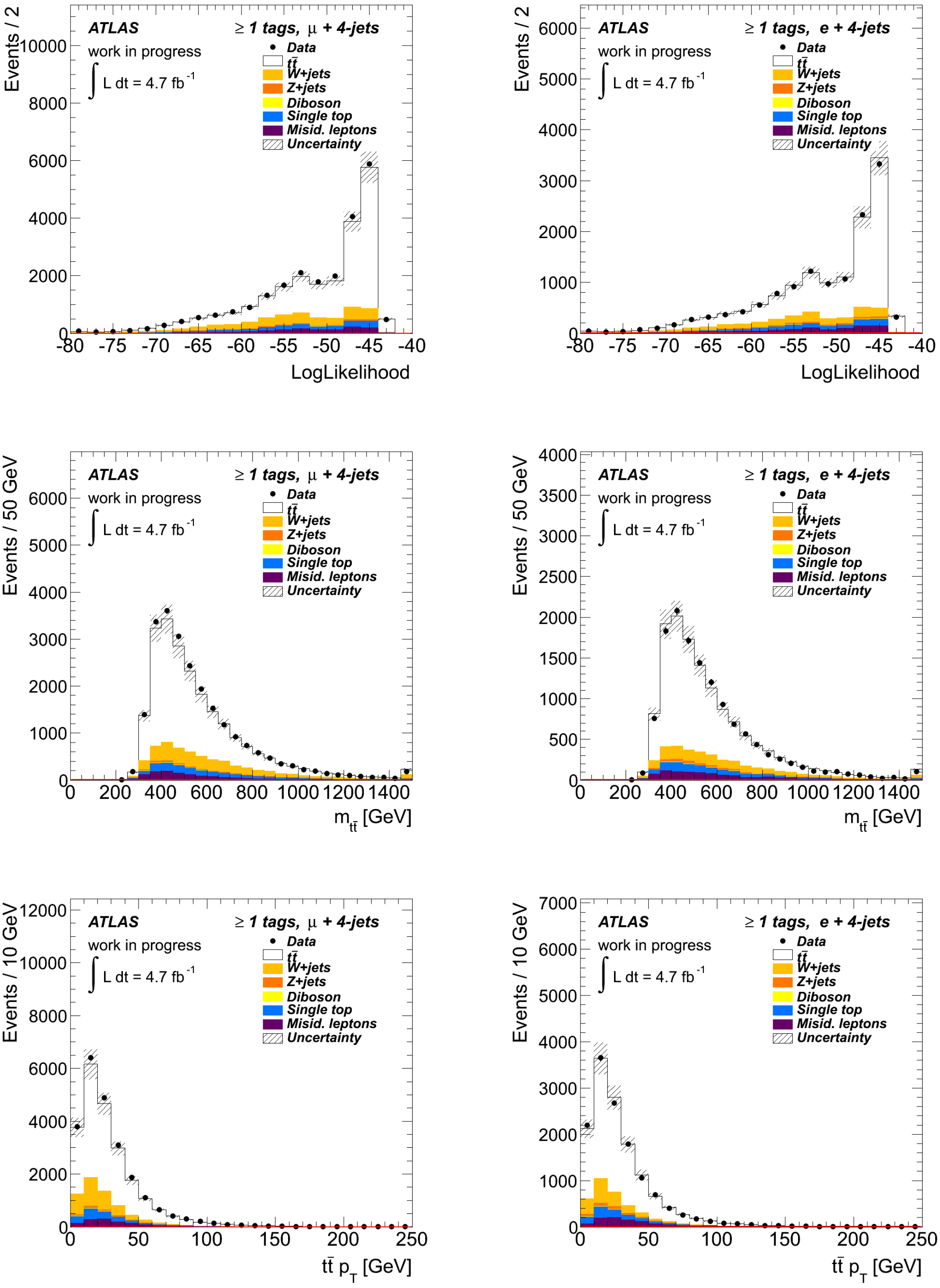

Figure 7.2.: Control plots for the μ + jets (left) and e + jets (right) channel in the $t\bar{t}$ enhanced region. Shown are the log Likelihood, the invariant mass of the $t\bar{t}$ pair and its transverse momentum. Only the statistical uncertainties are indicated.

8. Analysis Strategy

Due to the small cross sections of the production of a new singlet or triplet particle, the analysis needs to be optimised to enhance the signal over the background. Several optimisation studies have been performed for the analysis [68] which are shortly summarised in chapter 8.1. The analysis presented in [68] is a cut-and-count analysis and hence does not use shape information. In order to select a sample of events with a high signal-over-background ratio, a cut in the $m_{tj} - m_{\bar{t}j}$ plane is applied which is described in chapter 8.2.

8.1. Optimisation Studies

In the following, the optimisations which have been studied to improve the sensitivity of the analysis are introduced. As a figure of merit, the scale factor s95 has been used which is the scale factor on which the signal is excluded at 95%. The new physics process can be excluded for s95 = 1. Hence, the smaller s95, the better the sensitivity.

The likelihood distributions for the singlet sample with $m_{W'} = 400$ GeV and the $t\bar{t}$ background sample in the signal region (at least five jets and at least one b-tag) are shown in Fig. 8.1. It has been tested if a cut on the log likelihood distribution at $\log(L) = -52$ improves the sensitivity of the analysis. Although a large number of $t\bar{t}$ events is thrown away, no gain in sensitivity can be achieved if a likelihood cut is applied.

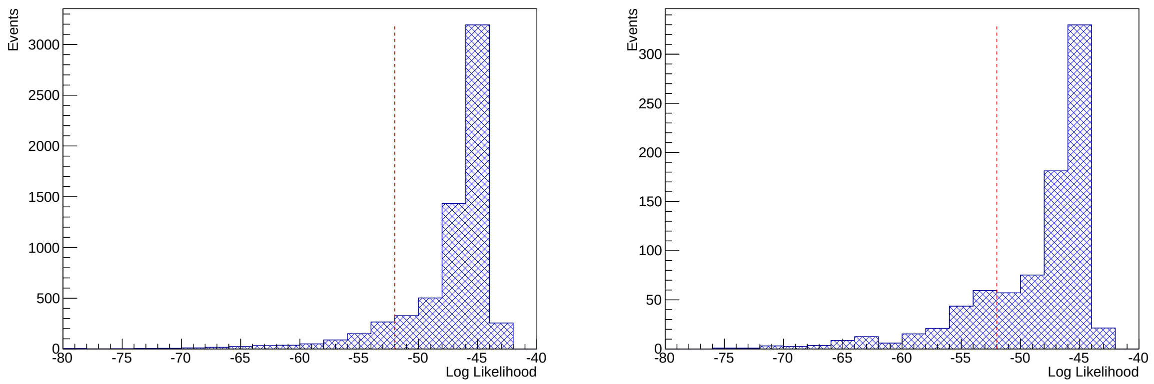

(a) $t\bar{t}$

(b) $m_{W'} = 400$ GeV

Figure 8.1.: Log likelihood distributions in the signal region for the $t\bar{t}$ sample and the singlet sample with $m_{W'} = 400$ GeV. The red line indicates the likelihood cut value.

Furthermore, it has been tested whether b-tagging information should be used in the KLFitter and which method (kVeto or weighting method) should be chosen. Using b-tagging information in the KLFitter does not change the sensitivity. Therefore, the weighting method is chosen as it gives the largest reconstruction efficiency.
The sensitivity is increased if only the assignment of the jets to the partons by the KLFitter is used and not the fitted values. The larger the mass of the resonance, the larger the discrepancy between the scale factor s95 if fitted or the reconstructed values are used.
In the event selection, the leading jet is required to have a transverse momentum of at least 25 GeV. Three different cuts on the leading jet p_{T} , i.e. $p_{\mathrm{T}} > 60$, 80 and 100 GeV, have been tested. No gain in sensitivity was observed and the standard p_{T} cut is kept for the analysis.

8.2. 2d-Binning Method

To enhance the signal over background ratio and hence to increase the sensitivity, a two dimensional binning optimisation in the $m_{tj} - m_{\bar{t}j}$ plane has been performed. For each singlet and triplet sample, two dimensional histograms (m_{tj} vs. $m_{\bar{t}j}$) are filled using bin sizes of 25 GeV. Different bin sizes for the optimisation have been studied, yielding no further improvements. To choose the $m_{tj} - m_{\bar{t}j}$ phase space which is most sensitive for the signal sample under study, a scan over the two-dimensional histogram is performed varying the upper and lower bin edges of m_{tj} and $m_{\bar{t}j}$, respectively. The bin edges for different singlet and triplet samples which give the largest sensitivity are listed in Tab. 8.1 and 8.2. For the optimisation studies, the full list of systematic uncertainties, described in chapter 9, have been taken into account.

Resonance	200 GeV	300 GeV	400 GeV	500 GeV	600 GeV	700 GeV	800 GeV
m_{tj} lower bound	250 GeV	350 GeV	400 GeV	550 GeV	550 GeV	675 GeV	675 GeV
m_{tj} upper bound	300 GeV	450 GeV	825 GeV	775 GeV	750 GeV	1125 GeV	1150 GeV
$m_{\bar{t}j}$ lower bound	225 GeV	275 GeV	375 GeV	450 GeV	550 GeV	675 GeV	700 GeV
$m_{\bar{t}j}$ upper bound	250 GeV	350 GeV	425 GeV	525 GeV	650 GeV	750 GeV	875 GeV

Table 8.1.: Upper and lower bin edges for different singlet samples using the 2d optimisation.

Resonance	200 GeV	300 GeV	400 GeV	500 GeV	600 GeV	700 GeV	800 GeV
m_{tj} lower bound	225 GeV	300 GeV	400 GeV	500 GeV	575 GeV	700 GeV	750 GeV
m_{tj} upper bound	325 GeV	325 GeV	425 GeV	525 GeV	650 GeV	775 GeV	800 GeV
$m_{\bar{t}j}$ lower bound	250 GeV	350 GeV	375 GeV	400 GeV	475 GeV	450 GeV	750 GeV
$m_{\bar{t}j}$ upper bound	350 GeV	525 GeV	575 GeV	875 GeV	875 GeV	750 GeV	950 GeV

Table 8.2.: Upper and lower bin edges for different triplet samples using the 2d optimisation.

In order not to tune the bin optimisation to statistical fluctuations, the bin edges of the m_{tj} and

$m_{\bar{t}j}$ windows are smoothed using a linear approach. A linear dependence of the bin edges on the resonance mass is assumed. The upper and lower bin edges for m_{tj} and $m_{\bar{t}j}$ for the singlet samples are depicted in Fig. 8.2 a,b and for the triplet samples in Fig. 8.2 c,d. Furthermore, the linear fits are shown. The shaded area between the linear curves for the upper and lower limit indicates the m_{tj} and $m_{\bar{t}j}$ mass windows considered for each mass point. As it can be seen in Fig. 8.2, the $m_{\bar{t}j}$ window for the singlet sample is much smaller than the m_{tj} window, taking into account that the resonance is expected to occur predominantly in the $\bar{t}j$-system.

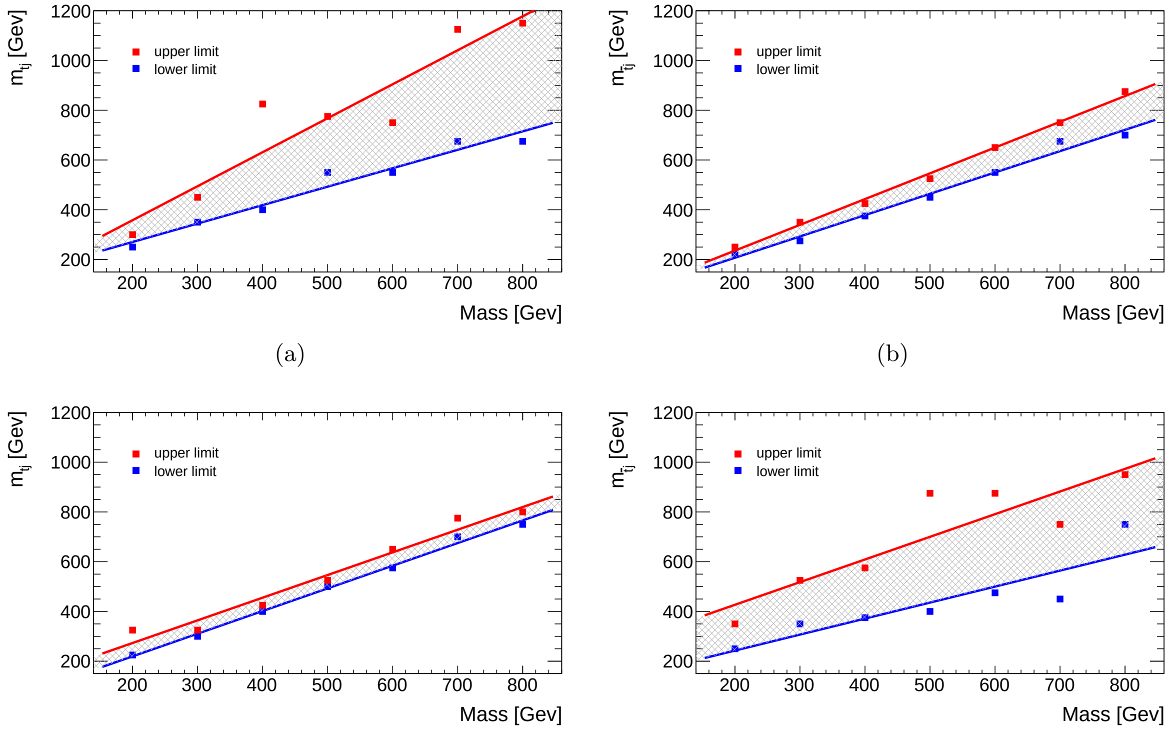

(a) (b)

(c) (d)

Figure 8.2.: Upper and lower bin edges for the m_{tj} (left) and $m_{\bar{t}j}$ (right) mass windows for the singlet (a,b) and triplet (c,d) samples. Furthermore, the linear fits used for the smoothing of the bin edges is shown. The shaded area between the fits for the upper and lower limit indicates the m_{tj} and $m_{\bar{t}j}$ mass windows considered for each mass point.

For the analysis, the bin edges, defined by the linear fits are used. For signal samples with masses larger than 800 GeV, the upper limit on m_{tj} and $m_{\bar{t}j}$ are set to 2500 GeV. Only events which fulfil the cuts, defined through the upper and lower bin edges are selected in the analysis, resulting in a single bin counting experiment.

Exemplary, the two dimensional histograms for the singlet sample with a mass of 400 GeV as well as the histogram for the largest background are shown in Fig. 8.3 a,b. The histograms are overlaid with the $m_{tj} - m_{\bar{t}j}$ mass window for the $m_{W'} = 400$ GeV singlet sample, indicated by the dashed box. Furthermore, the histogram for the triplet sample with a mass of 400 GeV and the $t\bar{t}$ sample are depicted in Fig. 8.3 c,d overlaid with the optimised mass window.

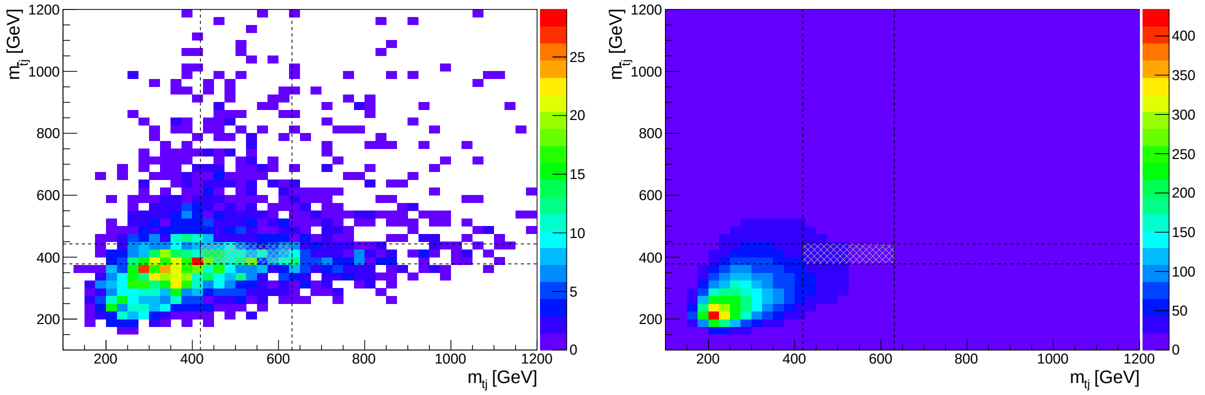

(a) Singlet $m_{W'} = 400\ GeV$ (b) $t\bar{t}$ (singlet)

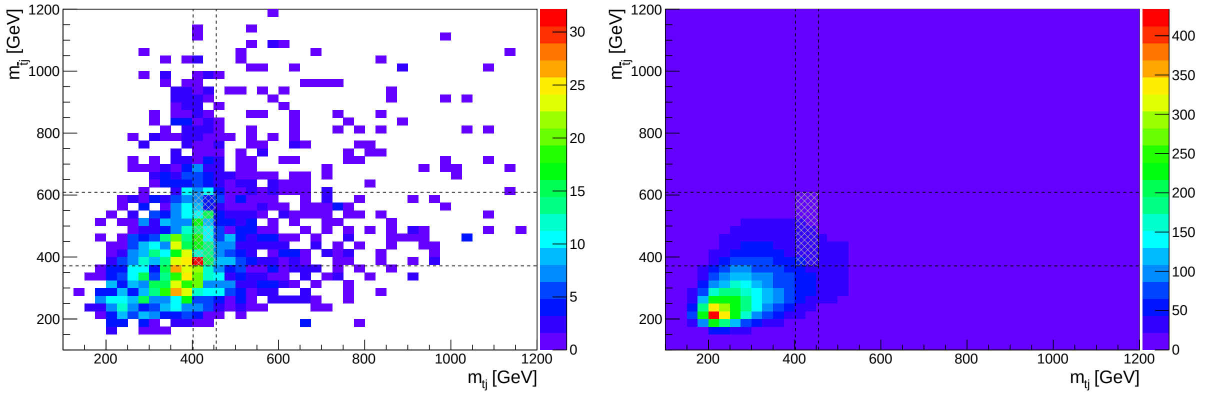

(c) Triplet $m_{\Phi} = 400\ GeV$ (d) $t\bar{t}$ (triplet)

Figure 8.3.: $m_{tj} - m_{\bar{t}j}$ histograms for the 400 GeV singlet (a) and triplet (c) sample overlaid with the optimised mass windows. The histograms for the $t\bar{t}$ sample are overlaid with the mass window optimised for the 400 GeV singlet (b) and triplet (d) sample.

9. Systematic Uncertainties

Due to the large amount of data recorded by the Large Hadron Collider per year, the evaluation of the systematic uncertainties is crucial for each analysis since the statistical uncertainty decreases with increasing statistics. In this chapter, the systematic uncertainties arising from the modelling of the signal and background processes are presented as well as uncertainties due to the modelling of the detector. Furthermore, the uncertainty of 1.8% on the integrated luminosity for the full 2011 data set is taken into account. The evaluation of the systematic uncertainties follows the prescription in [69]. In the following, only the systematic uncertainties which are included in the limit setting procedure, described in chapter 10, are introduced. For the analysis presented in [68], all systematic uncertainties have been taken into account.

9.1. Signal and Background Uncertainties

- **Monte Carlo generator:** The uncertainty due to the modelling of $t\bar{t}$ events using different Monte Carlo generators is studied comparing the default generator MC@NLO with Powheg [70] using Herwig/Jimmy for the showering. The systematic uncertainty is estimated as the relative difference between the two samples.
- **Parton shower model:** In the default $t\bar{t}$ sample, MC@NLO is interfaced with Herwig/Jimmy for the showering. In order to account for uncertainties due to the shower modelling, the results obtained with two different Powheg samples, once interfaced with Pythia and once with Herwig are compared.
- **Initial and final state radiation:** The impact of initial and final state radiation (ISR/FSR) on the measurement is studied by varying the amount of radiation. For the $t\bar{t}$ sample, two different samples are simulated with AcerMC interfaced with Pythia for the showering with "more" and "less" radiation. Half the difference between the two samples is taken as uncertainty. For the signal samples, private fully reconstructed samples with varied radiation are used. For the singlet and triplet samples with a mass of 800 GeV as well as for the 500 GeV triplet sample, the systematic uncertainty is examined and the largest variation is taken for all signal samples.
- **Parton distribution functions:** The signal samples generated with the PDF set CTQ6L1 are reweighted to MSTW2008lo68cl following the prescription in [71] using the LHAPDF interface [72]. The uncertainties are estimated with an asymmetric Hessian method and half of the envelope is used as systematic uncertainty.

- **$t\bar{t}$ normalisation**: An uncertainty of 10% for the $t\bar{t}$ cross section is taken into account.

- **Z + jets normalisation:** An uncertainty of 24% per jet is used for the estimation of the uncertainty on the Z + jets cross section. The uncertainties are assumed to be uncorrelated and thus are added in quadrature resulting in a total uncertainty on the Z + jets cross section of 54% in the signal region.

- **W + jets normalisation:** As described in chapter 5.2.2, the normalisation of the W + jets background is a data driven approach. The systematic uncertainties due to the scale factors are varied within their $\pm 1\ \sigma$ uncertainties and compared to the nominal value, resulting in an uncertainty of approx. 28%.

- **Single top normalisation:** The uncertainty on the single top normalisation is estimated using the NNLO cross sections and their uncertainties as quoted in [73, 74, 75] resulting in an approximate uncertainty of 12%.

- **Diboson normalisation:** The uncertainty on the diboson production cross section is 5% as described in [76].

- **QCD multijet normalisation:** For the normalisation of the QCD multijet background, conservative uncertainties of 50% in the electron and 20% in the muon channel are assumed.

9.2. Detector Modelling

- **Jet energy scale:**: Due to the large number of jets in the event in the signal region, the analysis is sensitive to the *jet energy scale* (JES). The JES uncertainty takes amongst others the uncertainties arising from the flavour composition of the jets, the in-situ calibration and close-by jets into account. The energies of the jets are scaled up and down by $1\ \sigma$ of their transverse momentum uncertainty to determine the influence of the JES on the measurement.

- **Jet energy resolution:** The impact of the jet energy resolution is taken into account by Gaussian smearing of the transverse momentum of the jets. Since the resolution in data and MC simulations agree, no smearing of the nominal jet transverse momenta is applied.

- **Jet reconstruction efficiencies:** To account for the jet reconstruction inefficiency of approx. 3% for jets with $p_{\mathrm{T}} < 30$ GeV, an uncertainty is estimated by randomly dropping jets in the Monte Carlo simulation based on their transverse momentum and pseudorapidity.

- **Jet vertex fraction:** To reduce the number of pile-up events, a cut on the jet vertex fraction is applied. The scale factors for the jet vertex fraction efficiency and fake rates are varied within their uncertainty and applied to the MC simulations.

- ***b* tagging scale factors:** In the signal region, events with at least two b-tagged jets are selected. Systematic uncertainties due to b-tagging are taken into account by shifting the scale factors for the b-tagging efficiency and mistag rates by $\pm$ 1 σ.
- **Muon efficiencies:** To achieve better agreement between simulation and data, scale factors for the muon trigger efficiency, reconstruction and identification efficiency are applied. These scale factors are determined in $Z \to \mu\mu$ events using the tag & probe method. The scale factors are varied within their uncertainty (up and down variation) to account for systematic uncertainties.
- **Muon momentum scale and resolution:** To account for discrepancies between the muon resolution in data and Monte Carlo, the momentum of the muons is smeared and scaled according to dimuon mass resolution at the Z-pole. The p_{T} of the muon in the inner detector and the muon spectrometer are smeared separately. For the systematic uncertainty, the inner detector and muon spectrometer track are smeared by $\pm$ 1 σ and half of the difference of the maximal and minimal variation is considered as uncertainty.
- **Electron efficiencies:** Systematic uncertainties arising from the electron trigger, reconstruction, identification and isolation efficiencies are estimated in the same way as for the muons.
- **Electron energy scale and resolution:** The electron energy scale and resolution are determined in $Z \to ee$ events. Since the simulated energy resolution does not reflect the resolution in data, a Gaussian smearing to the transverse energy of the electron is applied. The energy resolution and scale are varied within their uncertainty and the largest variation is used as systematic uncertainty.

10. Statistical Treatment

In this chapter, the $\mathrm{CL_s}$ method is introduced which is used to interpret the results presented in chapter 11. The $\mathrm{CL_s}$ method has been introduced at the LEP experiment for the combined search for the Higgs boson. Within this context, the $\mathrm{CL_s}$ method, based on a profile likelihood ratio is used to set upper limits on the singlet and triplet production cross sections.

10.1. $\mathrm{CL_s}$ Method

With the $\mathrm{CL_s}$ method [77, 78], which is based on frequentist statistics, confidence levels for searches for new particles are calculated. The $\mathrm{CL_s}$ method is applied to searches with small expected number of signal s and background b events, and assuming Poisson statistics. Two hypotheses are tested to calculate the confidence levels: the *background-only* and the *signal-plus-background hypothesis.*

Assuming that the search is performed in n channels or bins, which are statistically independent, the likelihood to observe d_i events under the assumption of the signal-plus-background hypothesis, is given by

$$\mathcal{L}(d|s+b) = \prod_{i=1}^{n} \frac{(s_i+b_i)^{d_i}}{d_i!} \exp(-(s_i+b_i)) \ ,$$

whereas the likelihood for the null hypothesis (background only) is:

$$\mathcal{L}(d|b) = \prod_{i=1}^{n} \frac{b_i^{d_i}}{d_i!} \exp(-b_i) \ .$$

To discriminate between signal-like and background-like outcomes, a test statistic Q is defined. The optimal choice, according to the Neyman-Pearson lemma [79] is the likelihood ratio test statistic:

$$\begin{aligned} Q &= -2\ln\frac{\mathcal{L}(d|s+b)}{\mathcal{L}(d|b)} \ , \\ &= 2\sum_{i=1}^{n} s_i - 2\sum_{i=1}^{n} d_i \ln\left(1+\frac{s_i}{b_i}\right) \ . \end{aligned}$$

Fig. 10.1 shows the probability density functions of the test statistic Q for the background-only hypothesis $f(Q|b)$ and signal + background hypothesis $f(Q|s+b)$. The distributions have been created by performing $5 \cdot 10^5$ pseudo-experiments with $s = 30$ and $b = 60$ expected signal and background events. The vertical line indicates the test statistic Q_{obs} for the observed number of events, $d = 70$ observed events.

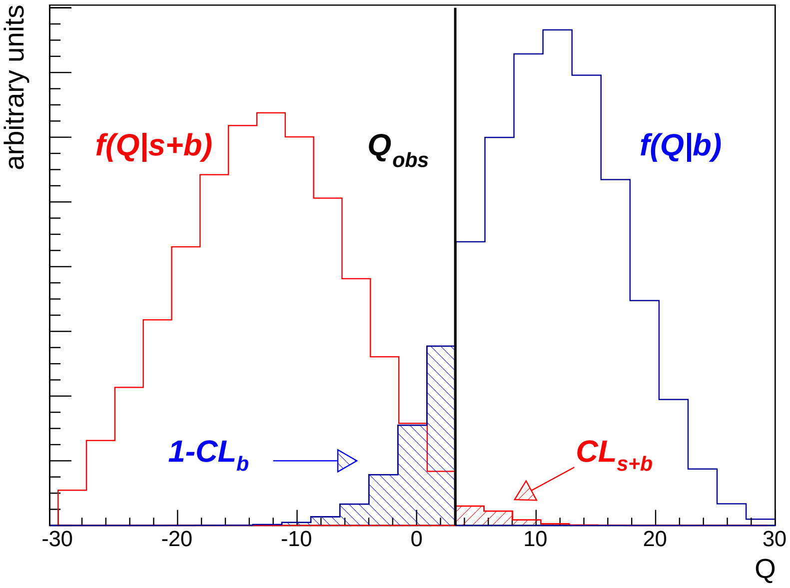

Figure 10.1.: Probability density functions of the test statistic Q for the background-only $f(Q|b)$ and signal-plus-background hypothesis $f(Q|s+b)$ assuming $s = 30$ and $b = 60$ expected signal and background events. The test statistic Q_{obs} for the observed number of data events $d = 70$ is indicated as the horizontal line. The shaded areas show the confidence levels for the signal-plus-background CL_{s+b} and background only hypothesis CL_b.

The probability that the test statistic is less than Q_{obs} under the assumption of the background only hypothesis is given by:

$$P(Q < Q_{\text{obs}}) = 1 - \text{CL}_b \ ,$$

where CL_b is defined as:

$$\text{CL}_b = \int_{Q_{\text{obs}}}^{\infty} f(Q|b) \, \mathrm{d}Q \ .$$

The confidence level for excluding the signal-plus-background hypothesis is defined as the probability of the test statistic being larger than the observed value in data:

$$\text{CL}_{s+b} = P(Q > Q_{\text{obs}}) \ ,$$

with

$$\text{CL}_{s+b} = \int_{Q_{\text{obs}}}^{\infty} f(Q|s+b) \, \mathrm{d}Q \ .$$

For $\mathrm{CL}_{s+b} < \alpha$, the signal-plus-background hypothesis is excluded at confidence level of $1 - \alpha$. The disadvantage of using CL_{s+b} is that if the number of observed events is less than the number of predicted background events, the signal-plus-background hypothesis could be excluded even though the experiment is not sensitive to the signal because of small expected signal yields. To account for this effect, the *Modified Frequentist confidence level* CL_s was introduced:

$$\mathrm{CL}_s = \frac{\mathrm{CL}_{s+b}}{\mathrm{CL}_b} = \frac{p_{s+b}}{1 - p_b} \; .$$

The upper limits from CL_s are weaker than the ones from CL_{s+b} since $\mathrm{CL}_s > \mathrm{CL}_{s+b}$. As for CL_{s+b}, the signal-plus-background hypothesis is excluded at 95% confidence level if $\mathrm{CL}_s < 0.05$.

11. Results

In Chapter 6.3 and Appendix A, it was shown that the background processes for the production of a resonance in $t\bar{t}$ +jets events are well modelled in the defined control regions. In the following, the signal region with at least five jets and one b-tagged jet is analysed. Control region plots are shown, followed by the evaluation of the systematic uncertainties. Since no deviations from the Standard Model expectations are observed, upper limits on the signal production cross section are set.

11.1. Control Plots and Event Yields

In Tab. 11.1, the numbers of expected events from Monte Carlo predictions and data driven methods are compared to the numbers of observed events in the data sample in the single electron and muon channels. As expected, more events in the μ + jets channel are observed due to the tighter cut on the missing transverse energy in the e + jets channel. Within the statistical and systematic uncertainties, the number of expected events is in agreement with the number of observed events in the electron and muon channel. As explained before, the normalisation in the muon channel is not well described by Monte Carlo predictions and currently studied.

Process	single electron channel	single muon channel
$t\bar{t}$	6406 ± 1258	10601 ± 1993
Single top	331 ± 103	557 ± 156
W + jets	473 ± 248	1050 ± 461
Z + jets	138 ± 97	129 ± 111
Diboson	10 ± 8	13 ± 12
QCD multijet	614 ± 327	506 ± 112
Total predicted	7972 ± 1331	12856 ± 2058
Total observed	8631	14704

Table 11.1.: Comparison of the expected number of events and the number of observed events. The uncertainties are statistical and include all systematic uncertainties except for the $t\bar{t}$ modelling systematics (generator and parton shower model) and the initial and final state radiation.

Control region plots for the single muon and electron channel are depicted in Fig. 11.1 and 11.2. A good agreement between the observation and prediction is achieved within the statistical and systematic uncertainties. In addition, the invariant mass distributions of the top-jet system and the antitop-jet system, which are sensitive to the mass of the singlet and triplet, are shown in

Fig. 11.3. Further control plots showing distributions of the kinematic event reconstruction can be found in Appendix D. As described in Chapter 8.2, the m_{tj} and $m_{\bar{t}j}$ distributions are used as input for the two-dimensional binning method to perform the counting experiment in a single bin depending on the signal sample under study.

11.2. Systematic Uncertainties

The full list of systematic uncertainties, summarised in Chapter 9 are evaluated for each singlet and triplet sample due to the different optimised $m_{tj} - m_{\bar{t}j}$ mass windows. The uncertainties on the choice of the parton distribution function utilised in the MadGraph MC generator for the modelling of the singlet and triplet samples are given in Tab. 11.2. The uncertainty due to the PDF increases with the signal mass. Tables 11.3 and 11.4 list the breakdown of systematic uncertainties exemplary for the singlet and triplet sample with a mass of 400 GeV for the electron and muon channel. The systematic uncertainties arising from the modelling of the signal and background processes and from the detector modelling were treated as uncorrelated and thus added in quadrature. For the signal and background samples, the jet energy scale is the dominating systematic uncertainty.

Sample mass [GeV]	PDF uncertainty	
	Singlet [%]	Triplet [%]
200	1.3	1.3
300	1.4	1.4
400	1.5	1.5
500	1.7	1.7
600	2.0	1.8
700	2.1	2.1
800	2.4	2.8
1000	3.7	3.2
1250	4.5	4.4
1500	6.6	5.7
1750	7.4	6.6
2000	8.5	7.6

Table 11.2.: Systematic uncertainty due to the parton distribution functions of the different singlet and triplet samples. The signal samples were generated with CTQ6L1 and were reweighted to MSTW2008lo68cl to estimate the uncertainty.

Electron channel

Systematic	$t\bar{t}$ [%]	W + jets [%]	Total [%]	Signal [%]
Jet energy scale	$^{+16.1}_{-14.7}$	$^{+19.9}_{-25.2}$	$^{+12.2}_{-11.3}$	$^{+11.4}_{-11.8}$
Jet reconstruction efficiency	± 1.2	± 0.0	± 0.1	± 2.1
Jet energy resolution	± 6.9	± 14.6	± 5.3	± 0.4
Jet vertex fraction efficiency	± 1.4	± 1.9	± 1.1	± 1.7
b-tag scale factors	± 5.3	± 9.4	± 4.0	± 4.6
Electron efficiencies	± 2.4	± 2.4	± 1.8	± 2.4
Electron smearing	± 0.2	± 8.1	± 0.8	± 3.6
Electron energy scale	± 0.2	± 9.4	± 0.9	± 3.1
Generator	± 24.5	–	± 18.2	–
Parton Shower	± 0.3	–	± 0.3	–
ISR/FSR	± 7.9	–	± 5.9	± 10.3
Luminosity	± 1.8	± 1.8	± 1.8	± 1.8

Muon channel

Systematic	$t\bar{t}$ [%]	W + jets [%]	Total [%]	Signal [%]
Jet energy scale	$^{+13.4}_{-13.3}$	$^{+39.0}_{-17.3}$	$^{+11.4}_{-10.9}$	$^{+17.3}_{-11.5}$
Jet reconstruction efficiency	± 0.2	± 0.0	± 0.2	± 5.6
Jet energy resolution	± 1.2	± 22.5	± 2.2	± 0.6
Jet vertex fraction efficiency	± 1.5	± 1.4	± 1.2	± 1.8
b-tag scale factors	± 4.6	± 9.6	± 3.8	± 4.8
Muon efficiencies	± 1.5	± 1.4	± 1.2	± 1.5
Muon smearing	± 0.0	± 0.0	± 0.0	± 0.3
Muon momentum scale	± 0.0	± 1.6	± 0.1	± 0.8
Generator	± 18.6	–	± 14.9	–
Parton Shower	± 4.8	–	± 3.9	–
ISR/FSR	± 9.7	–	± 7.9	± 10.3
Luminosity	± 1.8	± 1.8	± 1.8	± 1.8

Table 11.3.: Systematic uncertainties on the signal and background samples in the signal region optimised for the 400 GeV singlet sample.

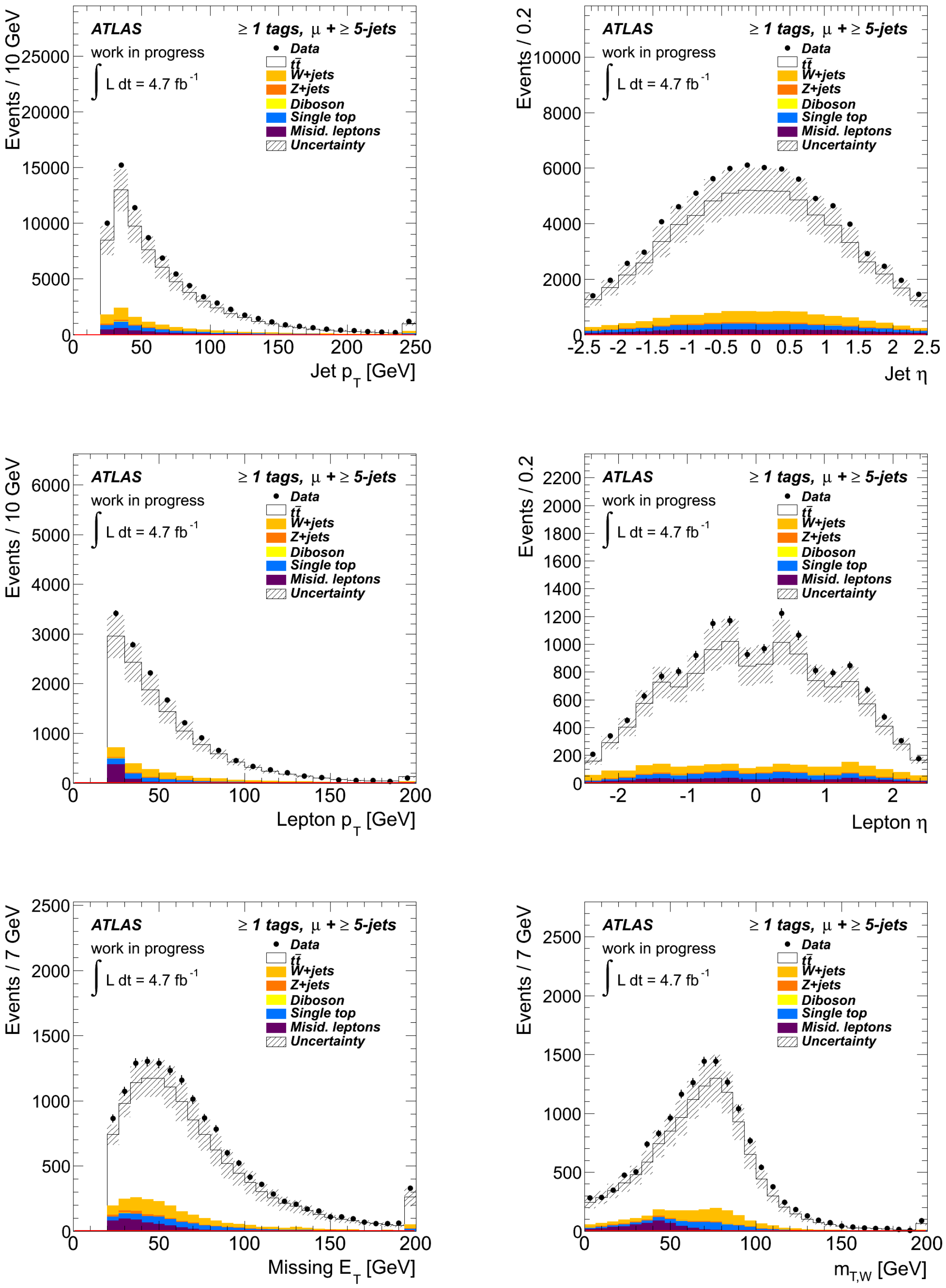

Figure 11.1.: Control plots for the μ + jets channel. The transverse momentum p_{T} and the pseudorapidity η of the jets and the muon are shown as well as the missing transverse energy distribution $E_{\mathrm{T}}^{\mathrm{miss}}$ and the transverse W-boson mass $m_{\mathrm{T}}(W)$. The uncertainties are statistical and all systematic uncertainties except for ISR/FSR and the $t\bar{t}$ modelling uncertainties.

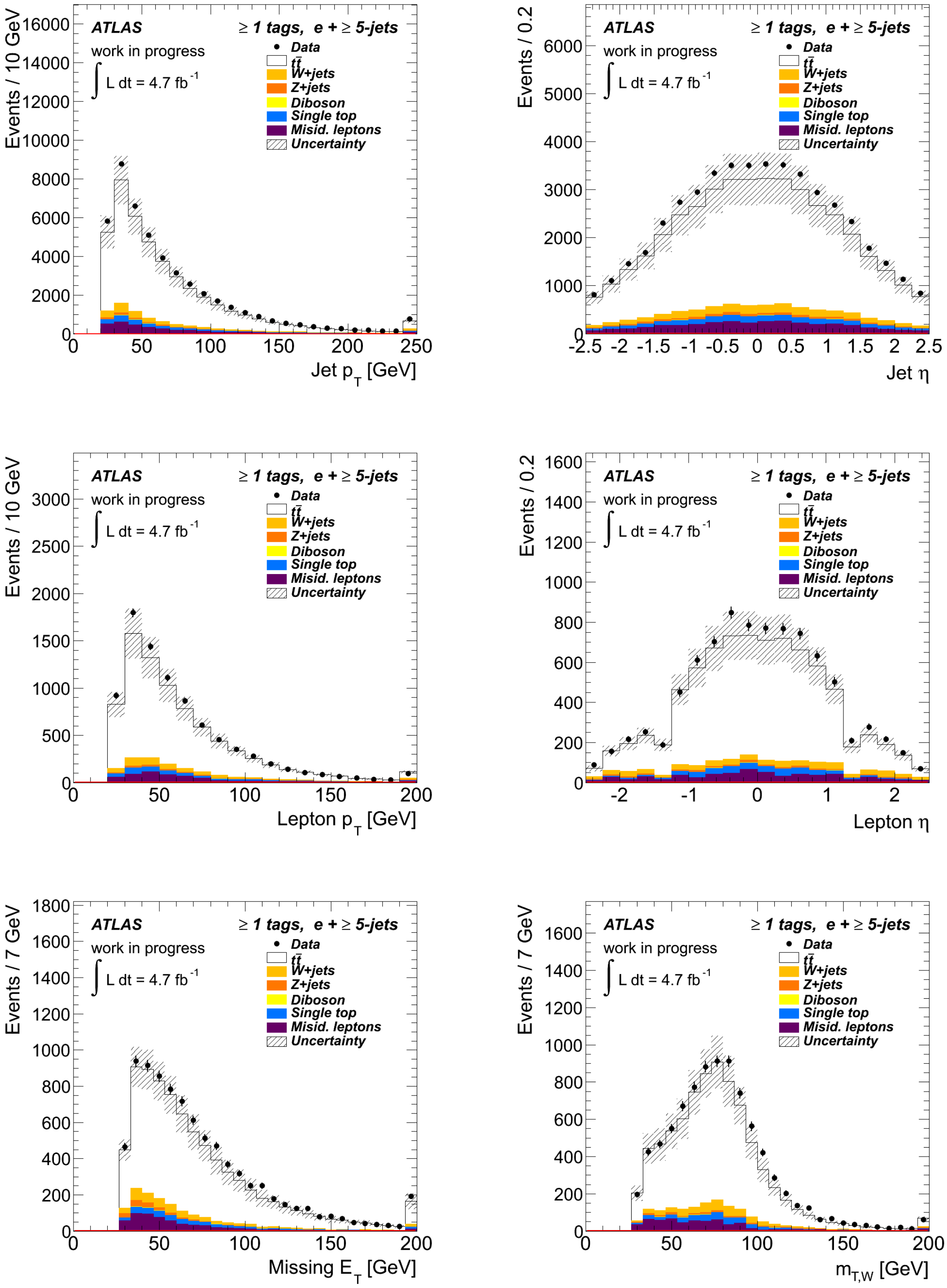

Figure 11.2.: Control plots for the e + jets channel. The transverse momentum p_{T} and the pseudorapidity η of the jets and the electron are shown as well as the missing transverse energy distribution $E_{\mathrm{T}}^{\mathrm{miss}}$ and the transverse W-boson mass $m_{\mathrm{T}}(W)$. The uncertainties are statistical and all systematic uncertainties except for ISR/FSR and the $t\bar{t}$ modelling uncertainties.

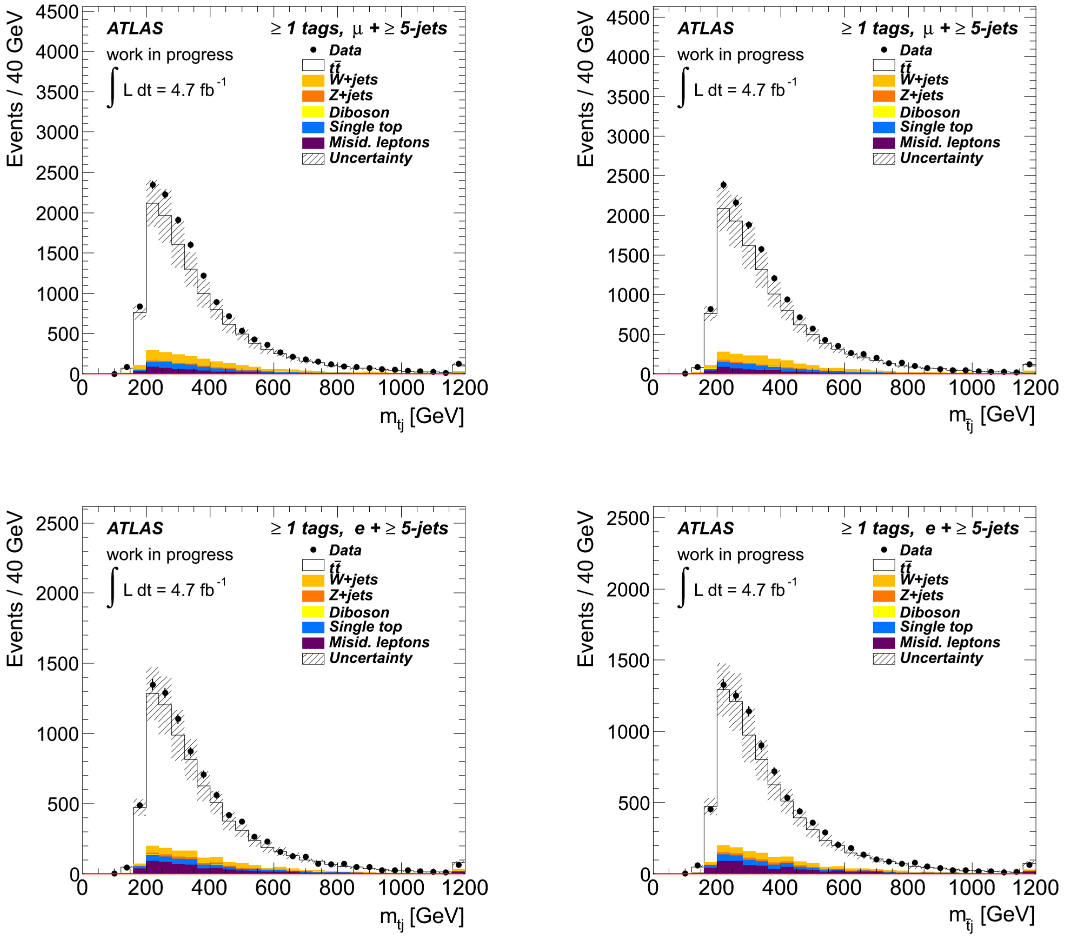

Figure 11.3.: Invariant mass distributions of the top-jet and antitop-jet system m_{tj} and $m_{\bar{t}j}$ for the μ + jets (a, b) and e +jets (c, d) channel.

Electron channel				
Systematic	$t\bar{t}$ [%]	W + jets [%]	Total [%]	Signal [%]
Jet energy scale	$^{+15.3}_{-13.0}$	$^{+13.8}_{-19.2}$	$^{+11.2}_{-\ 9.7}$	$^{+10.1}_{-19.7}$
Jet reconstruction efficiency	± 0.6	± 0.0	± 0.4	± 1.3
Jet energy resolution	± 2.4	± 7.1	± 1.9	± 0.6
Jet vertex fraction efficiency	± 1.4	± 1.1	± 1.0	± 1.7
b-tag scale factors	± 3.8	± 10.6	± 2.9	± 5.6
Electron efficiencies	± 2.4	± 2.5	± 1.8	± 2.5
Electron smearing	± 0.5	± 0.2	± 0.4	± 1.6
Electron energy scale	± 0.1	± 3.0	± 0.4	± 2.5
Generator	± 19.3	–	± 14.1	–
Parton Shower	± 1.1	–	± 0.8	–
ISR/FSR	± 7.5	–	± 5.5	± 10.3
Luminosity	± 1.8	± 1.8	± 1.8	± 1.8
Muon channel				
Systematic	$t\bar{t}$ [%]	W + jets [%]	Total [%]	Signal [%]
Jet energy scale	$^{+14.3}_{-13.4}$	$^{+13.9}_{-43.8}$	$^{+11.4}_{-11.7}$	$^{+22.3}_{-15.4}$
Jet reconstruction efficiency	± 0.0	± 2.0	± 0.2	± 2.1
Jet energy resolution	± 0.1	± 12.2	± 1.4	± 0.5
Jet vertex fraction efficiency	± 1.4	± 2.6	± 1.1	± 1.7
b-tag scale factors	± 4.9	± 9.7	± 4.0	± 8.1
Muon efficiencies	± 1.5	± 1.4	± 1.2	± 1.4
Muon smearing	± 0.2	± 0.6	± 0.2	± 0.0
Muon momentum scale	± 0.3	± 3.2	± 0.5	± 0.7
Generator	± 18.8	–	± 14.6	–
Parton Shower	± 3.1	–	± 2.4	–
ISR/FSR	± 9.8	–	± 7.7	± 10.3
Luminosity	± 1.8	± 1.8	± 1.8	± 1.8

Table 11.4.: Systematic uncertainties on the signal and background samples in the signal region optimised for the 400 GeV triplet sample.

11.3. Limit Setting

The number of expected signal and background events as well as the number of observed events after applying the cuts on the m_{tj} and $m_{\bar{t}j}$ variables are listed in Tab. 11.5 and Tab. 11.6 for each singlet and triplet sample, respectively. The uncertainties on the prediction are statistical and systematic uncertainties. As a simplification, the electron and muon channels were assumed to be uncorrelated. The number of background events depends on the signal mass due to the different optimised m_{tj}–$m_{\bar{t}j}$ bins, see Fig. 8.2.

Signal Mass	Background (expected)	Signal (expected)	Observed
200 GeV	561^{+87}_{-83}	424^{+56}_{-104}	627
300 GeV	773^{+118}_{-119}	387^{+57}_{-46}	924
400 GeV	598^{+99}_{-96}	214^{+30}_{-24}	662
500 GeV	425^{+67}_{-66}	107^{+18}_{-19}	470
600 GeV	284^{+48}_{-47}	54^{+10}_{-10}	301
700 GeV	194^{+35}_{-32}	32^{+6}_{-7}	208
800 GeV	134^{+24}_{-23}	17^{+4}_{-5}	151
1000 GeV	165^{+28}_{-27}	8^{+2}_{-3}	139
1250 GeV	48^{+12}_{-10}	1^{+1}_{-1}	38
1500 GeV	22^{+8}_{-7}	0^{+1}_{-1}	17
1750 GeV	22^{+8}_{-7}	0^{+1}_{-1}	17
2000 GeV	23^{+8}_{-7}	0^{+1}_{-1}	17

Table 11.5.: Expected number of background, signal and observed events for different singlet samples, fulfilling the cuts on m_{tj} and $m_{\bar{t}j}$, defined in chapter 8.2.

For each signal sample, the p-value and the significance are calculated and listed in Tab. 11.7. The p-value is defined as the probability to observe more events than the number of measured data events under the background-only hypothesis. For values $p > 0.005$, the observation is consistent with the *background-only* hypothesis. For each mass window, the observation is consistent with the Standard Model hypotheses and 95% confidence level upper limits on the signal cross section are set.

The upper limits on the cross section are computed based on the CL$_s$ method as described in Chapter 10. The MCLimit package [80] is used to calculate the 95% C.L. expected and observed upper cross section limits $\sigma_{95\%}$. 10000 pseudo-experiments were performed to create the probability density functions for the *background-only* and *signal-plus-background* hypotheses. Exemplary, the probability density functions for the two hypotheses for the singlet sample with a mass of 400 GeV are shown in Fig. 11.4 without taking the systematic uncertainties into account. With systematic uncertainties, the parton distribution functions are smeared out around the central value. The scale factor at which the signal is excluded at 95% C.L. is defined as $s95 = \frac{\sigma_{95\%}}{\sigma_{SM}}$ and is listed in Tab. 11.8. Furthermore, the scale factor is shown as a function of the resonance mass in Fig. 11.5. For $s95 < 1$, the signal can be excluded at 95% confidence level. Hence, no 95% C.L. lower limits on the mass of the new resonance can be set in the analysed mass range due to the large systematic uncertainties. Masses below 430 GeV and 220 GeV for the singlet and triplet, respectively, were expected to be excluded. Without taking the systematic uncertainties into account, the lower limit on the mass of the colour singlet is 534 GeV whereas the expected lower limit is 620 GeV, assuming a unit right-handed coupling. For the colour triplet sample, the limit on the mass is 630 GeV, where it was expected to set a limit at 700 GeV.

Signal Mass	Expected events	Signal (expected)	Observed
200 GeV	$2272\,^{+349}_{-322}$	$713\,^{+131}_{-\ 72}$	2467
300 GeV	$1295\,^{+206}_{-197}$	$456\,^{+\ 99}_{-\ 81}$	1512
400 GeV	$667\,^{+101}_{-\ 99}$	$240\,^{+\ 40}_{-\ 33}$	725
500 GeV	$328\,^{+\ 57}_{-\ 53}$	$115\,^{+\ 20}_{-\ 22}$	373
600 GeV	$178\,^{+\ 33}_{-\ 30}$	$58\,^{+\ 11}_{-\ 12}$	193
700 GeV	$103\,^{+\ 19}_{-\ 19}$	$32\,^{+\ 7}_{-\ 7}$	113
800 GeV	$56\,^{+\ 13}_{-\ 13}$	$13\,^{+\ 4}_{-\ 4}$	57
1000 GeV	$186\,^{+\ 35}_{-\ 32}$	$19\,^{+\ 14}_{-\ 14}$	169
1250 GeV	$60\,^{+\ 13}_{-\ 13}$	$5\,^{+\ 2}_{-\ 2}$	39
1500 GeV	$18\,^{+\ 7}_{-\ 7}$	$1\,^{+\ 1}_{-\ 1}$	13
1750 GeV	$18\,^{+\ 7}_{-\ 7}$	$1\,^{+\ 1}_{-\ 1}$	13
2000 GeV	$18\,^{+\ 7}_{-\ 7}$	$0\,^{+\ 1}_{-\ 1}$	13

Table 11.6.: Expected number of background, signal and observed events for different triplet samples, fulfilling the cuts on m_{tj} and $m_{\bar{t}j}$, defined in chapter 8.2.

Signal Mass	Singlet		Triplet	
	p-value	Significance	p-value	Significance
200 GeV	0.28	0.60	0.32	0.47
300 GeV	0.11	1.23	0.17	0.96
400 GeV	0.31	0.49	0.35	0.38
500 GeV	0.31	0.50	0.26	0.63
600 GeV	0.38	0.30	0.36	0.37
700 GeV	0.36	0.35	0.35	0.39
800 GeV	0.30	0.53	0.48	0.04
1000 GeV	0.70	-0.54	0.59	-0.24
1250 GeV	0.68	-0.49	0.87	-1.12
1500 GeV	0.71	-0.55	0.78	-0.77
1750 GeV	0.71	-0.55	0.78	-0.77
2000 GeV	0.71	-0.55	0.78	-0.77

Table 11.7.: p-value and significance of the different signal samples to show the consistency of the observation with the Standard Model background.

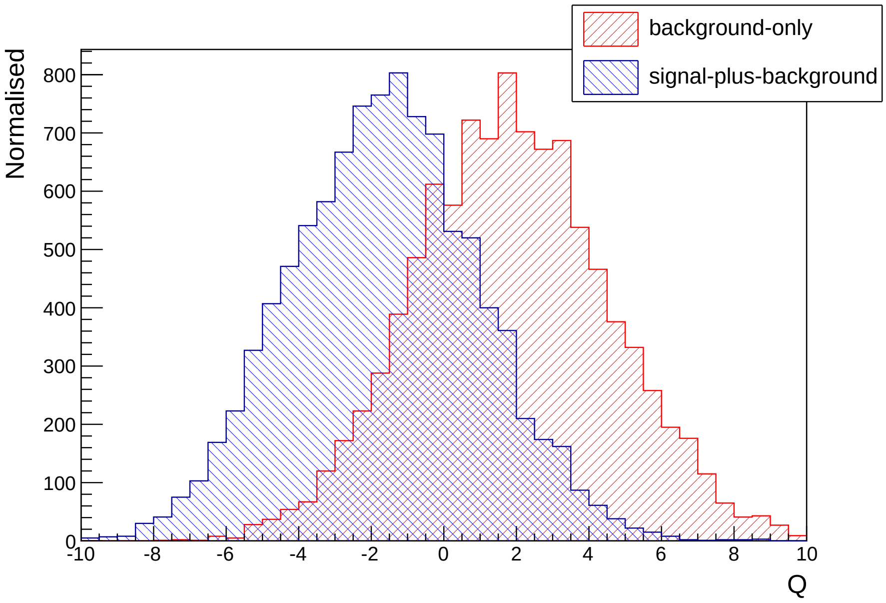

Figure 11.4.: Probability density functions of the test statistic Q for the background-only (red) and signal-plus-background hypothesis (blue) for the singlet sample with 400 GeV if no systematic uncertainties are considered. The test statistic for the observation yields $Q = 22.8$.

Sample	Singlet			Triplet		
	$s95$	$s95_{\mathrm{exp}}$	$\sigma_{95\%}$ [pb]	$s95$	$s95_{\mathrm{exp}}$	$\sigma_{95\%}$ [pb]
200 GeV	1.03	0.92	58.80	1.24	0.98	55.80
300 GeV	1.15	0.78	21.05	1.71	1.23	29.93
400 GeV	1.40	1.13	10.36	1.32	1.09	10.44
500 GeV	2.39	1.98	7.78	1.92	1.54	7.49
600 GeV	2.73	2.39	4.23	2.14	1.90	4.45
700 GeV	4.46	3.88	3.50	2.73	2.39	3.14
800 GeV	9.12	7.84	6.25	5.85	4.16	3.89

Table 11.8.: Scale factor $s95$ at which the signal is excluded at 95 % confidence level and the expected scale factor for the null hypothesis. Furthermore, the scale factor is translated into the upper signal cross section limit.

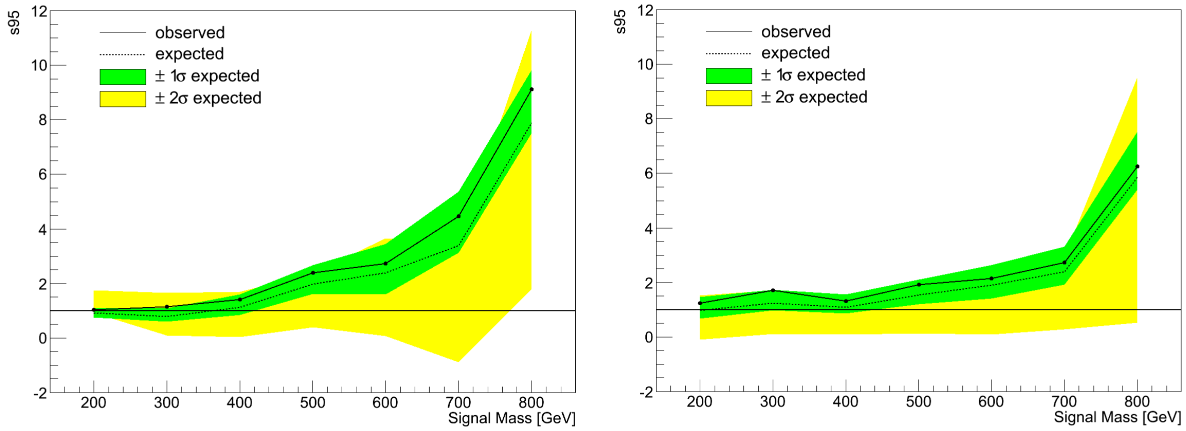

Figure 11.5.: Scale factor $s95$ at which the signal is excluded at 95% C.L. as a function of the mass of the colour singlet (a) or triplet (b).

12. Conclusion and Outlook

In this thesis, a search for a new top-flavour violating particle in association with a top quark was performed using the full 2011 dataset collected with the ATLAS detector and corresponding to an integrated luminosity of 4.7 fb^{-1} of proton-proton collisions at a centre-of-mass energy of $\sqrt{s} = 7$ TeV. Two different models were considered in the analysis: a colour singlet and a colour triplet which could explain the anomalous forward-backward asymmetry measured in top quark production at the Tevatron. The new particle decays either into a top plus light jet or an antitop plus light jet, resulting in a resonance in $t\bar{t}$ + jet final states.

Events passing the event selection criteria were reconstructed with the Kinematic Likelihood Fitter under the assumption of the lepton + jets decay topology. In order to maximise the reconstruction efficiency for a possible signal, several configurations of the fitter were tested and compared. An event selection was applied which reduces the number of W + jets events significantly; the Standard Model production of top-antitop pairs remains an irreducible background. Therefore, a two-dimensional binning method in the m_{tj}–$m_{\bar{t}j}$ mass plane was applied, resulting in a single bin counting experiment. This binning method was optimised for each singlet and triplet sample, taking all systematic uncertainties into account. For each singlet and triplet sample, the systematic uncertainties were evaluated. The event yields in the different signal regions were determined and compared to the observation which is consistent with the background-only hypothesis. Hence, upper limits on the signal cross section were set with the CL_s method, based on a frequentist approach. Assuming a unit right-handed coupling, no lower limits on the mass of the new particles could be set in the studied range due too the large systematic uncertainties. It was expected to exclude a new singlet state with $m < 430$ GeV and a triplet with $m < 220$ GeV.

To finalise these studies, the electron and muon channel need to be properly combined taking into account correlations between both channels. In addition, the discrepancies between the predicted and observed number of events, arising from the mismodelling of the production of $t\bar{t}$ pairs with additional jets, need to be further investigated. Especially the systematic uncertainties need to be minimised in order to be able to exclude mass ranges for the singlet or triplet. In order to improve the sensitivity of the analysis, further optimisation studies need to be performed. The angle between the top and the light jet or the antitop and the light jet could be used as discriminating variable between the dominating background sources and the signal. In the SM, the additional jet is produced via initial or final state radiation which would result in a uniform distribution of the angle as a function of the tj and $\bar{t}j$ mass. If the mass of the new particle is sufficiently low, the decay products of the particle are boosted, resulting in a small angle between the decay products. If, however, the new particle is produced at rest due to its large mass, the decay products are emitted back-to-back.

Bibliography

[1] D. Griffiths, *Introduction to elementary particles*, Weinheim, Germany: Wiley-VCH (2008) .

[2] F. Halzen and A. D. Martin, *Quarks and Leptons: An Introductory Course In Modern Particle Physics*, John Wiley and Sons (1984) .

[3] J. Erler and P. Langacker, *Electroweak model and constraints on new physics*, Review of Particle Physics (2011) .

[4] Particle Data Group Collaboration, J. Beringer et al., *Review of Particle Physics (RPP)*, Phys.Rev. **D86** (2012) 010001.

[5] M. E. Peskin and D. V. Schroeder, *An Introduction to quantum field theory*, Addison-Wesley (1995) .

[6] F. Englert and R. Brout, *Broken Symmetry and the Mass of Gauge Vector Mesons*, Phys.Rev.Lett. **13** (1964) 321–323.

[7] P. W. Higgs, *Broken Symmetries and the Masses of Gauge Bosons*, Phys.Rev.Lett. **13** (1964) 508–509.

[8] ATLAS Collaboration, *Observation of a new particle in the search for the Standard Model Higgs boson with the ATLAS detector at the LHC*, Phys.Lett. **B716** (2012) 1–29.

[9] CMS Collaboration, *Observation of a new boson at a mass of 125 GeV with the CMS experiment at the LHC*, Phys.Lett. **B716** (2012) 30–61.

[10] D0 Collaboration, S. Abachi et al., *Observation of the top quark*, Phys.Rev.Lett. **74** (1995) 2632–2637.

[11] CDF Collaboration, F. Abe et al., *Observation of top quark production in $\bar{p}p$ collisions*, Phys.Rev.Lett. **74** (1995) 2626–2631.

[12] S. Herb, D. Hom, L. Lederman, J. Sens, H. Snyder, et al., *Observation of a Dimuon Resonance at 9.5-GeV in 400-GeV Proton-Nucleus Collisions*, Phys.Rev.Lett. **39** (1977) 252–255.

[13] Tevatron Electroweak Working Group, for the CDF and D0 Collaboration, *Combination of CDF and D0 results on the mass of the top quark using up to 5.8 fb-1 of data*, ArXiv e-prints (2011) , `arXiv:1107.5255 [hep-ex]`.

[14] *HERA - A Proposal for a Large Electron Proton Colliding Beam Facility at DESY*, DESY-HERA-81-10 (1981) .

[15] G. Altarelli and G. Parisi, *Asymptotic Freedom in Parton Language*, Nucl.Phys. **B126** (1977) 298.

[16] H.-L. Lai et al., *New parton distributions for collider physics*, Phys. Rev. **D82** (2010) 074024.

[17] M. Aliev, H. Lacker, U. Langenfeld, S. Moch, P. Uwer, et al., *HATHOR: HAdronic Top and Heavy quarks crOss section calculatoR*, Comput.Phys.Commun. **182** (2011) 1034–1046.

[18] D0 Collaboration, V. Abazov et al., *Observation of Single Top Quark Production*, Phys.Rev.Lett. **103** (2009) 092001.

[19] CDF Collaboration, T. Aaltonen et al., *First Observation of Electroweak Single Top Quark Production*, Phys.Rev.Lett. **103** (2009) 092002.

[20] CDF Collaboration, T. Aaltonen et al., *Evidence for a Mass Dependent Forward-Backward Asymmetry in Top Quark Pair Production*, Phys.Rev. **D83** (2011) 112003.

[21] D0 Collaboration, V. M. Abazov et al., *Forward-backward asymmetry in top quark-antiquark production*, Phys.Rev. **D84** (2011) 112005.

[22] ATLAS Collaboration, *Measurement of the charge asymmetry in top quark pair production in pp collisions at sqrt(s) = 7 TeV using the ATLAS detector*, Eur.Phys.J. **C72** (2012) 2039.

[23] CMS Collaboration, *Inclusive and differential measurements of the $t\bar{t}$ charge asymmetry in proton-proton collisions at 7 TeV*, ArXiv e-prints (2012) , `arXiv:1207.0065 [hep-ex]`.

[24] J. H. Kuhn and G. Rodrigo, *Charge asymmetries of top quarks at hadron colliders revisited*, JHEP **1201** (2012) 063.

[25] J. Aguilar-Saavedra and M. Perez-Victoria, *Asymmetries in $t\,\bar{t}$ production: LHC versus Tevatron*, Phys.Rev. **D84** (2011) 115013.

[26] A. Arhrib, R. Benbrik, and C.-H. Chen, *Forward-backward asymmetry of top quark in diquark models*, Phys.Rev. **D82** (2010) 034034.

[27] J. Shu, T. M. Tait, and K. Wang, *Explorations of the Top Quark Forward-Backward Asymmetry at the Tevatron*, Phys.Rev. **D81** (2010) 034012.

[28] J. Aguilar-Saavedra and M. Perez-Victoria, *Simple models for the top asymmetry: Constraints and predictions*, JHEP **1109** (2011) 097.

[29] M. I. Gresham, I.-W. Kim, and K. M. Zurek, *Searching for Top Flavor Violating Resonances*, Phys.Rev. **D84** (2011) 034025.

[30] Y. Cui, Z. Han, and M. D. Schwartz, *Top condensation as a motivated explanation of the top forward-backward asymmetry*, JHEP **1107** (2011) 127.

[31] S. Knapen, Y. Zhao, and M. J. Strassler, *Diagnosing the Top-Quark Angular Asymmetry using LHC Intrinsic charge Asymmetries*, Phys.Rev. **D86** (2012) 014013.

[32] CDF Collaboration, T. Aaltonen et al., *Search for top+jet resonances in* $t\bar{t}$*+jet(s) at CDF*, CDF CONF. Note 10776 (2012) . `http://www-cdf.fnal.gov/physics/new/top/confNotes/cdf10776_ttj.pdf`.

[33] CMS Collaboration, S. Chatrchyan et al., *Search for charge-asymmetric production of W' bosons in top pair + jet events from pp collisions at sqrt(s) = 7 TeV*, ArXiv e-prints (2012) , `arXiv:1206.3921 [hep-ex]`.

[34] E. Bruning, Oliver S., E. Collier, P., E. Lebrun, P., E. Myers, S., E. Ostojic, R., et al., *LHC Design Report. 1. The LHC Main Ring*, CERN-2004-003 (2004) .

[35] E. Benedikt, M., E. Collier, P., E. Mertens, V., E. Poole, J., and E. Schindl, K., *LHC Design Report. 3. The LHC injector chain*, CERN-2004-003 (2004) .

[36] *The Accelerator Complex*, `http://public.web.cern.ch/public/en/research/AccelComplex-en.html`, (Aug. 2012).

[37] The ATLAS Collaboration, *ATLAS: Detector and physics performance technical design report. Volume 1*, CERN-LHCC-99-14 (1999) .

[38] The CMS Collaboration, *CMS physics: Technical design report*, CERN-LHCC-2006-001 (2006) .

[39] The ALICE Collaboration, *ALICE: Technical proposal for a large ion collider experiment at the CERN LHC*, CERN-LHCC-95-71 (1995) .

[40] LHCb Collaboration, *LHCb technical proposal*, CERN-LHCC-98-04 (1998) .

[41] *ATLAS Public Luminosity Results*, `https://twiki.cern.ch/twiki/bin/view/AtlasPublic/LuminosityPublicResults`, (Aug. 2012).

[42] ATLAS Collaboration, *The ATLAS Experiment at the CERN Large Hadron Collider*, JINST **3** (2008) S08003.

[43] F.Hugging, On behalf of the ATLAS Collaboration, *The ATLAS Pixel Insertable B-Layer (IBL)*, ArXiv e-prints (2011) , `arXiv:1012.2742`.

[44] C. Grupen and B. Schwartz, *Particle detectors*, Cambridge University Press (2008) .

[45] M. Cacciari, G. P. Salam, and G. Soyez, *The Anti-k(t) jet clustering algorithm*, JHEP **0804** (2008) 063.

[46] ATLAS Collaboration, *Commissioning of the ATLAS high-performance b-tagging algorithms in the 7 TeV collision data*, ATLAS-CONF-2011-102 (2011) .

[47] Atlas Collaboration, *Measurement of the* $W \to \ell\nu$ *and* $Z/\gamma^* \to \ell\ell$ *production cross sections in proton-proton collisions at* $\sqrt{s} = 7$ *TeV with the ATLAS detector*, JHEP **1012** (2010) 060.

[48] *ATLAS Muon Combined Performance, Guidelines for Analyses of 2011 Data in Release 17*, `https://twiki.cern.ch/twiki/bin/viewauth/AtlasProtected/MCPAnalysisGuidelinesRel17MC11a`, (Aug. 2012).

[49] M. L. Mangano, M. Moretti, F. Piccinini, R. Pittau, and A. D. Polosa, *ALPGEN, a generator for hard multiparton processes in hadronic collisions*, JHEP **0307** (2003) 001.

[50] B. P. Kersevan and E. Richter-Was, *The Monte Carlo event generator AcerMC version 2.0 with interfaces to PYTHIA 6.2 and HERWIG 6.5*, ArXiv e-prints (2004) , `arXiv:hep-ph/0405247 [hep-ph]`.

[51] J. Alwall et al., *MadGraph/MadEvent v4: The New Web Generation*, JHEP **09** (2007) 028.

[52] S. Frixione and B. R. Webber, *Matching NLO QCD computations and parton shower simulations*, JHEP **0206** (2002) 029.

[53] T. Sjostrand, S. Mrenna, and P. Z. Skands, *PYTHIA 6.4 Physics and Manual*, JHEP **0605** (2006) 026.

[54] G. Corcella, I. Knowles, G. Marchesini, S. Moretti, K. Odagiri, et al., *HERWIG 6: An Event generator for hadron emission reactions with interfering gluons (including supersymmetric processes)*, JHEP **0101** (2001) 010.

[55] T. Gleisberg, S. Hoeche, F. Krauss, M. Schonherr, S. Schumann, et al., *Event generation with SHERPA 1.1*, JHEP **0902** (2009) 007.

[56] ATLAS Collaboration, *ATLAS computing: Technical design report*, CERN-LHCC-2005-022, ATLAS-TRD-017 (2005) .

[57] GEANT4 Collaboration, S. Agostinelli et al., *GEANT4: A Simulation toolkit*, Nucl.Instrum.Meth. **A506** (2003) 250–303.

[58] J. Butterworth, J. R. Forshaw, and M. Seymour, *Multiparton interactions in photoproduction at HERA*, Z.Phys. **C72** (1996) 637–646.

[59] A. Martin, W. Stirling, R. Thorne, and G. Watt, *Parton distributions for the LHC*, Eur.Phys.J. **C63** (2009) 189–285.

[60] *"The Les Houches Accord PDF Interface"*, `http://lhapdf.hepforge.org/`, "(Aug. 2012)".

[61] P. M. Nadolsky, H.-L. Lai, Q.-H. Cao, J. Huston, J. Pumplin, et al., *Implications of CTEQ global analysis for collider observables*, Phys.Rev. **D78** (2008) 013004.

[62] *Heavy Flavor Overlap Removal.* (Aug. 2012). https://twiki.cern.ch/twiki/bin/viewauth/AtlasProtected.HforTool.

[63] C.-H. Kom and W. J. Stirling, *Charge asymmetry in W + jets production at the LHC*, Eur.Phys.J. **C69** (2010) 67–73.

[64] *TopGRL.* (Aug. 2012). https://twiki.cern.ch/twiki/bin/viewauth/AtlasProtected/TopGRLs#NEW_Final_2011_data_release_17.

[65] *Recommendations for jet cleaning for data 2011 - Bad jets*, `https://twiki.cern.ch/twiki/bin/viewauth/AtlasProtected/HowToCleanJets2011$#$Bad_jets`, (Sept. 2012).

[66] *KLFitter*, `https://twiki.cern.ch/twiki/bin/viewauth/AtlasProtected/KLFitter`, (Aug. 2012).

[67] F. Beaujean, A. Caldwell, D. Kollar, and K. Kroninger, *BAT: The Bayesian analysis toolkit*, J.Phys.Conf.Ser. **331** (2011) 072040.

[68] ATLAS Collaboration, *Search for top-jet resonancees in the lepton+jets final state of* $t\bar{t}$ + *jets events with the ATLAS detector in* $4.7\,fb^{-1}$ *of pp collisions at* $\sqrt{s} = 7$ *TeV* , ATLAS-CONF-2012-96 (2012) .

[69] *TopSystematicUncertainties for Winter 2012 (rel17) 5* fb^{-1} *analyses*, `https://twiki.cern.ch/twiki/bin/viewauth/AtlasProtected/TopSystematicUncertainties2011`, (Sept. 2012).

[70] S. Frixione, P. Nason, and C. Oleari, *Matching NLO QCD computations with Parton Shower simulations: the POWHEG method*, JHEP **0711** (2007) 070.

[71] *TopPdfUncertainty*, `https://twiki.cern.ch/twiki/bin/viewauth/AtlasProtected/TopPdfUncertainty`, (Aug. 2012).

[72] M. Whalley, D. Bourilkov, and R. Group, *The Les Houches accord PDFs (LHAPDF) and LHAGLUE*, ArXiv e-prints (2005) , `arXiv:hep-ph/0508110 [hep-ph]`.

[73] N. Kidonakis, *Next-to-next-to-leading-order collinear and soft gluon corrections for t-channel single top quark production*, Phys.Rev. **D83** (2011) 091503.

[74] N. Kidonakis, *NNLL resummation for s-channel single top quark production*, Phys.Rev. **D81** (2010) 054028.

[75] N. Kidonakis, *Two-loop soft anomalous dimensions for single top quark associated production with a W- or H-*, Phys.Rev. **D82** (2010) 054018.

[76] Atlas Collaboration, *Measurement of the top quark-pair production cross section with ATLAS in pp collisions at* $\sqrt{s} = 7\ TeV$, Eur.Phys.J. **C71** (2011) 1577.

[77] A. L. Read, *Presentation of search results: The CL(s) technique*, J.Phys.G **G28** (2002) 2693–2704.

[78] A. L. Read, *Modified frequentist analysis of search results (The CL(s) method)*, CERN-OPEN-2000-205 (2000) .

[79] J. Neyman and E. Pearson, *On the Problem of the Most Efficient Tests of Statistical Hypotheses*, Philosophical Transactions of the Royal Society of London: Series A, Containing Papers of a Mathematical or Physical Character **231** (1933) 289–337.

[80] T. Junk, *Confidence level computation for combining searches with small statistics*, Nucl.Instrum.Meth. **A434** (1999) 435–443.

A. Control Region Plots

Control region plots for the muon and electron channel in the pretag region with at least four jets and b-tag requirement are depicted in Fig. A.1 - A.4 and for the W + jets region with more than four jets and no b-tagged jet in Fig. A.5 - A.8. The uncertainties on the prediction are statistical and systematic uncertainties on the normalisation of the background as well as uncertainties on the luminosity, b-tag scale factors and electron and muon efficiencies.

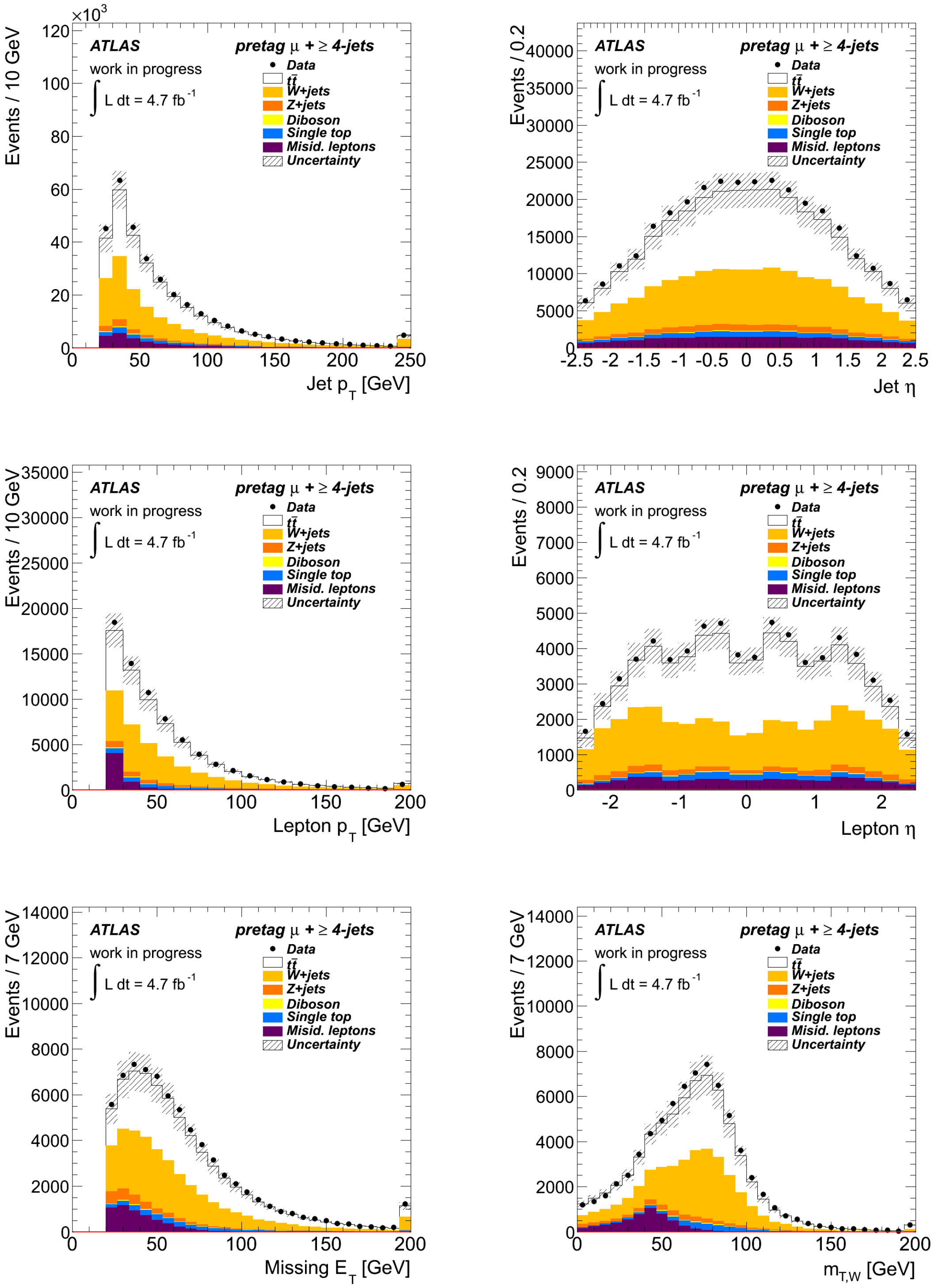

Figure A.1.: Control plots for the μ + jets channel in the pretag region with at least four jets and no b-tag requirement. The transverse momentum p_{T} and the pseudorapidity η of the jets and the muon are shown as well as the missing transverse energy distribution $E_{\mathrm{T}}^{\mathrm{miss}}$ and the transverse W-boson mass $m_{\mathrm{T}}(W)$.

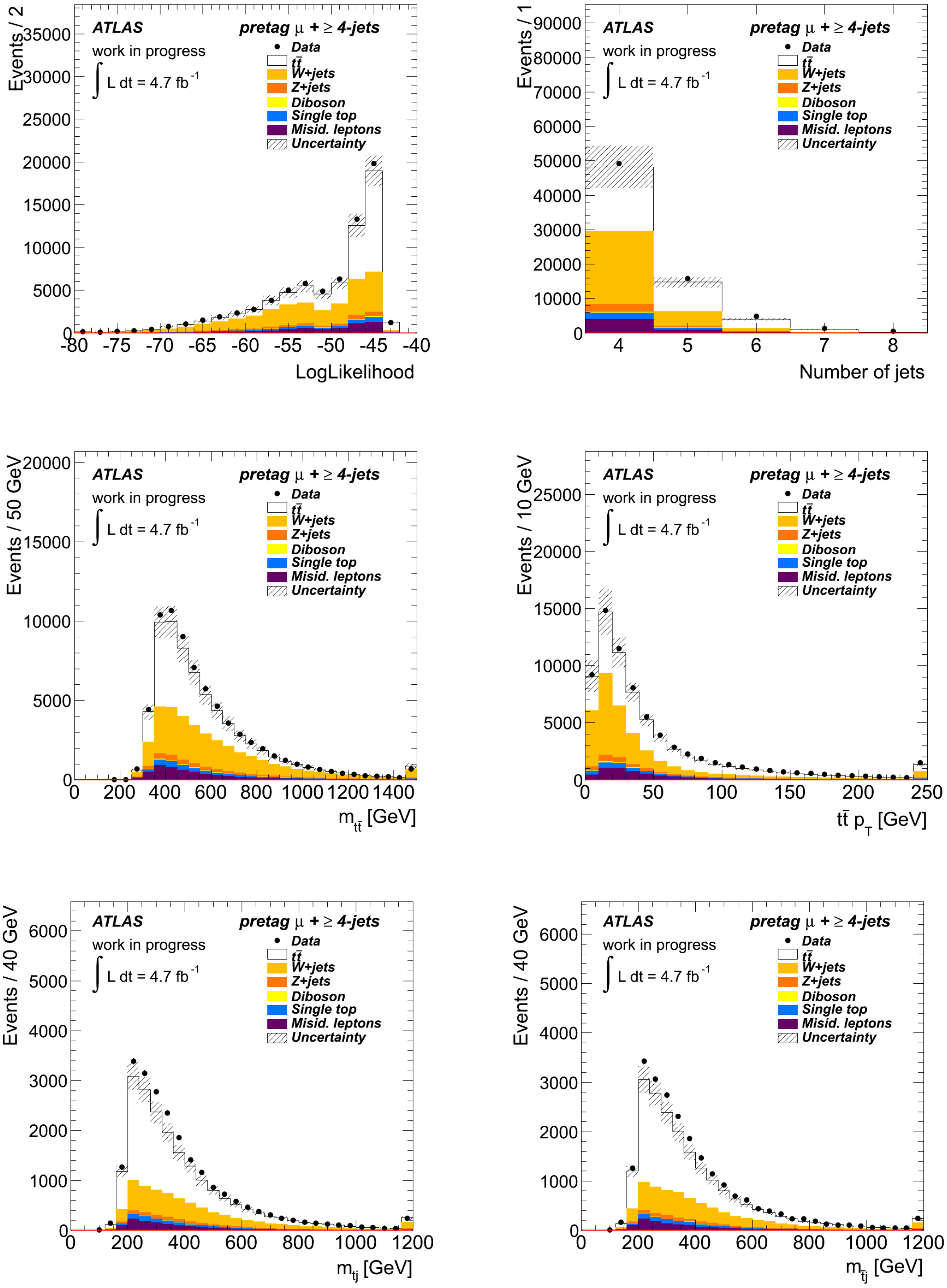

Figure A.2.: Control plots for the μ + jets channel in the pretag region. Shown are the log Likelihood, the jet multiplicity $\mathrm{N_{jets}}$, the invariant mass of the $t\bar{t}$ pair and its transverse momentum as well as the invariant mass of the top-jet and antitop-jet system.

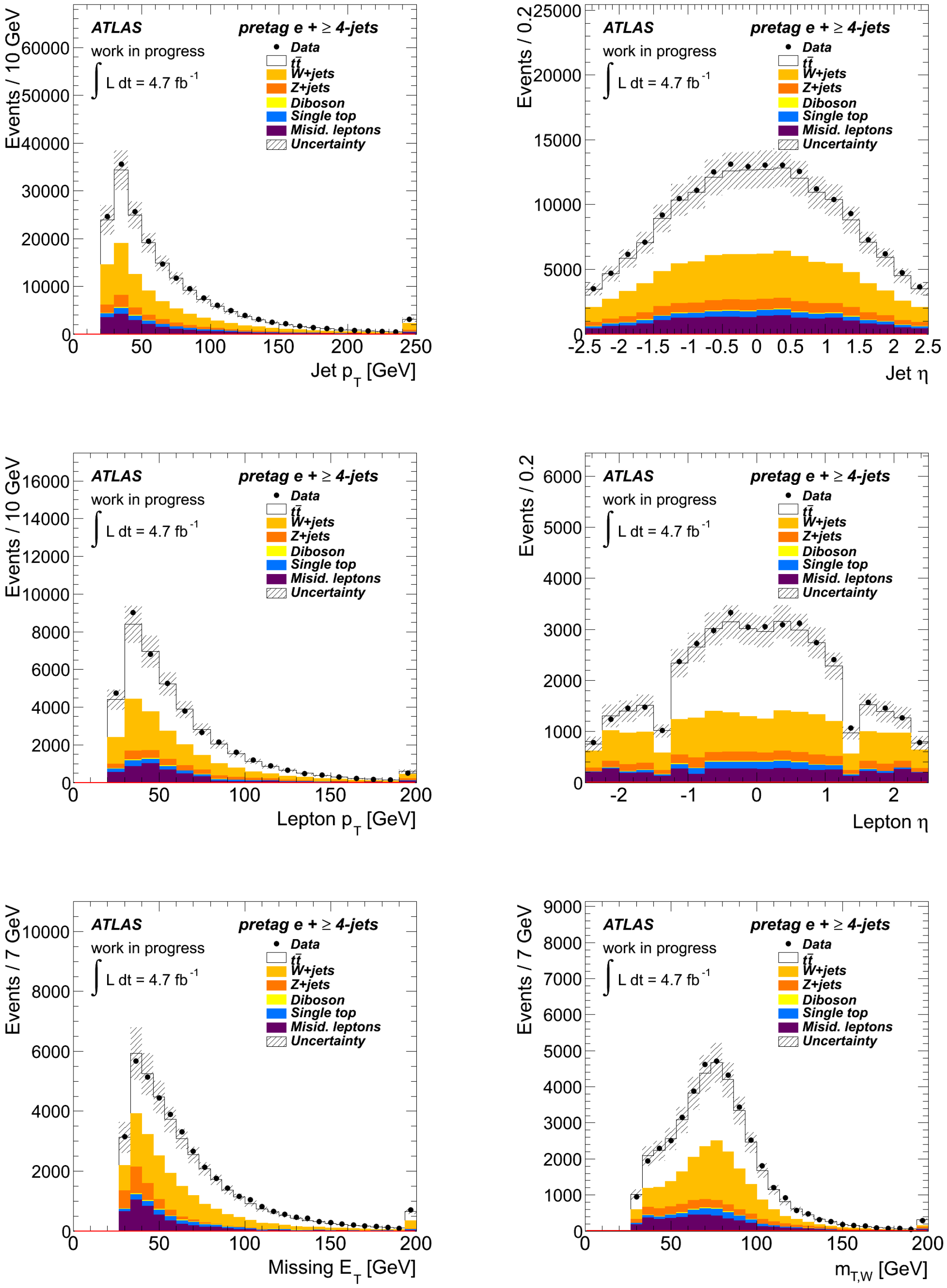

Figure A.3.: Control plots for the e + jets channel in the pretag region with at least four jets and no b-tag requirement. The transverse momentum p_{T} and the pseudorapidity η of the jets and the electron are shown as well as the missing transverse energy distribution $E_{\mathrm{T}}^{\mathrm{miss}}$ and the transverse W-boson mass $m_{\mathrm{T}}(W)$.

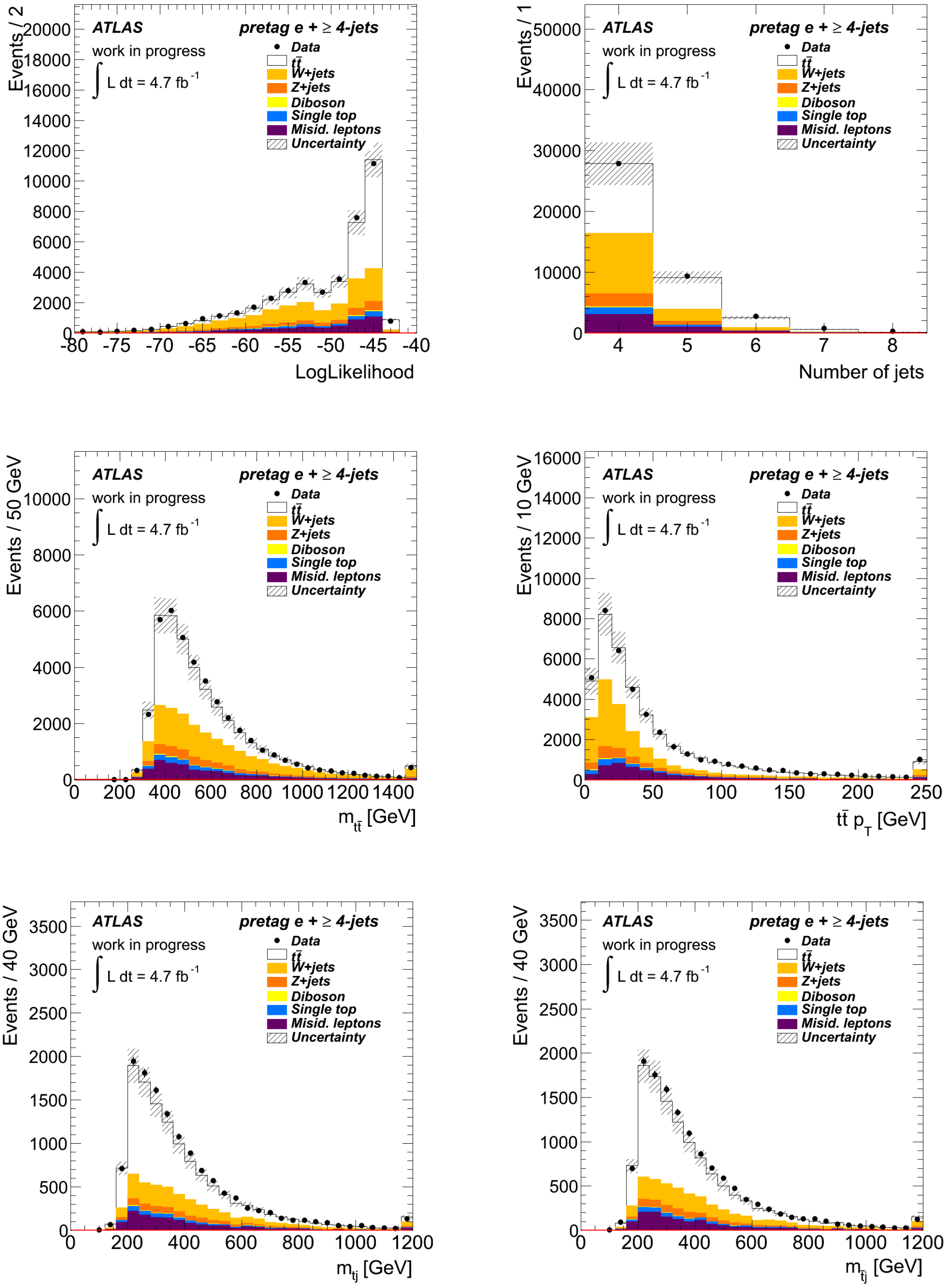

Figure A.4.: Control plots for the e + jets channel in the pretag region. Shown are the log Likelihood, the jet multiplicity $\mathrm{N_{jets}}$, the invariant mass of the $t\bar{t}$ pair and its transverse momentum as well as the invariant mass of the top-jet and antitop-jet system.

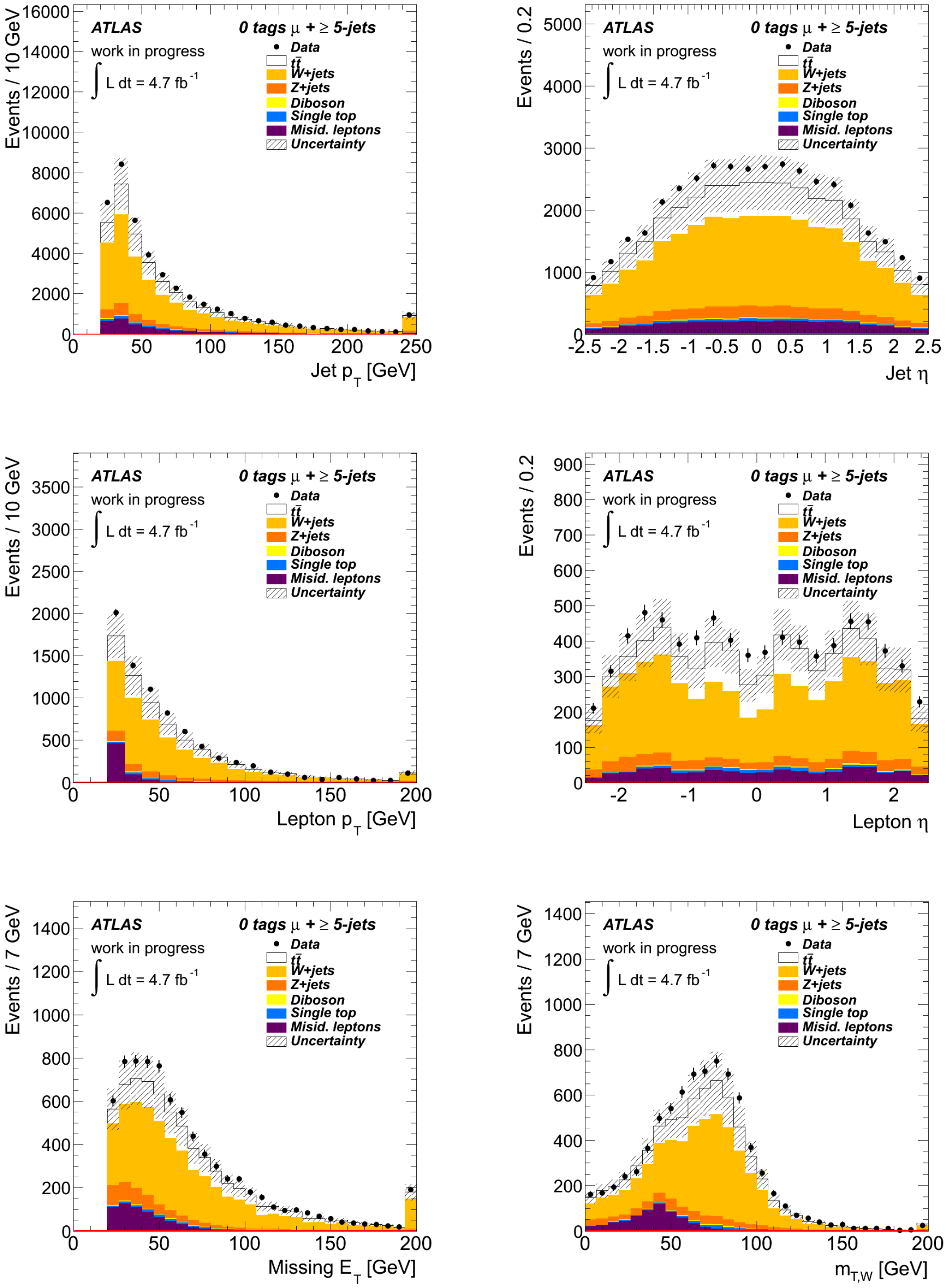

Figure A.5.: Control plots for the μ + jets channel in the enhanced W + jets region with more than four jets and no b-tagged jets. The transverse momentum p_{T} and the pseudorapidity η of the jets and the muon are shown as well as the missing transverse energy distribution $E_{\mathrm{T}}^{\mathrm{miss}}$ and the transverse W-boson mass $m_{\mathrm{T}}(W)$.

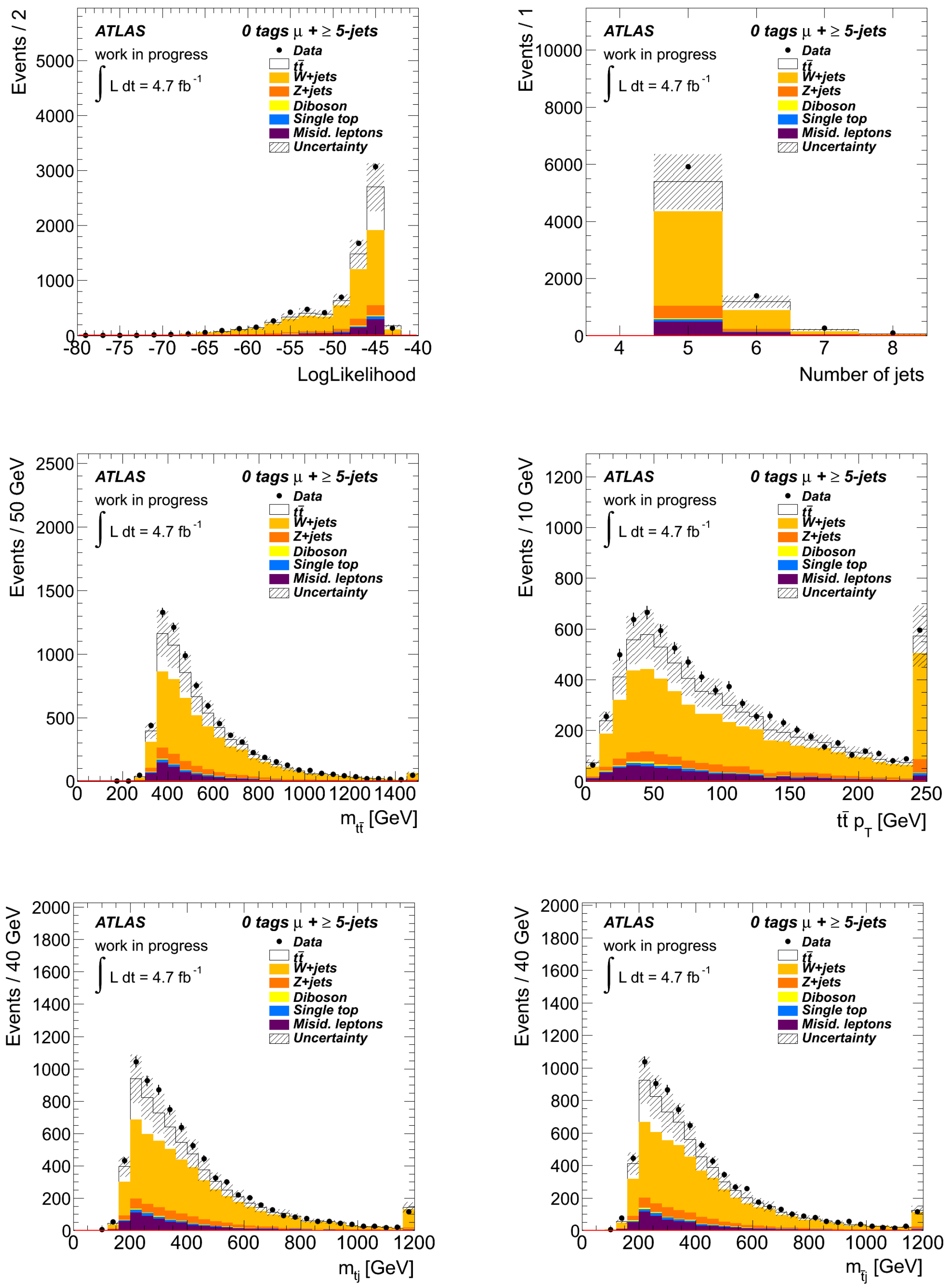

Figure A.6.: Control plots for the μ + jets channel in the enhanced W + jets region. Shown are the log Likelihood, the jet multiplicity, the invariant mass of the $t\bar{t}$ pair and its transverse momentum as well as the invariant mass of the top-jet and antitop-jet system.

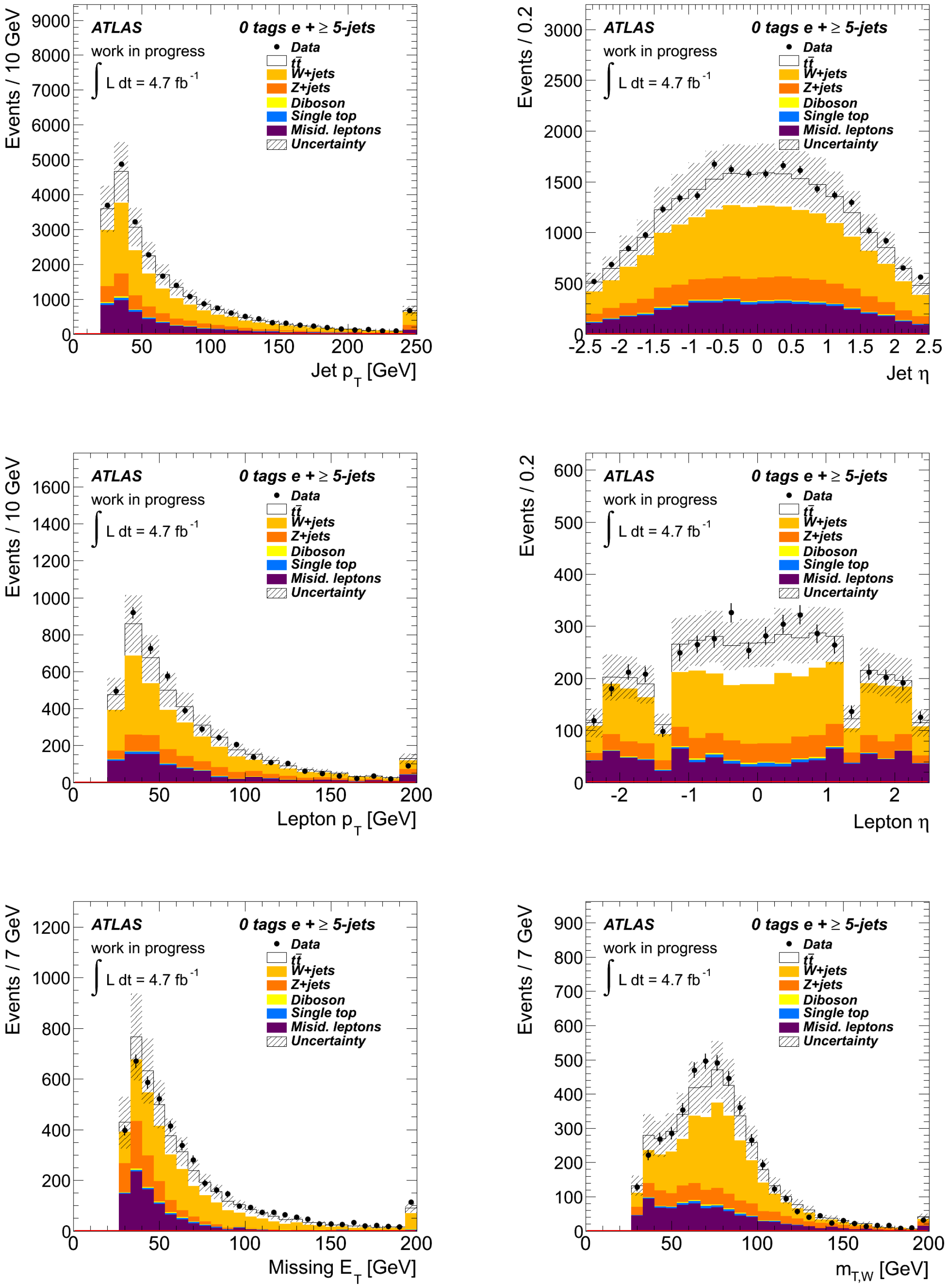

Figure A.7.: Control plots for the e + jets channel in the enhanced W + jets region with more than four jets and no b-tagged jets. The transverse momentum p_{T} and the pseudorapidity η of the jets and the muon are shown as well as the missing transverse energy distribution $E_{\mathrm{T}}^{\mathrm{miss}}$ and the transverse W-boson mass $m_{\mathrm{T}}(W)$.

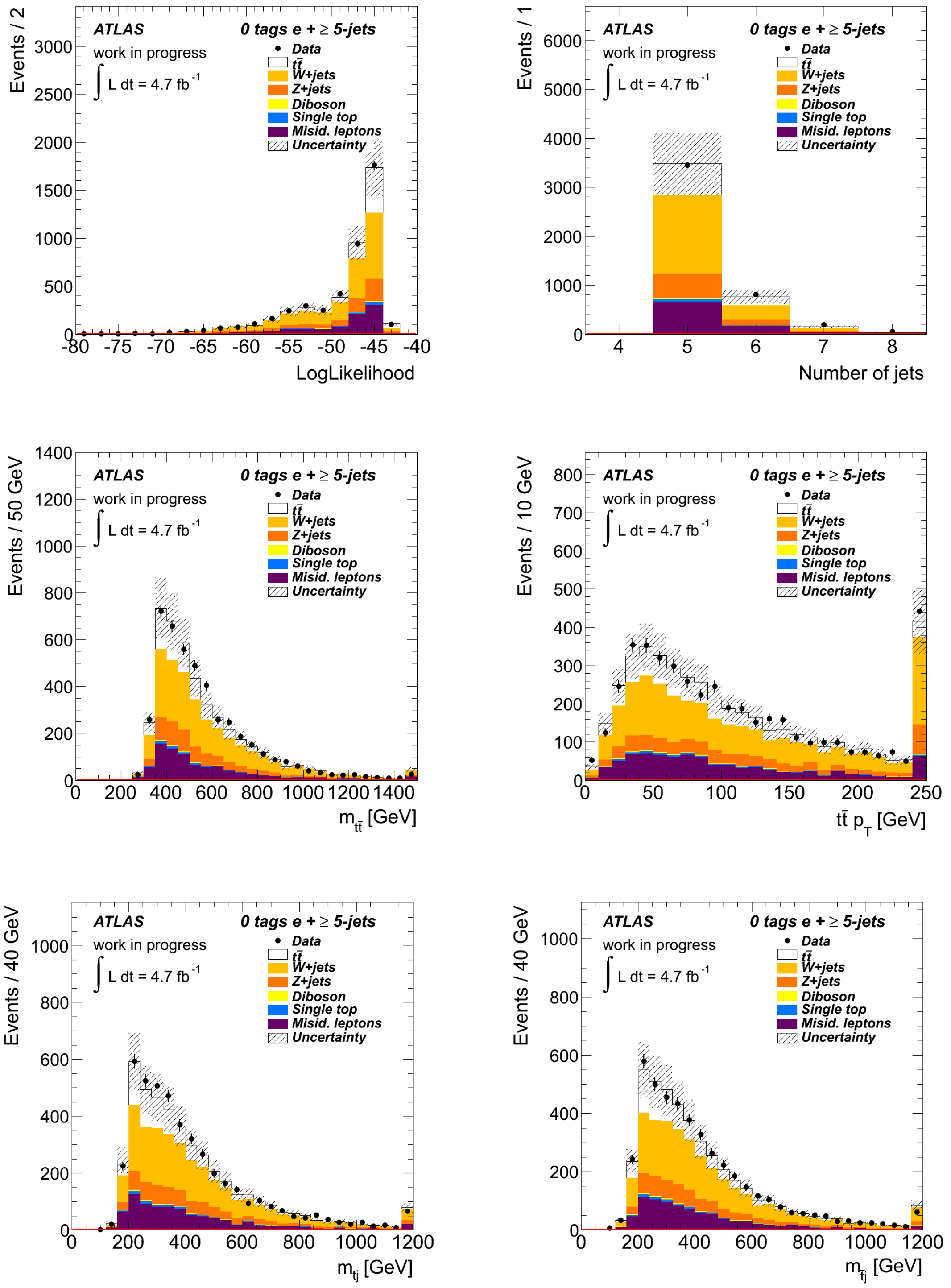

Figure A.8.: Control plots for the e + jets channel in the enhanced W + jets region. Shown are the log Likelihood, the jet multiplicity, the invariant mass of the $t\bar{t}$ pair and its transverse momentum as well as the invariant mass of the top-jet and antitop-jet system.

B. Reconstruction and Total Efficiencies

In this appendix, the reconstruction efficiencies for the singlet and triplet samples with masses of 200 and 1000 GeV are listed in Tab. B.1 and Tab. B.2 for the two different reconstruction techniques. Furthermore, the total efficiencies for the three singlet and triplet samples are given in Tab. B.3 and Tab. B.4 for the $m_{\mathrm{tj}}/m_{\bar{\mathrm{t}}\mathrm{j}}$ mass method.

Number of jets in event	Number of jets considered for fit	Reconstruction Efficiency ϵ_{R} [%]			
		$m_{W'} = 200$ GeV		$m_{\Phi} = 200$ GeV	
		p_{T} method	$m_{\mathrm{tj}}/m_{\bar{\mathrm{t}}\mathrm{j}}$ mass	p_{T} method	$m_{\mathrm{tj}}/m_{\bar{\mathrm{t}}\mathrm{j}}$ mass
≥ 5	5	24.0 ± 2.7	24.0 ± 2.7	22.4 ± 4.5	22.4 ± 4.5
	6	15.6 ± 1.9	14.0 ± 1.8	18.3 ± 3.6	16.5 ± 3.5
	7	14.5 ± 1.7	12.8 ± 1.6	17.1 ± 3.4	15.4 ± 3.3
5	5	23.3 ± 2.9	23.3 ± 2.9	25.3 ± 5.0	25.3 ± 5.0
6	5	27.8 ± 10.6	27.8 ± 10.6	0.0 ± 0.0	0.0 ± 0.0
	6	4.5 ± 1.8	1.5 ± 1.0	6.3 ± 4.3	0.0 ± 0.0
7	5	40.0 ± 21.9	40.0 ± 21.9	–	–
	6	9.1 ± 6.1	0.0 ± 0.0	0.0 ± 0.0	0.0 ± 0.0
	7	5.8 ± 3.2	0.0 ± 0.0	0.0 ± 0.0	0.0 ± 0.0

Table B.1.: Comparison of the reconstruction efficiencies using the two different reconstruction methods for the singlet and triplet samples with $m = 200$ GeV.

Number of jets in event	Number of jets considered for fit	Reconstruction Efficiency ϵ_R [%]			
		$m_{W'} = 1000$ GeV		$m_\Phi = 1000$ GeV	
		p_T method	$m_{tj}/m_{\bar{t}j}$ mass	p_T method	$m_{tj}/m_{\bar{t}j}$ mass
≥ 5	5	40.0 ± 2.2	40.0 ± 2.2	39.0 ± 1.9	39.0 ± 1.9
	6	32.5 ± 1.6	31.1 ± 1.6	31.7 ± 1.4	30.1 ± 1.4
	7	28.1 ± 1.4	26.5 ± 1.4	30.2 ± 1.3	28.0 ± 1.3
5	5	39.1 ± 2.9	39.1 ± 2.9	37.9 ± 2.3	37.9 ± 2.3
6	5	43.6 ± 4.3	43.6 ± 4.3	39.1 ± 3.6	39.1 ± 3.6
	6	29.2 ± 2.4	27.8 ± 2.4	26.5 ± 2.1	24.2 ± 2.1
7	5	37.5 ± 7.0	37.5 ± 7.0	44.4 ± 6.8	44.4 ± 6.8
	6	28.7 ± 4.2	24.3 ± 4.0	29.5 ± 3.7	25.5 ± 3.6
	7	17.8 ± 2.6	13.7 ± 2.3	25.6 ± 2.8	21.6 ± 2.6

Table B.2.: Comparison of the reconstruction efficiencies using the two different reconstruction methods for the singlet and triplet samples with $m = 1000$ GeV.

Number of jets in event	Number of jets considered for fit	Total Efficiency [%]		
		$m_{W'} = 200$ GeV	$m_{W'} = 1000$ GeV	$m_{W'} = 2000$ GeV
≥ 5	5	3.4 ± 0.4	4.6 ± 0.3	1.43± 0.2
	6	3.1 ± 0.4	5.9 ± 0.4	2.6 ± 0.3
	7	3.1 ± 0.4	6.1 ± 0.4	3.0 ± 0.3
5	5	4.6 ± 0.6	6.8 ± 0.6	1.9 ± 0.4
6	5	1.3 ± 0.6	4.5 ± 0.6	1.9 ± 0.4
	6	0.5 ± 0.4	7.5 ± 0.7	4.4 ± 0.7
7	5	1.4 ± 1.0	2.3 ± 0.5	1.5 ± 0.4
	6	0.0 ± 0.0	3.6 ± 0.7	2.5 ± 0.6
	7	0.0 ± 0.0	3.9 ± 0.7	4.0 ± 0.7

Table B.3.: Total efficiencies for different W' samples using the $m_{tj}/m_{\bar{t}j}$ mass method for the reconstruction of the resonance.

Number of jets in event	Number of jets considered for fit	Total Efficiency [%]		
		$m_\Phi = 200$ GeV	$m_\Phi = 1000$ GeV	$m_\Phi = 2000$ GeV
≥ 5	5	3.4 ± 0.8	7.2 ± 0.4	3.5 ± 0.3
	6	3.4 ± 0.8	8.5 ± 0.5	4.7 ± 0.4
	7	3.4 ± 0.8	8.9 ± 0.5	5.4 ± 0.4
5	5	4.9 ± 1.1	9.8 ± 0.7	4.3 ± 0.6
6	5	0.0 ± 0.0	6.0 ± 0.7	3.9 ± 0.7
	6	0.0 ± 0.0	8.9 ± 0.8	7.0 ± 0.9
7	5	0.0 ± 0.0	4.3 ± 0.9	1.5 ± 0.6
	6	0.0 ± 0.0	6.8 ± 1.1	3.7 ± 0.9
	7	0.0 ± 0.0	9.6 ± 1.2	6.5 ± 1.2

Table B.4.: Total efficiencies for different triplet samples using the $m_{\mathrm{tj}}/m_{\bar{\mathrm{t}}\mathrm{j}}$ mass method for the reonstruction of the resonance.

C. Efficiencies for the $t\bar{t}$ Background

The reconstruction of $t\bar{t}$ pairs which is the main background for this analysis with the KLFitter is analysed in this appendix. Therefore, events with at least four jets are selected. If a one-to-one assignment of the four truth partons to the selected jets and the truth lepton to the reconstructed lepton is fulfilled, a $t\bar{t}$ event is labeled matched. The matching efficiencies for the electron and muon channel are listed in C.1 resulting in a overall matching efficiency of 37.9%.

jets in the event	$\epsilon_{\mathrm{M}}[\%]$
≥ 4	37.90 ± 0.04
4	32.52 ± 0.05
5	44.10 ± 0.08
6	49.49 ± 0.10
7	51.80 ± 0.26

Table C.1.: Matching efficiencies for the electron and muon channel in the $t\bar{t}$ sample for different jet multiplicities.

If the event contains a large number of jets, the probability that the KLFitter chooses the correct permutation decreases. Therefore, the number of jets which is considered in the KLFitter for the reconstruction is limited. The reconstruction efficiency can be only evaluated for events which have been selected containing the truth partons. If not all jets in the event are considered for the fit, the matching efficiencies need to be recalculated. Depending on the number of jets in the event and the number of jets considered in the fit, the matching efficiencies for the $t\bar{t}$ sample are given in C.2. As for the singlet and triplet samples, the more jets are taken into account, the larger the matching efficiency.

The reconstruction efficiency for the $t\bar{t}$ sample is defined as the ratio of the number of correclty reconstructed events over the number of matched events. Tab. C.3 contains the reconstruction efficiencies in dependence on the number of jets considered by the KLFitter. If more jets are taken into account, the reconstruction efficiency decreases due to the larger number of permutations.

Number of jets in event	Number of jets considered in fit	Matching Efficiency $\epsilon_{\mathrm{M}}[\%]$ for the $t\bar{t}$ sample
≥ 4	4	23.91 ± 0.04
	5	34.44 ± 0.04
	6	37.24 ± 0.03
	7	37.79 ± 0.04
4	4	32.52 ± 0.05
5	4	13.56 ± 0.06
	5	44.10 ± 0.08
6	4	6.52 ± 0.07
	5	24.97 ± 0.12
	6	49.49 ± 0.10
7	4	3.46 ± 0.10
	5	14.66 ± 0.19
	6	32.82 ± 0.18
	7	51.80 ± 0.26

Table C.2.: Matching efficiencies for the electron and muon channel in the $t\bar{t}$ sample for different jet multiplicities.

Number of jets in event	Number of jets considered in fit	Reconstruction Efficiency $\epsilon_{\mathrm{R}}[\%]$ for the $t\bar{t}$ sample
≥ 4	4	37.96 ± 0.09
	5	33.15 ± 0.07
	6	31.50 ± 0.05
	7	31.07 ± 0.06
4	4	37.86 ± 0.10
5	4	38.28 ± 0.22
	5	26.72 ± 0.10
6	4	39.02 ± 0.55
	5	28.00 ± 0.24
	6	19.11 ± 0.11
7	4	40.47 ± 1.49
	5	30.38 ± 0.63
	6	21.52 ± 0.28
	7	14.77 ± 0.26

Table C.3.: Reconstruction efficiencies for the $t\bar{t}$ sample for different jet multiplicities.

D. Signal Region Plots

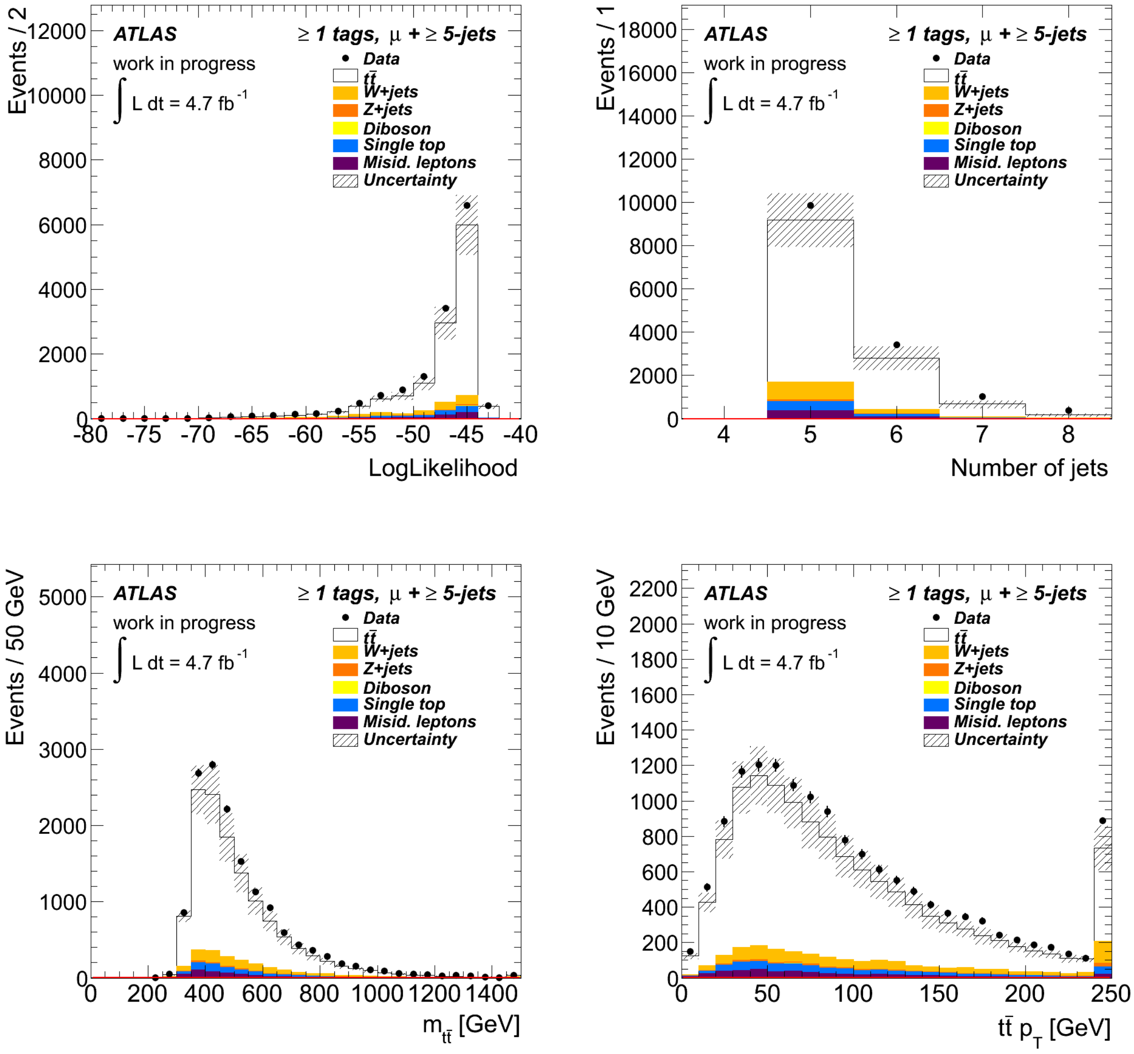

Figure D.1.: Control plots for the μ + jets channel. Shown are the log Likelihood, the jet multiplicity N_{jets}, the invariant mass of the $t\bar{t}$ pair and its transverse momentum.

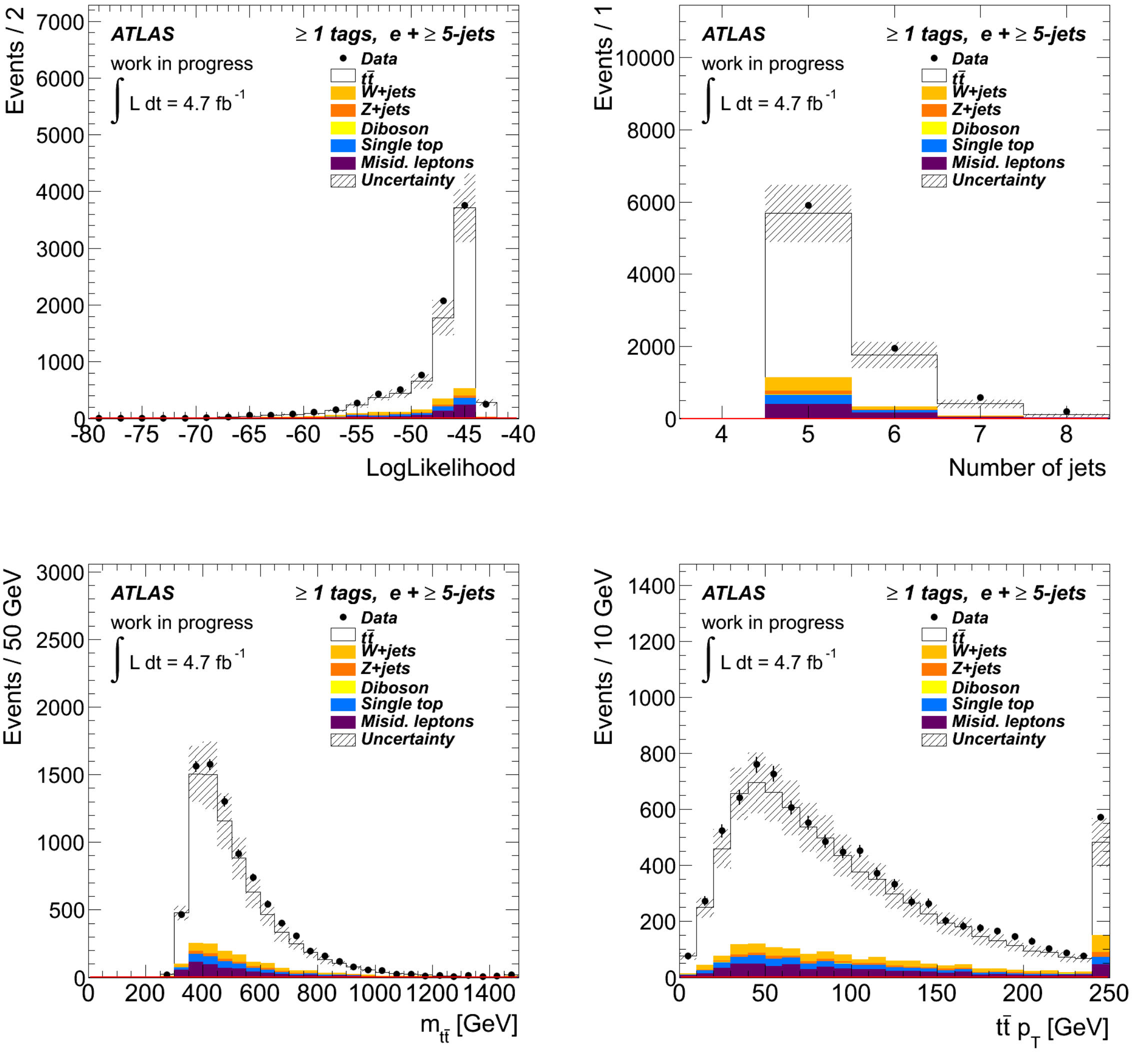

Figure D.2.: Control plots for the e + jets channel. Shown are the log Likelihood, the jet multiplicity $\mathrm{N_{jets}}$, the invariant mass of the $t\bar{t}$ pair and its transverse momentum.

Acknowledgement

Foremost, I would like thank my first referee Prof. Dr. Arnulf Quadt for the opportunity to write my master thesis in the top group. Furthermore, I would like to express my gratitude for his enthusiasm about particle physics and his continuous support during the last years which enabled me to participate in the DESY and CERN summer student programs as well as to work within the Geneva top group. I also want to thank Prof. Dr. Ariane Frey for her willing to be the second referee.

I'm also very thankful to Kevin Kröninger for being my supervisor during the last year and his patience in answering all my questions. Many thanks for all the discussion we had about the analysis, the proof-reading of this thesis and the constructive suggestions.

I'm very grateful to Andrea Knue and Boris Lemmer. This thesis wouldn't have been possible without the two of you. Thanks for answering all my questions about the Grid, the GoeSelection package and all other computing problems. Furthermore, I would like to thank Andrea for always cheering me up when some plots did not look like expected and for providing me with chocolate whenever needed.

Moreover I would like to thank all the members of the II. Physikalisches Institut for the lunch and coffee breaks and the nice atmosphere. Thanks to Julia Rieger, Stefan Guindon and Tamara Vazquez-Schröder for sharing the office with me and especially for the long football discussions. Further thanks to Anna Henrichs for sharing the adventures of the ”Rent a Scientist” program with me. Unfortunately we never went to a concert of the famous Swaggers.

Special thanks go to Emily, Jahred, Kanishka, Daniel and Johnny for giving me opportunity to work on the top plus jet analysis with them and for their patience concerning all my questions.

Many thanks to my friends in Göttingen, who were always there for me when I complained about my analysis, helped me whenever needed and showed me that there is also a world outside the physics department. Thanks for that! Also I want to thank my friends from Buchholz or wherever you might be at the moment for your interest in my work although I'm not searching for the Higgs boson :) and for being so understanding if I don't have the time to contact you for a long time.

Last but not least I would like to thank the most important people: Vielen Dank an meine Eltern Renate und Günter Delitzsch für die finanzielle Unterstützung ohne die so ein ”entspanntes” Studium sicherlich nicht möglich gewesen wäre. Vor allem möchte ich euch aber und natürlich auch meiner Schwester Kim für die jahrelange mentale Unterstützung danken und besonders für die Aufmunterungen während der letzten Wochen.

Erklärung nach §18(8) der Prüfungsordnung für den Bachelor-Studiengang Physik und den Master-Studiengang Physik an der Universität Göttingen:

Hiermit erkläre ich, dass ich diese Abschlussarbeit selbständig verfasst habe, keine anderen als die angegebenen Quellen und Hilfsmittel benutzt habe und alle Stellen, die wörtlich oder sinngemäß aus veröffentlichten Schriften entnommen wurden, als solche kenntlich gemacht habe.

Darüberhinaus erkläre ich, dass diese Abschlussarbeit nicht, auch nicht auszugsweise, im Rahmen einer nichtbestandenen Prüfung an dieser oder einer anderen Hochschule eingereicht wurde.

Göttingen, den 20. November 2012

(Chris Malena Delitzsch)